Human Activity Recognition and Control of Wearable Robots

by

Prudhvi Tej Chinimilli

A Dissertation Presented in Partial Fulfillment
of the Requirements for the Degree
Doctor of Philosophy

Approved October 2018 by the
Graduate Supervisory Committee:

Sangram Redkar, Co-Chair
Wenlong Zhang, Co-Chair
Thomas G. Sugar
Hyunglae Lee
Hamidreza Marvi

ARIZONA STATE UNIVERSITY

December 2018

ABSTRACT

Wearable robotics has gained huge popularity in recent years due to its wide applications in rehabilitation, military, and industrial fields. The weakness of the skeletal muscles in the aging population and neurological injuries such as stroke and spinal cord injuries seriously limit the abilities of these individuals to perform daily activities. Therefore, there is an increasing attention in the development of wearable robots to assist the elderly and patients with disabilities for motion assistance and rehabilitation. In military and industrial sectors, wearable robots can increase the productivity of workers and soldiers. It is important for the wearable robots to maintain smooth interaction with the user while evolving in complex environments with minimum effort from the user. Therefore, the recognition of the user's activities such as walking or jogging in real time becomes essential to provide appropriate assistance based on the activity.

This dissertation proposes two real-time human activity recognition algorithms intelligent fuzzy inference (IFI) algorithm and Amplitude omega ($A\omega$) algorithm to identify the human activities, i.e., stationary and locomotion activities. The IFI algorithm uses knee angle and ground contact forces (GCFs) measurements from four inertial measurement units (IMUs) and a pair of smart shoes. Whereas, the $A\omega$ algorithm is based on thigh angle measurements from a single IMU.

This dissertation also attempts to address the problem of online tuning of virtual impedance for an assistive robot based on real-time gait and activity measurement data to personalize the assistance for different users. An automatic impedance tuning (AIT) approach is presented for a knee assistive device (KAD) in which the IFI algorithm is used for real-time activity measurements. This dissertation also proposes an adaptive oscillator method known as amplitude omega adaptive oscillator ($A\omega AO$) method for HeSA (hip exoskeleton for superior augmentation) to provide bilateral hip

assistance during human locomotion activities. The $A\omega$ algorithm is integrated into the adaptive oscillator method to make the approach robust for different locomotion activities. Experiments are performed on healthy subjects to validate the efficacy of the human activities recognition algorithms and control strategies proposed in this dissertation. Both the activity recognition algorithms exhibited higher classification accuracy with less update time. The results of AIT demonstrated that the KAD assistive torque was smoother and EMG signal of Vastus Medialis is reduced, compared to constant impedance and finite state machine approaches. The $A\omega AO$ method showed real-time learning of the locomotion activities signals for three healthy subjects while wearing HeSA. To understand the influence of the assistive devices on the inherent dynamic gait stability of the human, stability analysis is performed. For this, the stability metrics derived from dynamical systems theory are used to evaluate unilateral knee assistance applied to the healthy participants.

To my family, without whom this would not have been possible.

ACKNOWLEDGMENTS

I would like to thank my co-advisors, Dr. Sangram Redkar and Dr. Wenlong Zhang, for their constant support and guidance throughout my PhD. Also, I would like to thank the other members of my committee: Dr. Thomas Sugar, Dr. Hyunglae Lee, and Dr. Hamid Marvi for their constructive feedback and helpful comments to improve my dissertation work.

I would like to thank both Robotics and Intelligent Systems laboratory and Human Machine Integration Laboratory members Zhi Qiao, Seyed Mostafa Rezayat Sorkhabadi, Vaibhav Jawar, Iat Hou Fong, Sean Wolfgang Wachtel, Shatadal Mishra, Susheelkumar C. Subramanian and Sandesh Bhatt for their help to add material to this dissertation. I would like to thank my parents and brother for their moral support through this process. I would especially like to thank my girlfriend Vijetha Gattupalli, for her love and support.

TABLE OF CONTENTS

v

LIST OF TABLES

LIST OF FIGURES

xii

Figure   Page

xviii

Chapter 1

INTRODUCTION

In 2050, the population aged 65 and over in United States is projected to be 83.7 million, almost double to its estimated population of 43.1 million in 2012 [1]. The aging poses several challenges related to nervous system (such as Alzheimers disease, stroke, and Parkinsons disease) and musculoskeletal system (such as arthritis and osteoporosis). As a result, a significant number of people have suffered difficulties to perform daily activities such as walking and climbing stairs. Therefore, the demand for rehabilitation training increased over the years. The research challenges for the rehabilitation involve the development of therapeutic methods and assistance modes that help the patients to improve their daily activity performance and to restore lost or impaired motion control.

The manual rehabilitation or supervised therapy is expensive, time consuming, and involves intensive labor of both physical therapists and patients [2]. Also, the therapists need patients to visit the rehabilitation facility regularly to check on the recovery progress that may cause inconvenience to patients. The aforementioned drawbacks motivate researches to develop an alternate solution based on wearable sensors and assistive devices. The wearable sensors and assistive devices help the patients to live independently at their homes while being remotely monitored by the therapists and provide feedback to the patients [3].

The wearable sensors along with assistive device form a personalized system for the patients which helps them to perform rehabilitation training remotely. The assistive robots need wearable sensors to record the kinematics and kinetics data such as position, velocity, and torque of the joints. They are equipped by actuations to move

the users limb, and they are designed to make the compensations of physical capabilities of patients [4]. Assistive robots can provide both the movement controllability and the measurement reliability, which makes them ideal instruments to help neurologists and therapists address the challenges facing neurorehabilitation [5]. Studies have shown that therapy should be intense and repetitive to achieve the maximum benefit [2]. To provide such training, rehabilitation equipment must be activated. Assistive robots are tireless in contrast to human-being trainers. Besides, because of their sensors, robots can monitor movement quality as well as progress constantly, providing highly specific feedback to patients to aid learning. The benefits of robots for rehabilitation are therefore multifold: they can produce repetitive high-quality movements, allowing increased intensity of rehabilitation [6]; they can provide a large variety of exercises for the therapist to choose from; they provide a smooth man-machine interaction which allows an objective measure of progress, which itself can allow changes in the interaction by altering control parameters [7].

The other major application of the wearable sensors and assistive robots is in the area of military [8]. Soldiers required to perform combat missions when they reach their destination. To assist in such cases, military exoskeletons have been developed to amplify the capabilities of the soldier and help them to travel long distances with reduced metabolic costs [9]. The wearable sensors provide kinematics and kinetics data for the exoskeleton to assist the soldiers [10].

1.1 Wearable Sensors

The advances in microelectronics and sensor technology have enabled the development of wearable sensors. A survey reported that the number of wearable sensors will increase from 22 million in 2013 to 177 million in 2018 [11]. Assisted living applications leveraging wearable sensors enable a healthier life style and independence

in the people. The monitoring of daily activities is crucial to assess the quality of life of various target population. The possibility of life-logging is enabled with the aid of developing technology and the reduced cost of wearable sensors. People are logging everything from the number of steps taken in a day to the range of activities performed.

Wearable sensors have diagnostic, as well as monitoring applications. The current capabilities of the wearable sensors include physiological, bio-mechanical sensing, and motion sensing. Wearable sensors are used to gather physiological and movement data thus enabling patient's status monitoring. Sensors are deployed according to the clinical applications of interest. Wearable sensors for movement data are used in applications such as monitoring effectiveness of home-based rehabilitation interventions in stroke survivors or the use of mobility assistive devices in older adults.

The wearable motion sensors such as accelerometers, gyroscopes, and magnetometers significantly impact the management of Parkinsons disease and post-stroke rehabilitation [12, 13, 14, 15]. Cancela, et al. have evaluated the feasibility of wearable system to assess the gait in PD patients [16]. The body-fixed accelerometers are used to enhance the utility of Timed Up and Go (TUG) test when evaluating PD patients [17]. The TUG test is a popular clinical test of mobility and fall risk. Uswatte, et al, have shown the data from body-worn accelerometers can provide objective information about real-world arm activity in stroke survivors [15]. Prajapati et al. have placed two accelerometers on each leg to monitor walking in stroke survivors [18]. Results showed that the system could monitor the symmetry and bio-mechanical characteristics of walking. Huang et al. have developed a micro-sensor based extremity rehabilitation system to evaluate motor impairment [19]. The system embedded in fabric of the garments include inertial sensors to capture motion, and enable the reconstruction of 3-D movement by the stroke patients. Philips Research have devel-

oped home-based rehabilitation technology known as Stroke Rehabilitation Exerciser [20]. This device coaches the patients through series of exercises for motor training.

In addition to kinematics, it is important to measure the kinetics. For kinetics, the force exerted on the ground i.e., ground reaction forces (GRFs) are essential for inferring the torque generated at each joint. The force plates are used in laboratory to measure these forces. The force plate have the limitations that they are restricted to the laboratory environment and entail high equipment costs. As an alternative, wearable pressure sensing insoles and inertial sensors have been developed. Morris Bamberg et al. [21] present an insole which incorporates two dual-axis accelerometers, three gyroscopes, four force sensitive resistors, two polyvinylidene fluoride strips, two bend sensors, and an electric field sensor for the analysis of Parkinson's gait. Pressure sensing shoes and insoles are also presented by Howell et al. [22] and Strohrmann et al. [23] to study the motion of stroke and Cerebral Palsy patients, respectively. Both Lo et al. [24] and Neugebauer et al. [25] propose to further simplify kinetic analysis using micro-inertial sensors for GRF measurement. Although GRF is critically important for kinetics analysis, it can only be used to infer virtual force generated at each joint by inverse dynamics, which may not be enough in practice.

In addition to GRF, surface EMG (sEMG) systems can be used to measure muscle activity for better understanding of muscle characteristics, muscle force estimation, and movement identification. Previous studies capture myoelectric signals through high density arrays of surface electrodes as they are less invasive than intramuscular electrodes and provide high resolution measurements. To estimate muscle forces using sEMG, musculoskeletal models and learning methods are typically used. For example, Staudenmann et al. [26] used a high density electrode array and principal component analysis (PCA) to estimate muscle force. PCA was used transform the spatial distribution of muscle activations into linearly independent ranked modes,

split into a sum of higher modes and lower modes, for muscle force estimation. Shao et al. [27] used a modified Hill-type muscle model [28] for describing lower limb anatomy. High-pass filtering, full wave rectification, normalisation using peak rectified EMG measurements, and low-pass filtering are used to process the measurements. A calibration process which incorporates EMG and kinematics was used to determine parameters between EMG and muscle activation of the muscle model to achieve RMS errors between 9.7% and 14.7%. Similarly, Naeem et al. [29] also rectified smooth EMG measurements, which are combined with a back-propagation neural network.

1.2 Wearable Robots for Assistance

The term wearable robotics came into existence in the 1960s when research efforts started to focus on developing load augmentation and rehabilitation systems. Essentially, wearable robots help users perform a variety of tasks such as carry heavy loads, reduce the burden in physically demanding tasks, and apply rehabilitation treatment to patients. Also, the wearable robots assist the users in performing daily activities such as walking, ascending/descending stairs, and sit-to-stand transfer.

The wearable robots can be classified in to two major classes: medical and non-medical robots. The medical robots are used to provide mobility to physically disabled, injured or weak persons who have walking difficulties due to a variety of medical reasons such as SCI, stroke, and PD. Primarily, these robots are used in controlled environment such as hospitals and rehabilitation centers. On the other hand, non-medical robots assist healthy persons like soldiers to perform physically demanding tasks such as carrying heavy loads and marching on rough terrain. In this section, review on wearable robots for rehabilitation and military applications are discussed.

1.2.1 Rehabilitation applications

Rehabilitation is needed for the patients with gait disorders due to medical conditions such as lesions in the central nervous system, cerebrovascular accidents, cerebral palsy and so on. Over the last decade, several lower-limb rehabilitation robots have been developed as a possible solution to provide therapy and retrain the patients to walk again [6]. An exoskeleton named Lokomat developed by Hocoma (Switzerland) is a treadmill-based body weight support device which includes audio-visual biofeedback, using a screen in front of the user; it is powered at the hip and knees [30]. The MIT-Skywalker robot is used for rehabilitation treatment of patients with stroke and nerve injury was developed by Massachusetts Institute of technology in the United States [31]. The robot is composed of a mechanism of sitting weight loss and a mechanism of foot movement.

The Active Leg Exoskeleton (ALEX) is a powered leg orthosis with linear actuators at the hip and knee joints, and with a force-field controller developed to provide assistance to the patient by using the assist-as-needed approach [32]. It has been tested with two chronic stroke survivors, whose gait patterns were substantially improved after the training [33].

The gait rehabilitation robot LOPES (LOwer-extremity Powered ExoSkeleton) can move in parallel with the legs of a person walking on a treadmill, at pelvis height flexibly connected to the fixed world [34]. The Ekso GT exoskeleton developed by Ekso Bionics is a wearable exoskeleton suit designed for the assistance and rehabilitation of patients with various levels of lower extremity weakness [35]. It is suitable for a wide range of patients such as paralyzed patients and other patients with lower level of mobility disorder such as stroke survivors. Clinical studies have verified that gait training with the Ekso GT exoskeleton supports patients in relearning a correct

step pattern and allows them to take a greater number of steps at a faster speed, compared to traditional rehabilitation.

1.2.2 Military applications

Lower extremity exoskeletons developed for human strength augmentation can enhance human strength and endurance during locomotion, and enable individuals to perform tasks that they cannot easily perform by themselves. The Berkeley Lower Extremity Exoskeleton (BLEEX) was developed to help soldiers to carry heavy loads [36, 37]. It has seven DOFs per leg: three DOFs at the hip joint, one DOF at the knee joint, and three DOFs at the ankle joint. Among these DOFs, hip flexion/extension, hip abduction/ adduction, knee flexion/extension, and ankle dorsiflexion/ plantarflexion are actuated by linear hydraulic actuators. The remaining DOFs are passively actuated by steel springs and elastomers. It has been reported that BLEEX wearers can walk at an average speed of 1.3 m/s while carrying a 34 kg payload.

Other similar military exoskeletons include Sarcos XOS2 (Raytheon, USA) [38], HULC (Berkeley Robotics and Human Engineering Laboratory, CA, USA) [39], Exo-climber (Berkeley Robotics and Human Engineering Laboratory [40], CA, USA and so on which have been designed to augment capabilities of soldiers in wartime and in emergency operations. The main challenge in developing load augmentation exoskeletons for soldiers is how to reduce the overall weight yet maintain high levels of augmentation for long durations so that soldiers will stay fresh for combat. These devices are likely to be practically useful only if they reduce the metabolic cost significantly while augmenting the load carrying capacity of soldiers. However, the high torque actuators require more power and bigger batteries for the long operational times; it is clear longer-lasting lightweight batteries are needed to realize solutions able to contribute in this sector. Preventing misalignment of the human joints during

actuation over the long wear times is another open research challenge for the future.

1.3   Human Activity Recognition

The major contribution of the wearable sensors is in the field of human activity recognition (HAR). HAR is important for a wide range of applications including assisted living, medical, health-care, fitness, and military. The recognition of the human activities is important for the treatment of patients which provide useful feedback to the therapists. In military, it is important to identify the locomotion activities of the soldiers such as level walking, uphill, and running to provide feedback to the wearable robot that assists the soldiers in real-time.

The recognition of the human activities is achievable with two methods: external and internal sensing. In external sensing, sensors such as cameras are employed to recognize activities and gestures from video sequences. The major drawbacks of external sensing are that they entail high equipment and maintenance cost and users must restrict to the laboratory environment. On the other hand, internal sensing allows users to move outdoors and are of less size, low cost and easily portable. Therefore, wearable sensors provide an alternative method to perform human activity classification considering the aforementioned advantages. Researchers have been developing activity monitoring algorithms given the emergence of wearable sensors. Typically, these methods employ a series of steps that includes time window selection, feature extraction, dimension reduction and applying classification algorithm. A fixed time window is used to extract the features [41]. Some used sliding window which slides between the two adjacent windows [42]. Others developed adaptive time window to account for the periodicity in the activities such as walking and running [43]. The common features that are used in feature extraction module are time-based, frequency-based and wavelet-based features. The dimension reduction techniques such as principal

component analysis (PCA) and linear discriminant analysis (LDA) are used to reduce the number of features. A large number of classification algorithms are explored on the set of features. The algorithms used for gait activity classification include support vector machines (SVM) [44], hidden Markov models (HMM) [45], Gaussian mixture models (GMM) [46], neural networks [47] and logistic regression [48].

An adaptive algorithm based on decision trees with four sensors attached to the body is implemented for recognition of activities such as walking and running [49]. Identification of locomotion modes is achieved with 12 EMG sensors by fusing LDA with artificial neural network (ANN) [50]. LDA and ANN methods are also used with time-domain and frequency-domain from nine EMG signals to perform intent recognition [51]. Also, multiple accelerometers and foot sensors are used to classify walking, running, stair ascent and stair descent [52, 53]. The multiple sensors on the body may cause discomfort to the users and restrict them from performing normal movements. Therefore, there is a need to reduce the number of sensors that are being used for activity recognition without compromising the accuracy of the recognition. A phase variable approach based on a single IMU sensor data is used for detecting locomotion activities such as walking, stair ascent, and stair descent [54]. Others used single IMU for real-time continuous gait phase and gait speed estimation [55].

1.4   Dissertation Organization

The goals of this dissertation are to develop novel human activity recognition algorithms using wearable sensors that can detect activities, especially periodic activities in real-time. Then, the next step is to integrate these algorithms in the high-level control of wearable robots to aid modulating the impedance as well as the parameters for the adaptive oscillator of the wearable robot based on the activity detection. This document is organized as follows:

Chapter 2: Related work. This chapter covers the background research in the area of human activity recognition and control of wearable robots. The types of sensors used and algorithms implemented for detecting the activities are discussed. The integration of wearable sensors to wearable robots and their control strategies are reviewed.

Chapter 3: Human activity recognition using smart shoes and inertial measurement units. This chapter presents the novel algorithm developed using smart shoes and four inertial measurements units (IMUs) mounted on bilateral thighs and shanks to detect six activities standing, sitting, walking, going upstairs, going downstairs, and jogging. Also, the algorithm developed for compensation of the hysteresis effect in pressure sensors that are embedded in smart shoes is discussed in detail. The experimental results to test the efficacy of the algorithms are presented.

Chapter 4: A Two-dimensional feature space based approach for human locomotion recognition. This chapter details the algorithm developed for human locomotion recognition using a single inertial measurement unit. The method to extract novel features amplitude A and omega ω are discussed. Also, the method to detect the transitions among the activities is explained. The experimental results in indoors and outdoors are presented to verify the robustness of the proposed algorithm.

Chapter 5: Automatic virtual impedance adaptation of a knee exoskeleton for personalized walking assistance. This chapter presents an approach to address the problem of online modulation of virtual impedance for a wearable assistive robot based on real-time gait and activity detection. The integration of activity recognition algorithm proposed in chapter 3 to the wearable knee exoskeleton is detailed. The details of the training of the Gaussian mixture model with fuzzy likelihood values of activities and gait phases is discussed. Finally, the experimental results related to muscle activity and kinematics are presented.

Chapter 6: The assessment of the dynamic gait stability of human-lead (lower extremity assistive device) system using metrics derived from dynamical systems theory. The objective of this chapter is to understand the walking from dynamical systems theory and chaotic dynamics perspective. The stability metrics derived from dynamical systems theory are used to evaluate the influence of the assistive device on the inherent stability of the human The methods to compute stability metrics is detailed. Additionally, biped simulations results are presented to understand the chaotic behavior of walking. The experimental results for eight healthy participants for five conditions: normal walking, passive, zero impedance, the finite state machine (FSM), and automatic impedance tuning (AIT) are presented.

Chapter 7: Human locomotion assistance using $A - \omega$ features based adaptive oscillator. This chapter presents an approach to implement a prediction module based on A-ω features. Also, it presents an adaptive oscillator method known as $A-$ which provides bilateral hip assistance during locomotion activities such as walking and running. The details of the low-level classifier, support vector machine (SVM) and high-level classifier, discrete hidden Markov model (DHMM) are given. Finally, experimental results are presented with participants wearing HeSA (hip exoskeleton for superior augmentation).

Chapter 8: Conclusion and Future work.

1.5 Contributions of this Dissertation

- An approach to achieve reliable ground contact force (GCF) measurements from smart shoes by compensating hysteresis in pressure sensors embedded in smart shoes.

- An activity recognition algorithm using smart shoes and inertial measurement

units that achieves significant classification accuracy in subject dependent and independent tests.

- An activity recognition algorithm using a single inertial measurement that achieves considerable accuracy with less training of the algorithm.

- An approach to address the problem of online modulation of virtual impedance for an wearable assistive robot based on activity and gait phase detection.

- An approach to modulate the parameters of the adaptive oscillator for an hip exoskeleton based on the prediction of transitions between the activities.

- Assessment of the overall stability of the human-LEAD system using metrics derived from dynamical systems theory. This assessment provide useful insights to understand the robotic device assistance from stability perspective.

Chapter 2

RELATED WORK

The wearable robot should possess cognitive skills in its control framework given it forms closer cooperation with the human user [10, 56]. To be effective in daily life activities, the controller need to be skilled enough to be able to estimate the intended movement of the user (e.g., walking, standing, sitting, or climbing stairs) and estimate the gait phases of the periodic locomotion related tasks. Also, the controller should account for the minor changes caused by intracycle variability [57]. This chapter reviews: a) Human activity recognition algorithms using wearable sensors, and b) the control strategies of the wearable robots that include activity recognition module in their high level control.

2.1   Human Activity Recognition using Wearable Sensors

Finite state machine (FSM) structure with pre-defined trajectories are generally employed in lower-limb exoskeletons. Pilots with these exoskeletons give commands manually by the machine user interface for different tasks such as walking, sitting, or standing. There are two main issues for this exoskeletons, when and how to provide assistance. As these exoskeletons receive order from pilots, there is a high possibility that pilot can give wrong command which may lead to accidents. Ideal exoskeleton walks as intention of human and becomes a part of human which will let the pilot sense no existence of exoskeleton. Therefore, there is a need for human intention or activity recognition which provides safety as well as better experience to the user.

Several studies proposed different approaches for the online recognition of human activities. Recent reviews [57, 58] presented a detailed overview of the sensory net-

works constituting a humanrobot interface and of the methods of activity recognition. The electromyography (EMG) signals from six muscles were used to recognize activities level walking, ramp ascent, and ramp descent modes [59]. In active prostheses, the intention recognition based on surface electromyography (sEMG) were the most common [50, 60]. Sensing based on sEMG was then coupled with the measurements acquired from mechanical sensors such as angular sensors, inertial measurement units (IMUs), or load cells, to embed sensory systems devoted to intention recognition in the prosthetic segments of the mechatronic device itself [61, 62]. Nevertheless, the robustness of EMG sensing is prone to fade in prolonged use because of skin temperature variations, sweating, and relative movements between the skin and electrodes. Therefore, alternative approaches have more recently abandoned sEMG electrodes preferring networks of mechanical sensors to minimize the invasiveness of the interface and increase its dependability [63, 64, 65].

Along with the sensory system, the techniques used for classification plays a key role in the activity classification. For mechanical sensors measurements, simple threshold-based finite state machine controllers are used [63, 64]. The success rate improved when fuzzy-logic-based classifiers [65] or linear discriminant analysis [66] techniques are applied. Other works have implemented ANN combined with heuristic methods for identification of locomotion mode and detection of gait cycle. These works used multiple accelerometer sensors and foot ground contact data from walking, running, stair ascent and descent [52, 67, 53]. Even though all these works achieved a recognition accuracy between 90% and 95%, they required a large number of sensors attached to the human body, which makes the calibration, synchronization and data collection complicated processes that impact on the computational cost and complexity of implementation. Fuzzy logic and combination of ANN and EMG signals, were employed for human intent recognition and prosthesis control achieving

an accuracy of 95% [68]. Multiple human activities were recognized using EMG and vision sensors with support vector machines (SVMs). These methods achieved accuracies between 77.3% and 99%, however, they need a large number of sensors that also limits these works to indoor applications [69, 70]. SVM and k-nearest neighbour algorithms, together with 9 accelerometers distributed from the torso to the ankle, achieved an accuracy of 97.6% for recognition of activities [70]. The combination of plantar pressure sensors with multi-class SVMs allowed the recognition of normal walking, stair ascent and stair descent activities with accuracies between 91.9% and 95.2% [71]. The listed algorithms here achieves significant accuracy with subject dependent training and exhibits less accuracy with subject independent training.

Therefore, two possible solutions are proposed in this dissertation: 1) Human activity recognition system with more sensors which can achieve significant accuracy in both subject dependent and independent tests, and 2) human activity recognition system with one sensor that can achieve considerable accuracy in subject dependent tests with less training data.

2.2 Control Strategies for Wearable Robots

Human motion intention estimation requires an understanding of how locomotion is nominally controlled in humans and how the users state and intent can be sensed. The terrain features and surface conditions of the environment (i.e. the environmental state) constrain the type of movements that can be carried out, and if perceived by the controller can be taken into account. Interaction forces exist between the device, the user, and the environment, which can also be sensed as an input to the controller.

Several algorithms for the human activity recognition were developed for powered lower limb exoskeletons [72]. To assist ground-level walking, variable stiffness actuation is a common adopted strategy for adapting the stiffness of actuated joints

depending on the walking terrain [73, 74, 75]. A successful approach for the HAR of patients with no residual neuromuscular peripheral activities (e.g., patients with spinal cord injury) is represented by brain machine interfaces (BMIs) for triggering gait initiation and termination and steady walking tasks [76, 77, 78]. Nevertheless, the BMI complexity limits their application in daily-life ambulation. Therefore, commercial lower limb orthoses for patients with spinal cord injury are often controlled monitoring mechanical feature of the human-exoskeleton system, such as the tilting of the trunk [79, 80]. Others proposed approach for the activity recognition with lower limb active orthoses is presented in a study [81] to identify locomotion-related activities of daily living in healthy or mildly impaired people with residual movement capabilities. The algorithm is based on a fuzzy-logic classifier operating on signals acquired from the on-board mechanical sensors (hip joint potentiometers) and an IMU (for foot contact detection) integrated in the backpack of a fully portable hip exoskeleton. The activity classification is performed with an overall accuracy rate of 97.4%. Despite the high accuracy rate, the classifier was tested only for self-selected cadence and under the zero torque mode of the orthosis. The kinematics alteration induced by the users walking pace or the robot assistive actions were misregarded in the current state of the art.

2.2.1   Impedance control strategy

The information from the mechanical sensors can be used with an appropriate set of classifiers, to detect the desired gait mode (e.g. walking, stair climbing, etc.) or to separate different phases of the gait cycle. Each of the states in which the gait cycle is divided, is specified by constraints on knee joint kinematics and is associated to a set of constant impedance parameters. Once the controller enters a specific state, the impedance models parameters are modified according to the new states

set of parameters. In particular, the impedance model is chosen to match human reference joint torque and position trajectories. The transitions between states are defined by parametric laws that are heuristically chosen based on a prototypical gait cycle. The FSM has been implemented by many different groups and with a wide variety of devices, i.e. Varol et al. applied it to the Vanderbilt leg at RIC [82, 83, 46], Gorsic et al. apply it to the CYBERLEGs ankle-knee prosthesis [63], Hoover et al. to the prosthetic knee at Clarkson University [84], Liu et al. to the Kanazawas ankle prosthesis [85]. At ETH Zurich, Pfeifer et al. implemented for the first time on the ANGELAA knee exoprosthesis a FSM impedance control for level ground walking and stair ascent/descent [86]. Here, FSM divides the gait cycles in four states, each associated to a set of constant knee impedance parameters.

FSM exhibits sharp changes in impedance parameters when gait phases changes. This may cause discomfort to the user and reduce the assistance efficiency offered by the wearable robot. Therefore, in this dissertation, an approach is proposed to smooth the impedance parameters between the gait phases. For this, the activity recognition and gait phase detection modules are integrated into high level control of the wearable robot. A Gaussian mixture model (GMM) is employed to map the fuzzy likelihood of various activities and gait phases to the desired robot virtual impedance.

2.2.2   Adaptive oscillators based control strategy

In phase plane control, the desired system state, called invariant trajectory i.e. position and velocity, is expressed as a function of gait phase and stride length. For instance, in the prosthetic ankle developed by Holgate et al. [87], a gyro sensor is used to measure shank angular velocity and position w.r.t. the ground, and from it a phase plot is generated. The phase plot represents the direct relation between the current shank angular position and velocity and the desired gait phase and step

length/velocity, also called invariant trajectory. Gregg et al. apply this control to the Vanderbilt leg at RIC and state that the relation found in the phase plot can be considered independent of time, gait speed and ideally subject [88]. The advantage of this control strategy is the possibility of automatic speed or step length adaptation during the gait cycle. Yifan et al. estimate the phase during walking with a robotic ankle calculating cross correlation between past measurements and a learned model of the gait position [89]. The phase oscillator is used to add energy during running with the Pogo suit [90]. In this, sine of the phase angle is used as a forcing function which produces a stable limit cycle.

Revzen et al. develop the theoretical frame to estimate the phase of multiple synchronized oscillators and use it in biological processes including walking. They define the process as stochastic with an underlying oscillatory behavior. They accomplish a good estimation of the phase and reduce the noise from the sensor at the same time transforming the data using single value decomposition and principal component analysis to improve the estimate [91, 92]. Seo et al. [93] uses an adaptive frequency oscillator to assist the hip during gait. They use a series of adaptive frequency oscillators to estimate the state of the phase angle and then, use a multidimensional table to select what kind of torque assistance they provide given the estimated value. They show that this system can reduce the metabolic cost during walking, however since it is a learning approach, it means that at the beginning of the process or after a sudden change, the estimated value of the gait phase and the real angle are not close to the actual value. This approach needs several sampling periods to converge to the real value. A. Jan Ijspeert et al. [94, 95, 96] also uses a phase based oscillator to provide assistance to periodic motions. In their case, they synchronize adaptive oscillators with the external signal, and then estimate position and velocity. The estimated states are used to compute control signals that are then

used to force the system to follow a behavior [94, 95, 96].

The adaptive oscillator is capable of learning the parameters of the new signal with it's complex architecture. However, during the transitions, this architecture takes some time to learn the parameters of the new signal. This may cause delay in providing controller input. Therefore, a solution is needed to account for the transition of the activities and provide controller input as soon as possible. Therefore, in this dissertation, this problem is addressed by integrating activity recognition module to the phase based oscillator to assist in various activities such as walking, going upstairs, or running.

Chapter 3

HUMAN ACTIVITY RECOGNITION USING SMART SHOES AND INERTIAL
MEASUREMENT UNITS

This chapter presents an intelligent fuzzy inference (IFI) algorithm using inertial measurement units (IMUs) and smart shoes to recognize human activities. IFI algorithm recognizes the activities based on ground contact forces (GCFs) and the knee joint angles. The smart shoes are designed to measure GCFs exerted by the wearer. A total of four IMUs are mounted on bilateral thighs and shanks to provide acceleration and angular rate data. To calculate knee flexion extension, a calibration procedure is adopted which eliminates the need for an external camera system. Then, an extended Kalman filter (EKF) is used to estimate the relative orientations of thigh and shank segments, from which knee angle is calculated. Random forest search (RFS) technique is used as a baseline to compare with the performance of the IFI algorithm.

To evaluate the performance of this algorithm, several outdoor experiments are conducted on two healthy subjects for six activities including sitting, standing, walking, going upstairs, going downstairs and jogging. The results show that the algorithm is capable of classifying six activities with higher precision and less update time compared to the baseline approach for both subject dependent and independent tests. Also, the algorithm detects transitions between all the activities smoothly such as sit-to-stand or stand-to-walk with higher precision.

This chapter is organized as follows: section 3.1 discusses about the GCFs measurement using smart shoes, implementation of hysteresis compensator to compensate for the hysteresis effect in pressure sensor readings. Section 3.2 gives information

about the procedure followed to measure bilateral knee angles using IMUs. Section 3.3 details about the baseline algorithm used to compare the proposed approach. The proposed approach (IFI algorithm) is discussed in section 3.4. The experiments and results of the baseline and proposed approach is given in section 3.5.

3.1 Ground Contact Forces Measurement using Smart Shoes

This section reviews the design of smart shoes, a wearable device that measures GCFs for gait analysis. Smart shoes utilize four coils of silicone tubes adhered directly underneath the shoe insole at key points of interest. Air pressure sensors connect to each tube coil to measure pressure changes caused by compression. The static and dynamic calibration performed on each sensing coil to establish a model of internal pressure and the GCF. Based on the model, a phase lead filter is designed to account for the hysteresis effect and visco-elastic properties of the silicone tube in order to provide accurate GCF measurements. To design this filter, the air bladder is modeled using a standard linear solid (SLS) model. The prediction error minimization (PEM) algorithm is then implemented to identify the continuous-time transfer function of this SLS model, which is then transformed to discrete time domain to implement in a digital processor. Mechanical characterization and testing on a healthy subject are performed to validate the model and its capability to compensate for hysteresis in GCF measurement.

3.1.1 Design of sensing unit in smart shoes

In an effort to obtain accurate results, a new sensing unit is made prior to smart shoe testing. This sensing unit is constituted by an air bladder made by winding silicone tubes and an air pressure sensor. When designing the sensing unit, considerations are made according to three questions. First, what sensor apparatus is best

21
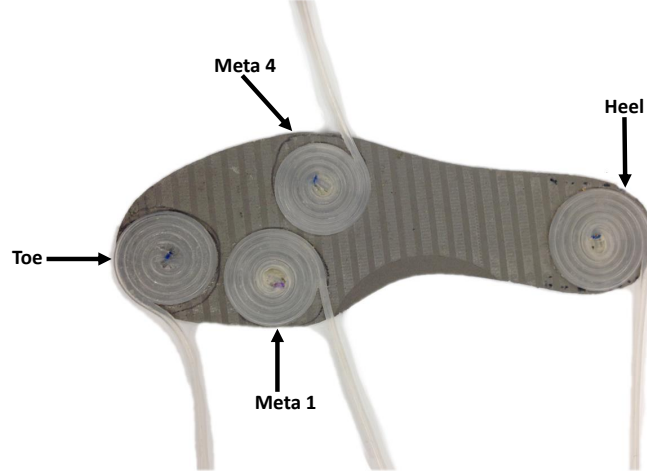
(a) Shoe insole with four air bladders
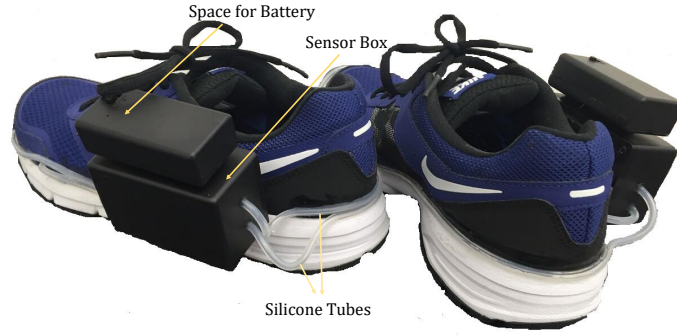
(b) Smart shoes with sensing unit

Figure 3.1: Wireless smart shoes with shoe insole consisting of coiled silicone tubes at heel, toe, inner and outer metatarsals.

used to measure distributed GCFs. Second, how and of what the apparatus is made. Third, how the received data are processed and stored.

Taking survey of existing solutions, FSRs are the typical means for GCF measurement. However, FSRs perform poorly due to their nonlinearity, lacking durability and lacking capability to measure distributed loads common in most any gait. An alternative solution utilizing air pressure sensors proposed by Kong et al. offers linearized readings, increased durability and better measurement of distributed loads [97]. Tube is coiled and adhered to the underside of a shoe insole under the toes, inner and outer

two metatarsals, and heel as shown in Figure 3.1(a). The coils function as air bladders and connect to air pressure sensors. When loaded different, during a step for instance, the tube coils are compressed, generating pressure which, in turn, is measured by the air pressure sensors. In this system, GCF is calculated from the pressure in the tube coils. Certain assumptions are made, including the lack of radial deformation and dynamic effects within the air bladder. Based on these assumptions, pressure change is proportional to force applied i.e., $F(t) = \frac{P(t)}{A(t)}$.

Silicone tube and unidirectional gauge pressure sensors are used to construct the previously described apparatus. Silicone tube is selected for use due to its minimal creep [97] and desirable stiffness, rigidity and toughness. Unidirectional gauge pressure sensors from First Sensors HDI series are used. Pressure sensors with 200 mbar measurement range connect to tubes coiled under the heels and metatarsals. Toes sustain less of a load than the heels and metatarsals. Therefore, 100 mbar pressure sensors are connected to the tubes coiled underneath the toes for higher resolution. The sensor box provides housing for the four air pressure sensors on each shoe as shown in Figure 3.1(b). The air pressure sensors connect to a microprocessor which reads their output voltage through bluetooth and communicates them to a computer. The computer, then, processes and analyzes the data. The sampling rate of the smart shoes can go up to 100 Hz with bluetooth module.

3.1.2   Calibration test setup

Testing apparatus and configuration

Calibration testing apparatus is comprised of the sensing unit itself, an Instron 5944 mechanical testing machine and a National Instruments myRIO. As shown in Figure 3.2, the sensing unit lays on an anvil, the Instron machine applies compressive load to

the tube coils, and the myRIO measures analog output from the air pressure sensors. In testing, the Instron machine is outfitted with a 1 kN load cell capable of applying compressive and tensive loads. Test instructions are sent to the Instron machine by Bluehill 3 software run on a nearby computer. The myRIO receives analog input from the Instron and air pressure sensors and sends it to another nearby computer via LabVIEW. To accurately deduce GCFs from pressure readings in practice, the relationship between pressure readings and load on each sensing node must be established and the dynamic characteristics of each sensor type must be determined. To achieve this, individual calibration tests are performed featuring static and dynamic loading. Figure 3.3 displays one example of data received during a static calibration test.

In static testing, the Instron machine applies a compressive load to individual tube coils, maintains that load for five seconds, then removes load. The test performs this process for loads from 50N to 800N in 50N intervals. Static tests are conducted for all 8 sensing nodes. Due to dynamic effects, load values obtained during loading do not represent load values in equilibrium. Therefore, they do not remain constant when compression is halted. Slower loading allows the system more time to normalize, keeping it closer to equilibrium. The static calibration procedure is described in Figure 3.4(a).

In dynamic testing, the Instron machine applies compressive load at various rates. The system begins unloaded, then Load is applied at a specified rate. When 800N load is applied, unloading begins. Load is reduced at 50N/s until the system is unloaded again. This cycle is repeated for loading rates of 50, 100, 200, 400 and 800N/s. The steps followed for dynamic calibration is shown in Figure 3.4(b).
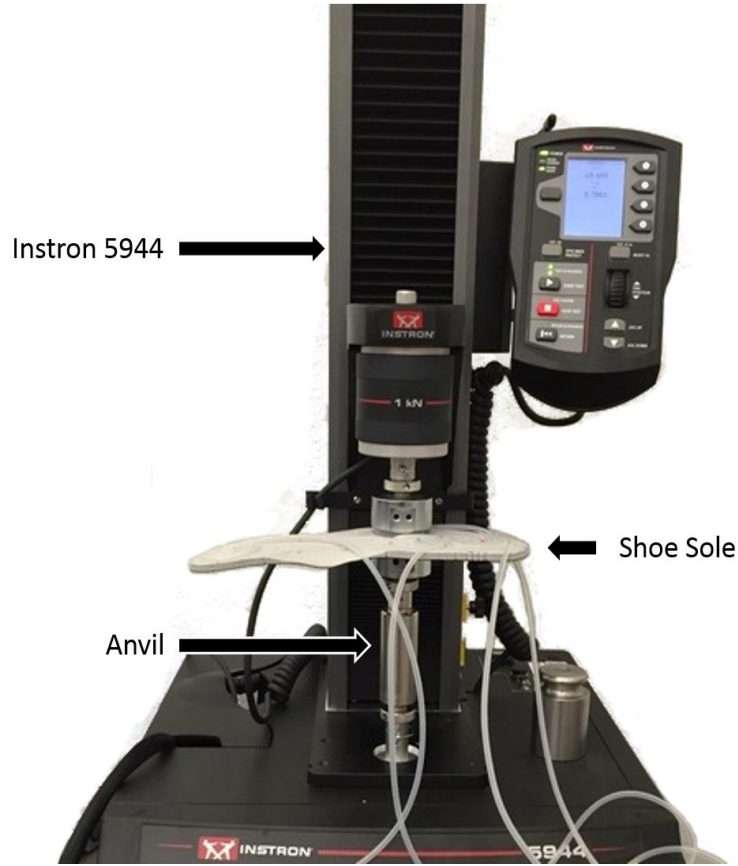
Figure 3.2: Setup for static and dynamic calibration tests: Instron 5944 material testing machine and shoe insole

Discussion on calibration test results

At the first stage of the process, calibrated weights were statically placed over tube coils in order to obtain the relationship between applied force and the pressure change i.e., output voltage of the circuit. These methods of loading range of weights and increment between each reading is chosen in such a way that remains within the limits of the sensor. Thus, by using test setup, loads are increased from 0 to 800N with the waveform shown in the Figure 3.3. Most importantly, Figure 3.3 illustrates the linearly proportional relationship between applied load and recorded pressure in static load conditions. Minor hysteresis is observed during load changes as apparent
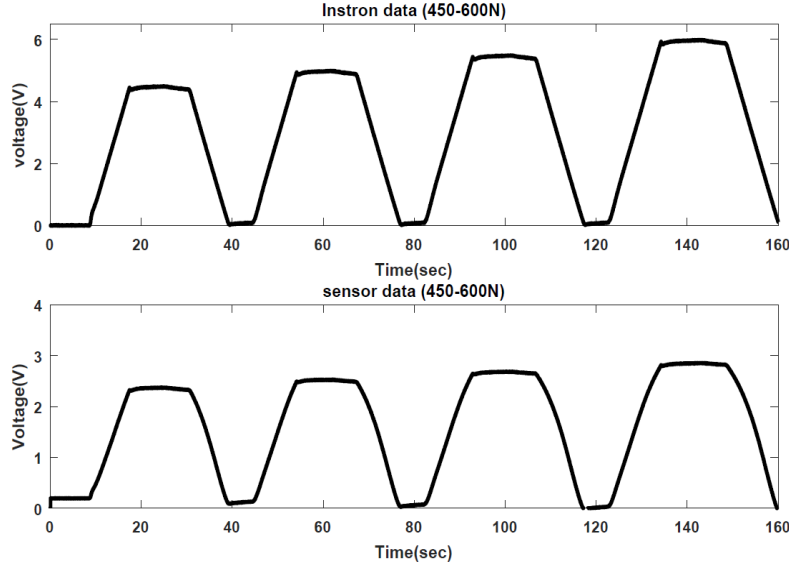
Figure 3.3: Static test (Loading range:450-600 N): voltage output from Instron and air pressure sensor

in the bowed lines during bulk loading and unloading in Figure 3.3(b).

For the dynamic test, triangular waveform of loading and unloading is generated by Instron machine at variable loading rates from 50N/s to 800N/s as shown in the Figure 3.5(a). Hysteresis is observed during loading and unloading the air pressure sensors. The sensor follows upper side of the curve during loading and lower side of the curve during unloading as shown in Figure 3.5(c) and 3.5(d). Hysteresis effect increases with higher rate of loading. Comparison of hysteresis effect at low and high speed of loading are shown in Figure 3.5(c) and 3.5(d).

3.1.3   Approach for designing hysteresis compensator

The approach is to design a physical model based hysteresis compensator capable of improving GCFs measurement and performance of the sensing unit especially during dynamic situations characterized by rapid changes in force. This makes sensing

26
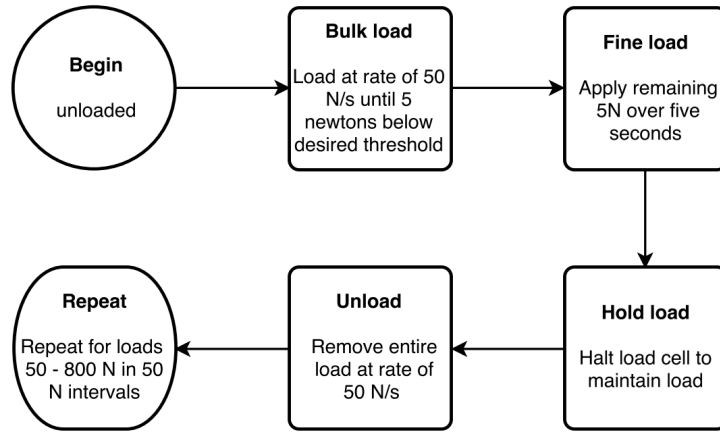
(a) Steps for static calibration test
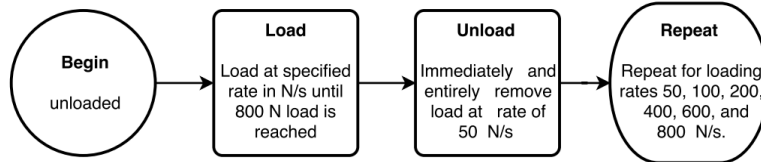
(b) Steps for dynamic calibration test

Figure 3.4: Calibration test procedure

suitable for dynamic activities such as walking, jogging and running. The approach followed to design such a filter is explained in three steps: 1) Develop a dynamic model for the air bladder system. 2) Determine the continuous time transfer function of the physical model on the basis of the input and output data measured in time domain. 3) Transform the continuous time transfer function into discrete time domain for implementation in a digital processor.
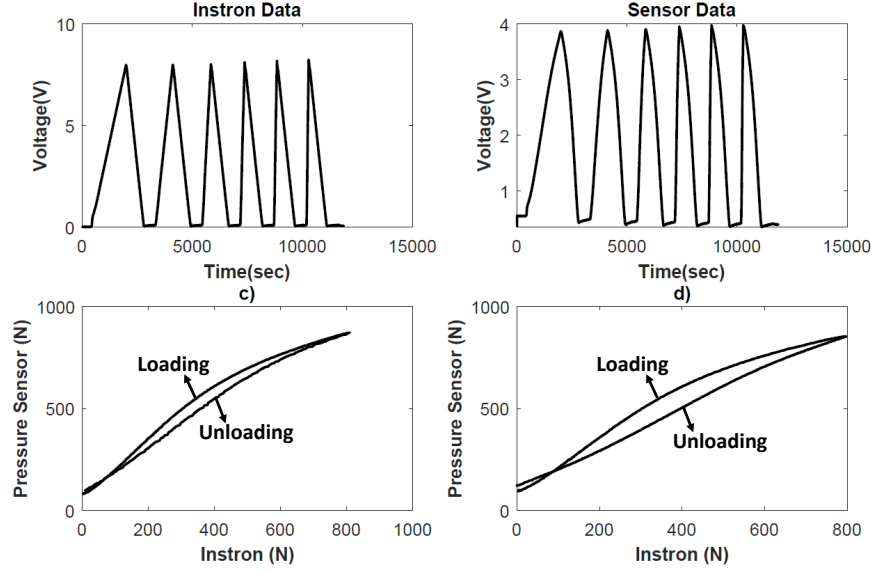
Figure 3.5: Dynamic testing for rate of loading (50-800 N/s): voltage output from Instron and air pressure sensor. (c) low speed (100 N/s) (d) high speed (800 N/s)
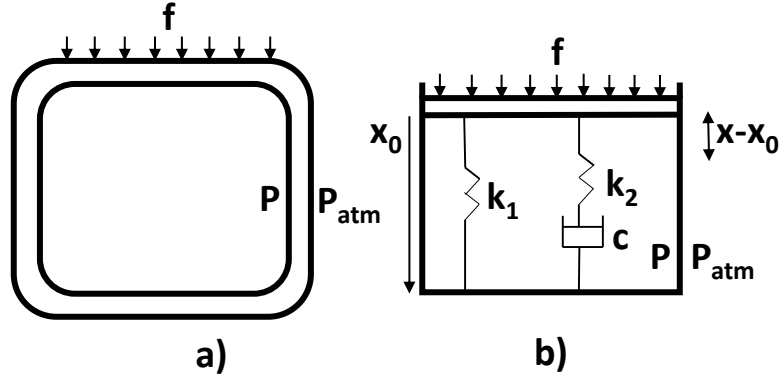
Figure 3.6: a) Silicone tube model b) Standard linear model

Dynamic model for air bladder

In order to accurately capture the dynamic characteristics of the air bladder system, a standard linear model is employed, which is used for modelling visco-elastic materials such as silicone tubing [97]. This model consists of one damper and two Hookean springs, one connected in parallel and another in series. The air bladder and equivalent standard linear model are shown in Figure 3.6. It is assumed that there are no

28

inertia and air leakage in the air bladder. Therefore, mass M is taken to be zero. The force balance equation for air bladder system is:

$$(P - P_{atm} - f)A - k_1(x - x_0) + \frac{k_2 cs(x - x_0)}{k_2 + cs} = 0, \qquad (3.1)$$

Here P and P_{atm} are the absolute and atmospheric pressure, A is the effective area of the air bladder which is assumed to be constant. $x - x_0$ is the deformation in the tube. s is the derivative operator as (3.1) is in the Laplace domain. Force applied on the air bladder is assumed to be uniformly distributed over the area. Therefore, total force applied $F(t) = f(t)A$. Gauge pressure P_G is the difference between P and P_{atm}. The governing transfer function between the force applied and gauge pressure is derived in [97]:

$$F = P_G + \frac{k_2 cs}{k_2 + cs} \frac{x_0^2}{nRT} P_G \equiv \frac{b_1 + b_2 s}{a_1 + a_2 s} P_G, \qquad (3.2)$$

where

$$a_1 = k_2, a_2 = c, \qquad (3.3)$$

$$b_1 = k_2 [1 + k_1 \frac{x_0^2}{nRT}], b_2 = c[1 + (k_1 + k_2) \frac{x_0^2}{nRT}]. \qquad (3.4)$$

Physical properties of the silicone tube are as follows: $n = 4.2075 \times 10^{-9} [mol], R = 8.3145 [m^3 pak^{-1} mol^{-1}], T = 300k$ and x_0 is the inside height of the undeformed silicone tube which is 2 mm in our case. Here, P_G is available from the air pressure sensor. However, in order to get load measurement, we need to multiply the pressure change with the area of cross section, which it is not easy to calculate. Because, it is difficult to calculate actual effective area of cross section for distributed load. Thus, it becomes important to identify the relationship between applied force and pressure change in order to estimate applied force F from the pressure sensor readings. As a

result, the coefficients a_1, a_2, b_1 and b_2 in (3.2) need to be determined to establish first order transfer function for the dynamic model.

3.1.4 Prediction error minimization (PEM) algorithm

To identify the coefficients of the first order transfer function, a PEM approach is applied. The main objective of this algorithm is to minimize the weighted norm of the prediction error which is the difference between measured and predicted output. This algorithm basically performs two steps to estimate the coefficients: 1) initialize parameters and 2) update parameters.

Initialization of coefficients for transfer function

To initialize numerator and denominator of the first order transfer function, Simplified Refined Instrumental Variable method for Continuous time systems (SRIVC) algorithm is employed [98]. SRIVC is one of the successful stochastic identification method where the noise $w(t)$ is assumed to be discrete-time, white noise process $w(t_k) = N(0, \sigma^2)$ so that no explicit noise modeling is necessary. In this algorithm, instrument variables which are correlated to system input, not to system noise are employed.

True system model

The input $u(t)$ and output $x(t)$ sampled data are available in time domain from air pressure sensors and Instron, respectively. The operator polynomial representation of the true system for input $u(t)$ and output $x(t)$ is

$$A(s, \theta^*)x(t) = B(s, \theta^*)u(t), \tag{3.5}$$

$$y(t) = x(t) + w(t). \tag{3.6}$$
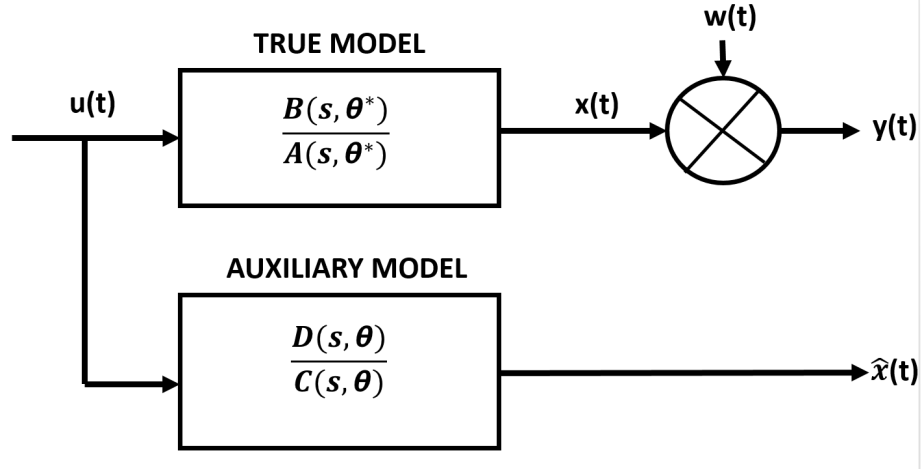
Figure 3.7: Representation of true and auxiliary model

Where $y(t)$ is the measured output with white noise $w(t)$. The operator polynomial is in the Laplace domain and true parameter θ^* can be defined by

$$A(s, \theta^*) = a_n^* s^n + \ .... + a_1^* s + 1, \tag{3.7}$$

$$B(s, \theta^*) = b_m^* s^m + \ .... + b_1^* s + b_0^*, \tag{3.8}$$

$$\theta^* = [a_n^* \quad a_{n-1}^* \quad ....a_1^* \quad b_m^* \quad b_{m-1}^* ....b_0^*]. \tag{3.9}$$

From (3.2), our system should consist of one zero and pole. Therefore, $n=m=1$ which gives

$$A(s, \theta^*) = a_1^* s + 1, \tag{3.10}$$

$$B(s, \theta^*) = b_1^* s + b_0^*, \tag{3.11}$$

$$\theta^* = [a_1^* \quad b_1^* \quad b_0^*]^T. \tag{3.12}$$

Transfer function T for the true system for the true system representing dynamic model with input $u(t)$ and output $x(t)$ is

$$T = \frac{x(t)}{u(t)} = \frac{b_1^* s + b_0^*}{a_1^* s + 1}. \tag{3.13}$$

31

By comparing (3.13) and (3.2)

$$a_1^* = \frac{a_1}{a_2}, \quad b_0^* = \frac{b_2}{a_2} \quad and \quad b_1^* = \frac{b_1}{a_2}. \tag{3.14}$$

Let us assume that the value of $a_2 = 1$ which means the value of c becomes equal to 1 from (3.3). Further, this assumption is valid since the coefficients k_1, k_2 and c are coupled, the value of $c = 1$ results in one set of values for k_1 and k_2. The increment or decrement in c changes k_1 and k_2 values accordingly. For our case, c is assumed to be one. Thus, the problem of estimating three coefficients automatically reduces to two i.e., to estimate k_1 and k_2 only. Therefore, coefficients a_1^*, b_0^* and b_1^* need to be estimated in order to identify the continuous-time transfer function for the true system i.e., the dynamic model of air bladder and the sensor.

Auxilary model

To estimate system parameter vector θ^* from sampled input and output, SRIVC method creates an auxiliary model as shown in Figure 3.7. This is an approximation of the true system which takes the input $u(t)$ and estimates the output $\hat{x}(t)$ with no noise. The auxiliary model approximating the true system equations (3.10) to (3.12) is:

$$y(t) = \frac{D(s, \theta)}{C(s, \theta)} u(t) + e(t), \tag{3.15}$$

$$e(t) = y(t) - \phi^T(t)\theta, \tag{3.16}$$

$$\phi(t) = [-\frac{dy(t)}{dt} \quad \frac{du(t)}{dt} \quad u(t)]^T, \tag{3.17}$$

$$\theta = [a_1^- \quad b_0^- \quad b_1^-]^T. \tag{3.18}$$

Here, a_1^-, b_0^- and b_1^- are the estimates for a_1^*, b_0^* and b_1^* in (3.14). The single input, single output (SISO) model in the continuous time domain is algebraically equivalent to the discrete time SISO model explained in [99]. The equation containing error

32

function $e(t)$ in (3.16) can be written as

$$e(t) = \frac{1}{C(s,\theta)}[C(s,\theta)y(t) - D(s,\theta)u(t)], \tag{3.19}$$

$$Z(s) = \frac{1}{C(s,\theta)}. \tag{3.20}$$

where $Z(s)$ is given by pre-filter. In SRIVC method, the state variable filter (SVF) proposed by young (1964) is used as a prefilter. The minimal order SVF has the form [100]:

$$Z_{svf}(s) = (\frac{\beta}{s+\lambda})^n, \tag{3.21}$$

where n is the system order and filter time constant λ is apriori and usually $\lambda = \beta$. Now, taking $Z(s)$ in (3.20) inside the square bracket (3.19), error function $e(t)$ becomes

$$e(t) = C(s,\theta)y_f(t) - D(s,\theta)u_f(t), \tag{3.22}$$

$$y_f(t) = \frac{y(t)}{C(s,\theta)}, \quad u_f(t) = \frac{u(t)}{C(s,\theta)}. \tag{3.23}$$

The derivative of $y_f(t)$ and $u_f(t)$ is given by:

$$y_f^{(i)}(t) = f_i(t) * y(t) \quad i = 0, 1, \tag{3.24}$$

$$u_f^{(i)}(t) = f_i(t) * u(t) \quad i = 0, 1. \tag{3.25}$$

Here $y_f^{(i)}(t)$, $u_f^{(i)}(t)$ are the i_{th} derivative of $y_f(t)$ and $u_f(t)$ respectively. i is 0 and 1 in our case. $*$ is the convolution operator and filters take the form,

$$f_i(t) = L^{-1}(\frac{s^i}{C(s,\theta)}), \tag{3.26}$$

where L^{-1} is the inverse Laplace transform. Therefore, the auxiliary model at the n_{th} sampling instant $t = t_n$ can be written as

$$e(t_n) = y_f(t_n) - \phi_f^T(t_n)\theta, \tag{3.27}$$

$$\phi_f(t_n) = [-\frac{dy_f(t_n)}{dt_n} \quad \frac{du_f(t_n)}{dt_n} \quad u_f(t_n)]^T. \tag{3.28}$$

To obtain an initial estimate of θ for a data sample of length N, the following equations are used:

$$V_N = \frac{1}{N}\sum_{i=1}^{N}\phi_f(t_i)\phi_f^{\mathrm{T}}(t_i), \tag{3.29}$$

$$\theta = V_N^{-1}\frac{1}{N}\sum_{t=1}^{N}\phi_f(t_i)y(t_i). \tag{3.30}$$

The prefilter in SRIVC method provides $C(s,\theta)$ from the user defined λ. From equations (3.29) and (3.30), initial value of θ can be estimated.

Updating coefficients of transfer function

Nonlinear least square search method is employed to iteratively adjust the unknowns in true system (3.6), as well as estimate of the instrument variable at each iteration of the algorithm, until that converges. Instrument variable at each iteration is given by

$$\hat{x}(t) = \frac{D(s,\theta)}{C(s,\theta)}u(t). \tag{3.31}$$

Here, θ is the estimated vector obtained at the previous iteration. Estimating coefficients of θ, a_1^-, b_1^- and b_0^- in (3.18) can identify the values k_1, k_2 and c given in (2). However, we considered c is always equal to 1.

To update the initialized parameters for the transfer function, a set of non-linear least squares search methods Gauss Newton[101], Levenberg Marquardt[102, 103] and trust region reflective Newton [104] from the system identification toolbox MATLAB R2015b were adopted. Trust region based search methods are chosen in our approach because they have better convergence properties than regular line search method [105]. The main objective of these search methods is to reduce the error $e(t)$ given in (3.16) by minimizing weighted prediction error norm.

Algorithm summary

a) Input:$y1(t)$ and $y2(t)$

where $y1(t)$ and $y2(t)$ are the load measurement data available from Instron and air pressure sensor in time domain sampled at 100 Hz. For our test, data is collected at 100Hz.

b) Prediction Error Minimization :

1. Define a value for filter time constant λ and maximum tolerance value μ.

2. Apply SRIVC method, to find the initial condition of θ which is the estimate of the continuous system parameter vector θ^* from sampled input-output data using (30) and (31).

3. Update the value of θ on the basis of cost function using non-linear least square search method. The cost function is a positive function of prediction error e(t) given in (17). for a model with n number of y outputs, the cost function has the following general form:

$$C(\theta) = \frac{1}{N}\sum_{t=1}^{N}e^{\mathrm{T}}(t,\theta)We(t,\theta), \qquad (3.32)$$

where N is the number of data samples, $e(t,\theta)$ is n-by-1 error vector at a given time t, parameterized by the parameter vector θ and W is the weighting matrix. It is fixed and does not depend on θ.

4. Repeat step 3 until the maximum relative percentage of the estimated parameter θ in successive iterations is less than the tolerance value μ defined in first step.

c) Continuous to discrete time domain transform: continuous time transfer function obtained from PEM method is discretized using bi-linear transformation

for the real time implementation.

d) output: $f(t)$, which is the filtered signal of $y2(t)$.

3.1.5   Implementation of phase lead filter

Two types of air pressure sensors with range 100 mbar and 200 mbar are used in smart shoes. The sensor with 100 mbar range is used for toe sensing point and other with 200 mbar range for all other sensing points. The dynamic calibration tests were performed on sensors at left toe, left heel, right toe and right heel. The load measurement data are available simultaneously from the air pressure sensor and Instron at the sampling rate of 100 Hz. This collected time sampled data from the air pressure sensor and Instron are used as input and output in our proposed algorithm to identify the transfer function.

Trust region reflective Newton (TN) search method showed better performance compared to Gauss newton (GN) and Levenberg Marquardt (LM) search methods in terms of fit percentage. For instance, in left toe data simulation, TN method exhibited 90.32 % while LM and GN showed 83.12 % and 78.26 % respectively. Therefore, trust region reflective newton method search method was employed to identify the transfer function.

The identified values for k_1, k_2 and c of (3.4) are displayed in Table 1 along with their transfer fuction equations for four sensing points separately. There are certain points that can be inferred from Table 1:

1. If $k_1 = k_2 = 0$ or nearly equal to zero, this explains that the material exhibit less or weak visco-elastic effect and no signal processing is required. From Table 1, it is clear that the coefficients k_1, k_2 and c of any sensing units are not zero or close to zero. It means that the material exhibits considerable visco-elastic

36

effect. Therefore, it becomes necessary to carry out signal processing on the raw data.

2. If $k_1 \gg 0$, it means the material is stiff and noise will be amplified. From Table 1, it is clear that the value of k_1's are in the range from 1.341 to 2.025. This implies that material exhibits considerable stiffness and noise gets amplified over time.

3. If the pole and zero are negative, signal does not show drift. From Table 1 and using equations from (3.2) to (3.4), we can deduce that poles and zeros are negative. Therefore, it can be inferred that the filtered signal will not show drift.

4. If the magnitude of the pole is greater than zero i.e., $|\frac{a_1}{a_2}| > |\frac{b_1}{b_2}|$, the transfer function magnifies the high frequency range of the measured signal. The magnitude of the poles are greater than zeros which implies filter designed on the basis of this transfer function will show magnifying characteristics in the high frequency range with the phase lead.

The filter exhibits magnifying characteristics in the high frequency range with the phase lead. The performance of the hysteresis compensator designed for left shoe sensing unit can be seen in Figure 3.8. Filtered signal shows improved linearity in measurements with reduced hysteresis compared to raw signal. A variance level of 2.23N in root mean square is observed in the filtered signal which is nearly 0.3 percent of total load applied i.e., 800N. The root mean square error (RMSE) metrics are used to compare between the filtered and raw signal.

Root mean square error (RMSE) metrics: a) RMSE between load measurement from Instron $x(t)$and raw data measurement $u(t)$ from air pressure sensors. b) RMSE

37

Sensing unit	k_1	k_2	c	Transfer function
Right toe	1.873	0.119	1	$\frac{2.269z-2.267}{z-0.9988}$
Right heel	2.045	0.159	1	$\frac{2.284z-2.281}{z-0.9984}$
Left toe	1.341	0.215	1	$\frac{2.224z-2.221}{z-0.9979}$
Left heel	2.025	0.316	1	$\frac{2.355z-2.349}{z-0.9968}$

Table 3.1: The transfer function equation and coefficients of the physical model for four sensing units

between load measurement data from Instron $x(t)$ and filtered signal $r(t)$ after applying hysteresis compensator. c) Improvement percentage $P\%$ can be defined as $\frac{RMSE(u)-RMSE(r)}{RMSE(u)} \times 100$.

where

$$RMSE(u) = \sqrt{\frac{\sum_{i=1}^{N}(x_i - u_i)^2}{N}}, \tag{3.33}$$

$$RMSE(r) = \sqrt{\frac{\sum_{i=1}^{N}(x_i - f_i)^2}{N}}. \tag{3.34}$$

where N is the total number of data samples.

Table 3.1.5 displays the calculated metrics for four sensing units individually. Instron generated triangular waveform of loading range 0 to 800N with loading rates 100, 200, 400, 600 and 800N/s. This table compares filtered and raw data in terms of $RMSE$ metrics. Improvement percentage ($P\%$) reveals the improvement seen in the filtered signal after designed filter is applied. It is clear from the range of $P\%$ that filtered signal shows less RMSE value compared to raw signal. These filters provide better performance at lower rates of loading than at higher speeds. For instance, considering left toe sensing unit, the $P\%$ is 75.36% at 100 N/s and reduces to 68.27%
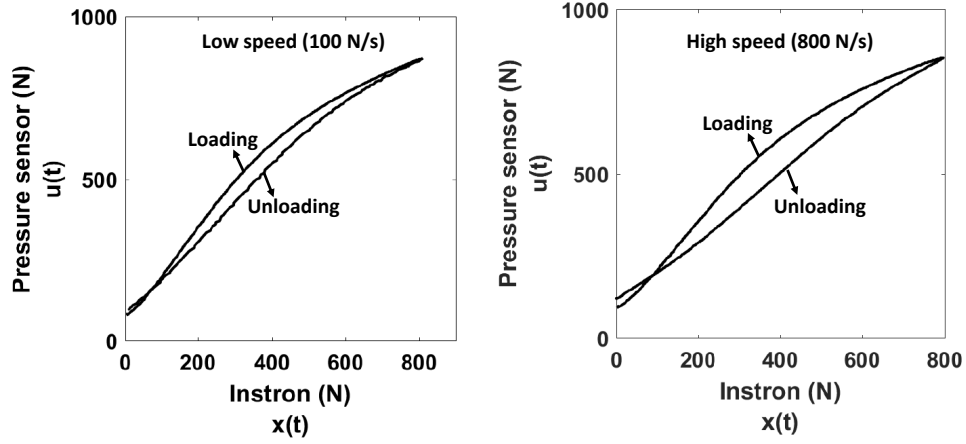
(a) Raw signal at low (100 N/s) and high (800 N/s) speeds.
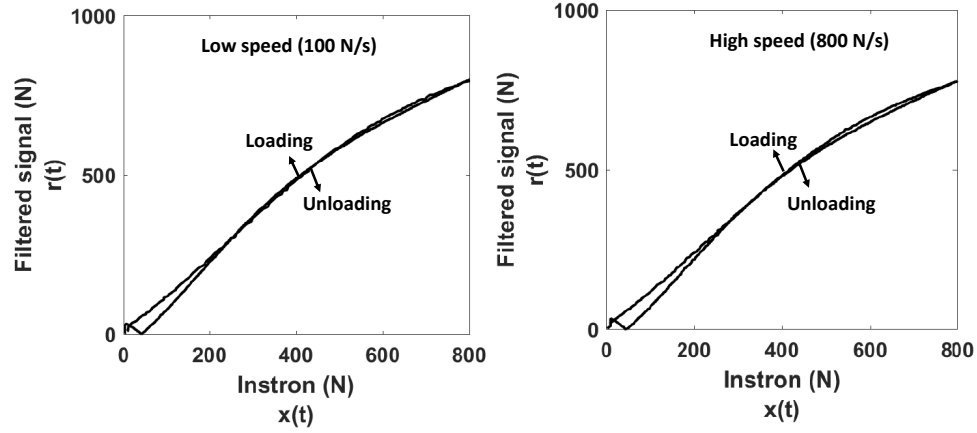
(b) Filtered signal at low (100 N/s) and high (800 N/s) speeds.

Figure 3.8: Left toe sensing unit hysteresis compensator performance

at 800 N/s. Even though $P\%$ decreased with an increase in loading rates, filter exhibited sufficient compensation in hysteresis for varying loads as shown in Figure 3.8(b). Filtered signal shows better linearity with less hysteresis at both low and high speed.

3.1.6 Experimental validation of hysteresis compensator

To evaluate the performance of the proposed phase lead filter on the GCF measurements, Data were collected from various trails of walking and standing activities

Sensing unit	Metrics(N)	Rate of loading (N/s)			
		100.000	200.000	400.000	800.000
	RMSE($y1$)	137.059	140.291	144.217	144.514
Right toe	RMSE(f)	43.992	47.883	54.123	56.205
	P	3.116	2.929	2.670	2.565
	RMSE($y1$)	103.999	108.437	111.274	113.595
Right heel	RMSE(f)	31.421	33.076	35.625	38.2441
	P	3.309	3.278	3.124	2.970
	RMSE($y1$)	224.283	232.154	238.448	239.654
Left toe	RMSE(f)	55.272	64.159	73.185	76.0494
	P	4.058	3.618	3.275	3.135
	RMSE($y1$)	158.164	196.177	250.127	283.381
Left heel	RMSE(f)	37.435	54.354	74.259	88.221
	P	4.225	3.609	3.369	3.212

Table 3.2: Comparison between raw and filtered signal for different rate of loading performed by a healthy subject. The healthy subject is male, weight 53 kg, and is 5 feet 10 inch tall.

1) For the standing trail, subject initially did toe movement i.e., he stood on tip-toe. Then, he went back to the normal standing position and remained still for the whole trail. This activity was performed for a period of 60 seconds. Figure 3.9 shows the raw and filtered GCF estimate from sensing units during standing trail. Total GCF exerted by the subject is calculated for both raw and filtered data. Total GCF estimate i.e., sum of the GCF estimate of all the eight sensing units from raw data is 618N, where from filtered data, it is 535.2N. Therefore, subject weighting 53kg can normally exert 519.4N on the ground. Thus, the filtered signal provides more accurate estimate.
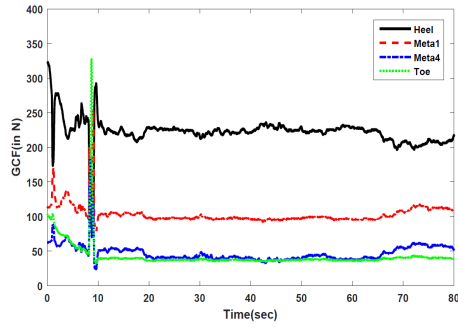
(a) Raw signal from left foot
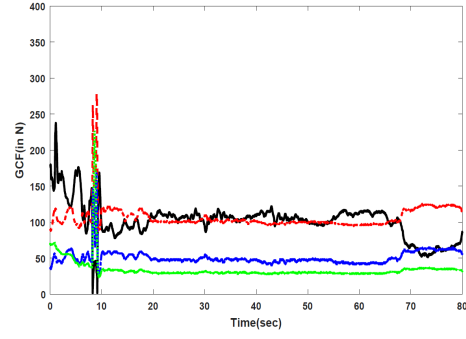
(b) Raw signal from right foot
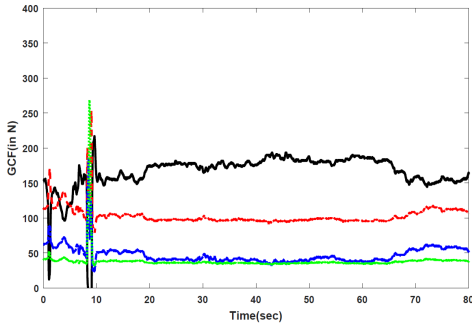
(c) Filtered signal from left foot
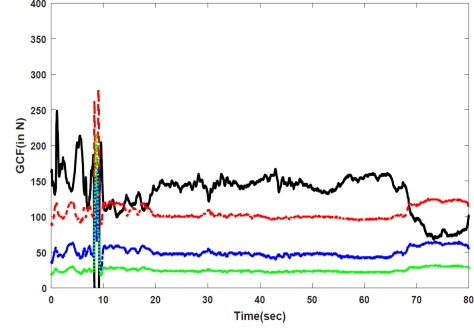
(d) Filtered signal from right foot

Figure 3.9: GCFs estimate plot for sensing units embedded in smart shoes for standing experiment

2) For the walking trail, subject performed continuous walking on treadmill for 2 minutes at a speed of 6 mph. Figures 3.10(a) to 3.10(d) show the performance of the hysteresis compensator for the walking trail. The raw data collected during this trail are processed using the designed filter and compared with raw data for the left shoe and right shoes. The plot is drawn between GCF estimate from all sensing units and time interval from 20 to 26 seconds. From Figures 3.10(a) to 3.10(d), it is observed that in each walking step, the subject initially touched the ground with the heel followed by Meta4, Meta1 and finally toe. It can also
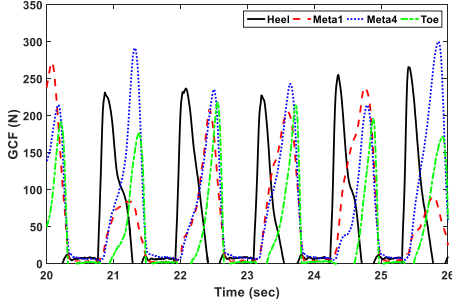
(a) Raw signal from left foot
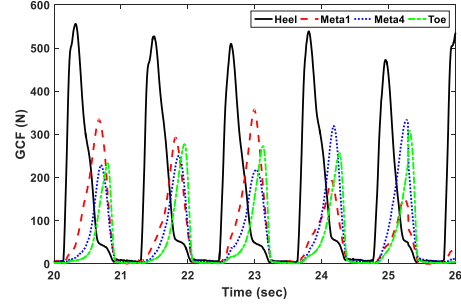
(b) Raw signal from right foot
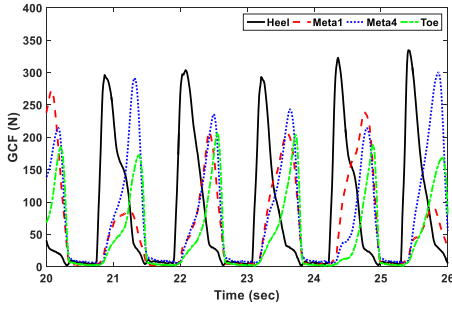
(c) Filtered signal from left foot
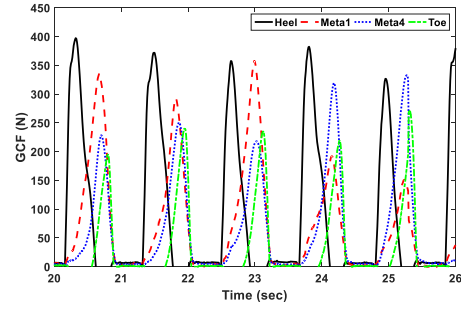
(d) Filtered signal from right foot

Figure 3.10: GCFs estimate plot from all sensing units embedded in smart shoes for walking experiment performed on treadmill (time range: 20-26sec)

be inferred from Figures 3.10(a) to 3.10(d) that the subject applied more force on the right side than left, and more specifically, right heel compared to left. Although, raw and filtered signal show similar GCF pattern during walking, differences can be observed in terms of the amplitude. For instance, from Figures 3.10(a) to 3.10(d), it can be seen that the filtered signal provides a lower estimate of heel GCF than the raw data. Now, reliable GCF measurements are achievable from smart shoes with the help of designed hysteresis compensator, the next step is to obtain knee angle measurements from IMUs.

3.2   The Knee Angle Estimation using IMUs

The procedure followed in the estimation of knee angle can be illustrated in two steps. First, the sensor frames are aligned using functional alignment procedure given in[106]. In the second step, an extended Kalman filter (EKF) estimates the relative orientation between IMUs.

The alignment of the sensor frames is done both vertically and horizontally with respect to joint coordinate system (JCS) given by [106]. For the vertical alignment with the JCS, the inertial data of the acceleration for still standing is required. In static conditions, gravity is prominent in acceleration signals. Therefore, the averaged gravitational vector is calculated for both thigh and shank frames. This is useful to calculate rotation matrices for z-axis of both the frames. For the horizontal alignment, the motion AA-rotation defined by Favre et al [106] is followed. The straight leg is lifted up and down laterally for approximately 30 seconds. This is useful to produce angular rate vectors in thigh and shank sensor frame. The misalignment angles can be detected easily by following this procedure. By using misalignment angles, rotation matrix about xy axis can be calculated which rotates the shank sensor frame around the already aligned z-axis to align with the thigh frame.

Two similar EKF given in [107] are implemented to estimate roll and pitch orientation of the two adjacent segments. The EKF used here is an eight-row state (acceleration and angular rate in three axis, roll and pitch) vector:

$$\vec{x} = \begin{pmatrix} \vec{a} \\ \vec{\omega} \\ \vec{\phi} \\ \vec{\theta} \end{pmatrix}$$

For this knee estimation algorithm, only roll and pitch components are taken

into consideration. Because yaw component of the gyroscope is the main reason for drifts in the output. The information related to equations of dynamic systems and observation model is described in detail in [107].

The orientations of the thigh and shank segments are estimated over time by the EKF. The rotation matrices obtained during the alignment are useful in aligning thigh and shank sensor frame with JCS.

3.3 The Baseline Algorithm: Random Forest Search

Random forest search (RFS) is used as a baseline algorithm to compare the performance of the proposed algorithm. Below are the reasons to choose RFS as a baseline:

- RFS takes less time to build the prediction model compared to other machine learning techniques such as SVM (Support Vector Machines) and neural networks [108].

- RFS gives good performance in terms of test accuracy.

- RFS is a very popular method used in human activity classification [109].

Data is available in discrete time series. It is not possible to identify the activity at a sample point as it takes time to complete an activity. Therefore, time window consisting of a certain number of samples is generally employed. Each segment gives an instance for human activity recognition. The fixed sliding window is a most commonly used segmentation approach for activity recognition. This approach divides the signal into fixed length segments. There are certain methods proposed to improve the fixed sliding window. One successful approach is overlapping sliding window approach. The length of the moving step determines the percentage of overlapping between adjacent windows. In this chapter, we adopt adaptive time window

44

approach as it divides the signal into segments whose moving step depends on period of the signal.

3.3.1   Autocorrelation based adaptive time window

Certain activities like walking, running, going upstairs and going downstairs are quasi-periodic. On the other hand, sitting and standing are non-periodic. Pre-classification is applied to separate periodic from non-periodic activities. The adaptive fixed sliding window uses fixed time segments to extract the period from periodic activities. Sliding step is determined from this period. To make the time window, we need to extract the period from these activities. At least data of two to three periods is needed to extract the period i.e., length of the window.

We use the auto-correlation method to extract the period for the time window. The basic principle of auto-correlation is that normalized auto-correlation function of a signal has the same period as the original signal[43].

3.3.2   Feature extraction

The classification algorithms cannot directly apply to raw data. Instead, raw data is first transformed into examples. The data contained in the segmented time window is considered as an example. In our case, the segmentation is performed by the adaptive time window. The data samples in this time window are used to calculate features. A total of 86 features is computed for this algorithm. The features used in the algorithm including acceleration and angular rate signals are variants of six basic features: average for each axis (six), standard deviation (six), average absolute difference (six), average resultant acceleration (two), time between peaks (six), and binned distribution (sixty). These are the basic time domain features and all are important for a classification algorithm [41]. Also, we tried to include other time

45

domain features such as zero crossing rate and linear correlation coefficient and did not notice any difference in classification results. The inclusion of frequency domain features such as spectral centroid and spectral flux showed little improvement of 1 to 2 % in test accuracy but at the cost of computation time. Therefore, we used variants of six basic features in this RFS algorithm.

3.3.3   Random Forest Search (RFS) algorithm

An RFS is an ensemble learning approach which constructs a number of structured decision trees at training stage. Each tree gives a classification vote for the classes and the forest chooses the overall classification having the most votes over all the trees in the forest. The main principle behind this approach is that the group of trees (weak learner) can come together to form a Random forest (strong learner).

RFS is proposed in [110] which adds an additional layer of randomness to bagging. Random forest approach is different from standard regression and classification approaches in the way each tree is constructed using a different bootstrap sample and each node is split using the best among a subset of predictors randomly chosen at that node. The algorithm is very user-friendly in the sensing of choosing parameters. It has only two parameters: number of variables in the random subset at each node, and the number of trees in the forest.

The algorithm for the classification using RFS for C number of trees is given below.

1. For $c = 1$ to C

   a) Draw bootstrap sample of size n from the original training data (N)

   b) For each of these samples, grow a random tree T_c by recursively repeating the following steps for each terminal node of the tree, until the minimum

node size $n_{\min}$ is reached

    i. Select m features at random from the all available p features

    ii. Pick the best split point among the m

    iii. Split the node into two daughter nodes

2. Predict class by aggregating the predictions of C trees (i.e., majority votes for classification).

Suppose K is a training matrix of size n for a random tree. For the construction of each tree, m features are chosen out of p features. Random decision trees are built using this subset of original training data and randomly picked features. During testing, each vector is passed through all the random decision trees and each tree makes a decision of the class on the basis of available data and features, Finally, RFS makes an overall classification result based on the majority of votes.

3.4 Proposed Approach: Intelligent Fuzzy Inference (IFI) Algorithm

The activities to be classified are sitting, standing, going upstairs, going downstairs, walking, and jogging. The classification is very difficult because human movements are very complex. It is not easy to identify activities on the basis of only raw acceleration and angular rate features because they are not intuitive. In this section, an approach is designed based on the human movements performed by the user during these activities. Instead of computing features from the raw data and using those features to train the system, this algorithm classifies activities on the basis of GCF and knee flexion-extension angles.

3.4.1 Intelligent Fuzzy Inference (IFI) algorithm

The algorithm implemented can be divided into three important steps:
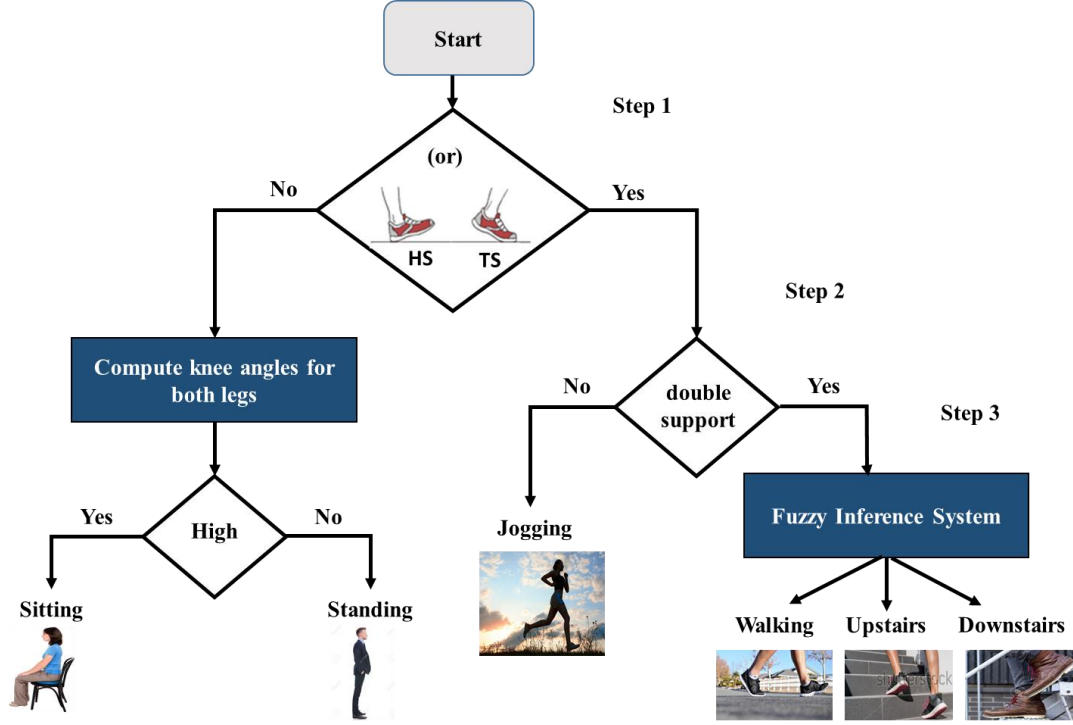
Figure 3.11: Intelligent Fuzzy Inference (IFI) algorithm flow diagram

1) Classify stationary activities like sitting and standing from non-stationary activities.

2) Classify jogging from other three walking states that includes flat ground waking, going-upstairs and going-downstairs.

3) A fuzzy Inference system classifies three walking states on the basis of knee angle during heel strike (HS) or Toe strike(TS).

In details, stationary activities like sitting and standing can be classified from other activities based on GCF information provided by smart shoes for four sensing points heel, toe, meta 1 and meta 4. In sitting and standing, no significant changes in GCF takes place over the period of time. In stationary activities, no heel strike (HS) or toe strike (TS) takes place. Based on this, stationary activities are classified from other activities. If the knee angle in the both legs are higher, the activity is sitting

otherwise standing. If HS or TS takes place: then the activity can be one of the four other activities jogging, walking, going-upstairs and going-downstairs. During jogging, at certain instant of time both feet do not touch the ground. This information gathered from smart shoes is useful in classifying jogging from other activities. Toe strike is most generally performed in downstairs activity.

For walking states, knee performs different range of flexion during HS or TS [44]. During upstairs activity, knee on the heel strike performs more knee angle compared to downstairs or walking activity. This is opposite for the downstairs activity, where knee not on the toe strike performs more knee angle. Generally, toe strike is observed in downstairs. For the walking activity, knee on the heel strike performs less angle and knee not on the heel strike performs medium knee angle. High, medium and low are relative terms and fuzzy logic is the best approach to define the thresholds for this angles. Therefore, a fuzzy inference system is designed for the classification of three walking states. The flow diagram of the IFI algorithm is given in Figure 3.11.

HS and TS detection plays a crucial role in this algorithm. To detect HS and TS, another fuzzy logic method is implemented to determine when large force is applied at heel that is proposed in [97]. Hyperbolic tangent function is used as a membership function to define smooth thresholds. TS and HS detection are used different scenarios. For instance, people generally have toe strike during downstairs.

3.4.2 Fuzzy inference system

The IFI algorithm classifies sitting, standing and jogging from three walking states in first two steps. Then, Fuzzy inference system is adopted to classify walking states.

For our classification problem, features extracted from the sensors are the inputs, with the fuzzy outputs representing each activity type. Two separate FIS systems are adopted for both left and right HS or TS events. Rule base differs for these FIS

systems. The rule bases for these FIS are discussed in further sections.

a. Membership function

In contrast to classical set theory, where data points are either 0 or 1, fuzzy logic allows membership function to range between 0 and 1. Fuzzy set theory allows partial membership function in multiple set theory. Gaussian membership function is chosen for knee angle features. Fuzzy membership function chosen by Gaussian distribution is given in the form:

$$\mu_A(x) = exp(-\frac{1}{2}(\frac{x - c_i}{\sigma_i})^2) \tag{3.35}$$
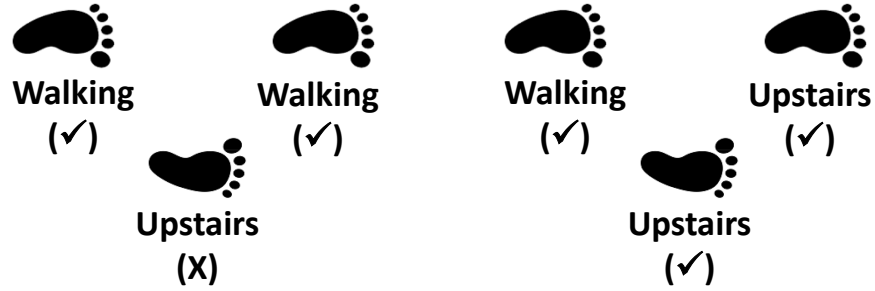
Figure 3.12: Transition detection example: a) no transition, b) transition.

where σ_i is the distribution of membership function and it is generally chosen in such a way that membership functions are overlapped and c_i is the centre of membership function and defined as:

$$c_i = \frac{x_{max} - x_{min}}{c - 1}i - 1 + x_{min} \tag{3.36}$$

where x_i is the real number in the interval (x_{min}, x_{max}). c is the number of linguistic variables. For our case, if left HS or TS takes place, two linguistic variables defined for

	Left FIS		Right FIS	
Activity	L1	R1	L1	R1
Upstairs	High	Low	Low	High
Downstairs	Low	High	High	Low
Walking	Low	Medium	Medium	Low

Table 3.3: Fuzzy rules for left and Right FIS: L1- Average Left knee angle, R1- Average Right knee angle

left leg knee angle i.e., high and low. For right knee angle, three linguistic variables are defined low, medium and high. Similarly, if right HS takes place, two linguistic variables defined for right leg knee angle i.e., high and low. For left knee angle, three linguistic variables are defined low, medium and high.

b. IF-THEN rules

The fuzzy logic and rules are used to map fuzzified inputs in to outputs. In FIS for left HS or TS event, three rules are defined. For each rule, two inputs corresponding to two features are used to map one output. This is same for right HS event.

IF A THEN B, where A and B are antecedent and consequent respectively. For instance, the rule for upstairs activity in left HS event is defined as: If (Left leg average knee angle is high) AND (Right leg average knee angle is low) THEN output is upstairs. In fuzzy logic, min is used for AND operation. The rule base is given in TABLE 1.

c. Aggregation and Defuzzification

The final step in FIS system is aggregation. It combines two outputs from fuzzy rules and form a single fuzzy set, which is then used for defuzzification method to

determine activity class. Here, max method is used for aggregation and centroid method for defuzzification. Centroid method returns centre of the area under the curve. In our algorithm results from both FIS are accounted for classifying activity.

d. Transition between the activities

It is important to detect transition between the activities along with the classification. Sit to stand or stand to sit can be easily determined on the basis of change in knee joint angle for both legs.

On the other hand, it is difficult to detect transition between non-stationary activities. In this , we employ a method in which transition between the activities can be determined accurately. Example cases for both transition and wrong detection are given in Figure3.12. If the results of the consecutive HS or TS events is different. Next HS or TS result is compared with the previous HS or TS result. If they match each other, transition takes place last HS or TS result is incorrect. This makes algorithm more intuitive in terms of detecting transitions.

3.5   Experiments and Results

In order to verify the performance of the proposed algorithm, four trails of activity experiments performed by two healthy users. In each trail, data of six physical activities sitting, standing, going upstairs, going downstairs, walking and jogging were collected for total of 6 minutes. Experiment was planned to include all the transitions between different activities. Data collected during first trail of data is used for training the system, identifying correct mean of Gaussian membership functions used for fuzzifying the inputs. Before training, the data is normalized transforming to new data vector whose norm is 1. Then, the model is tested on data collected for other three trails of the same subject (subject dependent) and different subject (subject

independent). For subject dependent tests, testing is performed on the subject by the fuzzy inference model developed using the data collected from the same subject. Where as for subject independent tests, model is developed using the data collected from another subject. Subject independent tests are useful for real life applications, because the trained model need not to be re-trained for different subjects. The main objective of the IFI algorithm is to provide higher activity recognition accuracy for both subject dependent and independent tests.

During jogging, there is an instant of time where both feet do not touch the ground, i.e., no GCF are exerted by the user on the ground. This can be inferred from the Figure 3.13, where 0.1 second time instants are marked for both the shoes. Also, the jogging GCF plot is compared with walking plot, where difference in double foot support instances can be noticed. This information is used in the algorithm to classify jogging activity from rest of the activity. For walking states, HS or TS are used to extract average knee joint angles of both legs as shown in Figure 3.14(a) and 3.14(b). These calculated average knee joint angles are used as the features for FIS. In Figure 3.14(a) and 3.14(b), clear differences in joint angles during HS for upstairs and TS for downstairs can be noticed. The knee angle is around 61 deg for upstairs and 6 deg for downstairs. A knee joint angle plot for both the legs during walking activity is shown in Figure 3.15. Here at every left heel strike, it can be seen that left knee exhibits less angle around 8 deg and right knee exhibit medium angle of 27 deg.

The performance of the algorithm can be visualized using confusion matrix. The confusion matrices for subject dependent and subject independent tests using RFS and RFI are given in TABLES II-V. It is clear that IFI algorithm performs better in both subject dependent and subject independent tests exhibiting an overall accuracy (OA) of 99.17 % and 95.52% respectively. RFS performs equally well in subject dependent tests giving OA of 97.41%. But, it exhibits lesser OA of 81.2% for subject
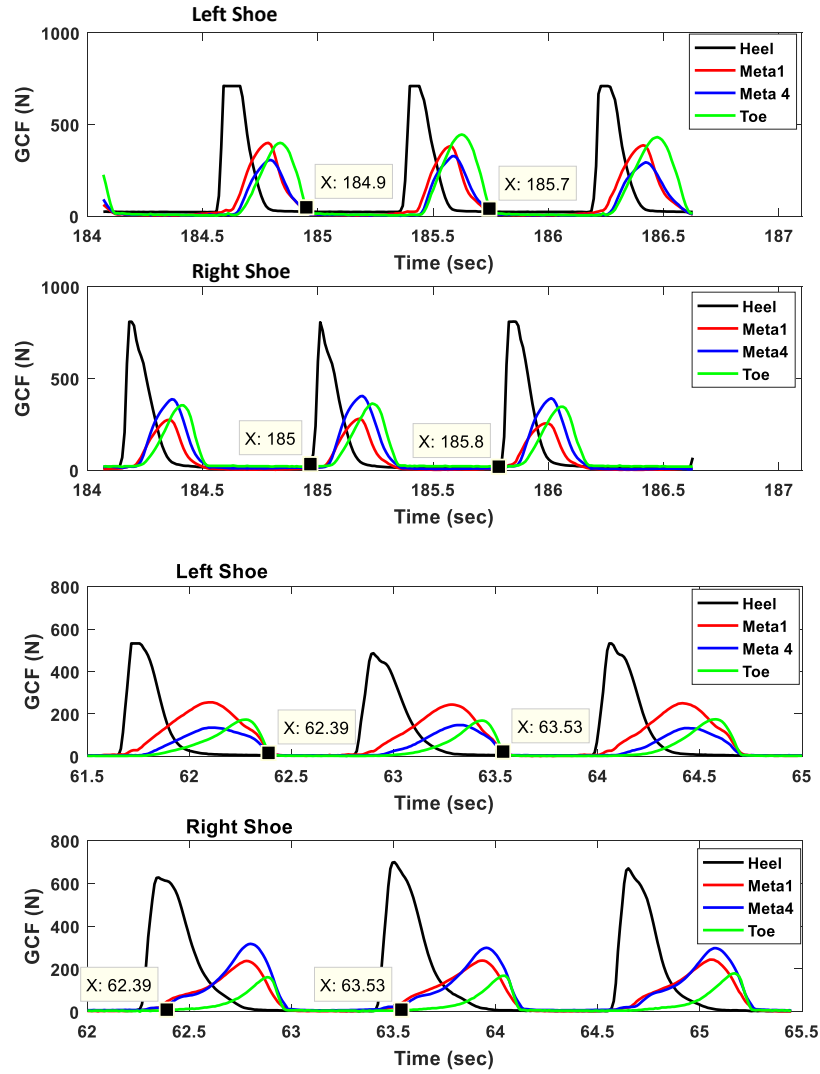
Figure 3.13: GCF plot for a) jogging showing no double support instances, b) walking showing support instances
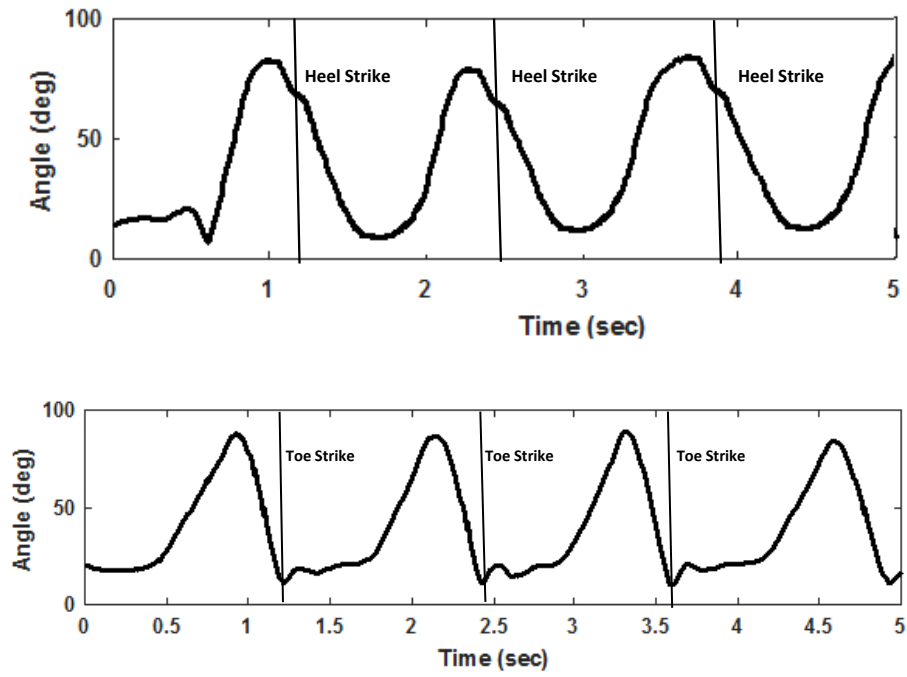
Figure 3.14: Detection periods for left leg heel strike and toe strike for a) upstairs and b) downstairs activities
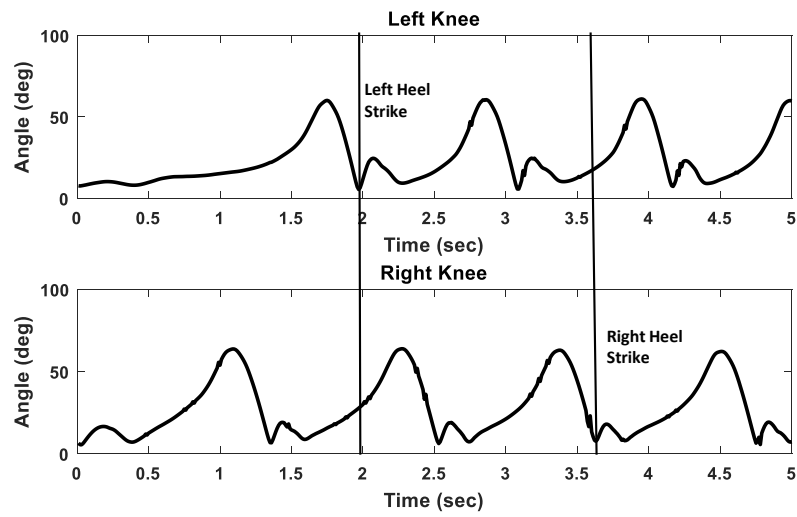
Figure 3.15: Left and right knee angles for walking

Activity	Sit	Stand	Up	Down	Walk	Jog	Accuracy(%)
Sit	603	0	0	0	0	0	100
Stand	0	605	0	0	0	0	100
Up	0	0	240	15	5	1	91.95
Down	0	0	21	201	0	3	89.93
Walk	0	0	4	1	207	0	97.64
Jog	0	0	3	4	0	249	97.27
							OA=97.41%

Table 3.4: Subject dependent confusion matrix for RFS algorithm

Activity	Sit	Stand	Up	Down	Walk	Jog	Accuracy(%)
Sit	603	0	0	0	0	0	100
Stand	0	605	0	0	0	0	100
Up	0	0	140	85	24	12	53.64
Down	0	0	97	107	7	14	47.56
Walk	0	0	68	15	129	0	60.85
Jog	0	0	57	23	5	171	66.80
							OA=81.20%

Table 3.5: Subject independent confusion matrix for RFS algorithm

independent tests compared to proposed algorithm. Most of the confusion takes place between upstairs and downstairs, where as other activities are classified with 100% precision. The OA for detecting the transitions between the six activities for subject dependent tests is 100% and 97.68% for subject independent tests. For RFS, OA for detecting the transitions between the six activities for subject dependent tests is 78% and 52.3%. It is clear that the IFI is capable of detecting transitions smoothly.

Activity	Sit	Stand	Up	Down	Walk	Jog	Accuracy(%)
Sit	618	0	0	0	0	0	100
Stand	0	625	0	0	0	0	100
Up	0	0	319	10	3	0	96.08
Down	0	0	7	317	4	0	96.65
Walk	0	0	0	0	391	0	100
Jog	0	0	0	0	0	610	100
							OA=99.17%

Table 3.6: Subject dependent confusion matrix for IFI algorithm

Activity	Sit	Stand	Up	Down	Walk	Jog	Accuracy(%)
Sit	618	0	0	0	0	0	100
Stand	0	625	0	0	0	0	100
Up	0	0	279	41	12	0	84.04
Down	0	0	32	278	18	0	84.76
Walk	0	0	0	0	391	0	100
Jog	0	0	0	0	0	610	100
							OA=95.52%

Table 3.7: Subject independent confusion matrix for IFI algorithm

The proposed algorithm gives an update about the activity at every HS or TS. For our data-sets, subjects performed HS or TS on an average 0.6 sec. On the other hand, adaptive time window segmentation approach is adopted for baseline algorithm. It generally gives update about the activity faster than fixed or sliding window. The stride frequency of the subject on an average is 1 Hz. The sampling frequency of the sensor is 100 Hz. To calculate the period of the of the activity, auto-correlation needs

to be calculated for atleast no less than periods. Therefore, update time of RFS is minimum of 2 sec. It is clear that the proposed algorithm can be useful for real-time applications, where activity needs to identified at a faster rate. The major advantage is that it will be helpful for faster transitions.

In this chapter, A design for smart shoes was reviewed. Each shoe contained four sensing units to measure GCFs at the heel, Meta1, Meta4 and toe positions. Static and dynamic calibration tests were performed on each sensing unit using Instron material testing machine. A digital filter was proposed which could compensate for the hysteresis effect in sensing unit and provide accurate GCFs estimates. The approach followed in designing this filter constituted of two parts: 1) dynamic modeling of the air bladder using standard linear solid (SLS) model, and 2) The PEM approach to identify transfer function of the compensate model. The filtered signal and raw data were compared with the data from Instron. In addition, standing and walking practical experiments were conducted on a healthy subject to verify the performance of the proposed filter.

In this chapter, classification of six human activities using HAR system consisting of four IMUs and smart shoes was proposed. This system utilized body movement accurately captured from the inertial and pressure sensors. An algorithm was implemented which could classify stationary from non-stationary activities in the first step, then jogging from three walking states. Finally, an FIS was implemented to classify the three walking states. Instead of implementing one FIS taking features from all sensors into one, two separate FISs were adopted for accuracy, reliability and faster update on the activity. The IFI algorithm detected transitions smoothly which made it reliable to implement in real time. The proposed algorithm exhibited higher overall accuracy compared to the RFS for both subject dependent and independent tests.

The algorithm developed in this chapter need measurements from a total of six

sensors (four IMUs and two smart shoes) to perform activity classification. There will always be trade-off between number of sensors and activity classification accuracy. Reducing the number of sensors may increase comfort to the users at the cost of fall in detection accuracy of activities and transitions among the activities. Therefore, the question arises is that is it possible to reduce the number of sensors and maintain considerable activities detection accuracy? In next chapter, an approach is proposed for human activity classification with a single sensor. A new two-dimensional feature space is derived from the thigh angle measurements from a IMU.

Chapter 4

A TWO-DIMENSIONAL FEATURE SPACE BASED APPROACH FOR HUMAN
LOCOMOTION RECOGNITION

There are a variety of periodic activities in human movements that includes walking, running, stair ascent and stair descent. Current state-of-the-art methods utilize multiple sensors and derive numerous features to classify periodic human activities. The derivation of numerous features for the classification poses real-time processing issues. Also, the use of multiple sensors causes discomfort to the users. This presents a real-time human locomotion recognition system using a single inertial measurement unit (IMU). The recognition method employs two novel features amplitude (A) and omega (ω) that are derived from thigh segment angular data measured using one IMU sensor. The machine learning algorithms such as linear support vector machine (SVM) and k-nearest neighbors (k-NN) are employed on the A-ω feature space to perform the classification. The periodic activities considered in this include level walking, stair ascent, stair descent, uphill, downhill, jogging and running. The experiments are performed in controlled (motion capture laboratory) and uncontrolled (outdoor) environmental conditions to evaluate the efficacy of the algorithm. The A-ω feature based method achieved significant accuracy in both environmental conditions for six subjects. The real-time classification advantages and potential benefits of this system to tune the parameters of the wearable robot are also discussed.

The contributions of this chapter can be summarized into:

- A real-time human locomotion recognition system is developed using single IMU sensor

- Two novel features A and ω are derived from thigh kinematic data which provides distinguishable feature space for classification of periodic activities.

- A transition detection module is designed that can detect the transitions between the activities in real-time.

- Both indoor (controllable environment) and outdoor (uncontrollable environment) experiments are performed to verify the efficacy of the proposed algorithm in both the environmental conditions.

The scope of this algorithm is to classify activities such as level, uphill and downhill walking, and running in the indoor environment equipped with instrumented treadmill. Also, to classify the activities such as level walking, stair ascent, stair descent and jogging in outdoors. In addition to this, transitions between all the given activities is considered in outdoors. Experimental assessments were performed on six healthy subjects who performed the activities at three different speeds. In indoor, treadmill setting is used to adjust the speed. Whereas in outdoors, metronome is used to set beats per minute and asked subjects the follow the sound beats while performing the activities.

The remainder of this chapter is organized as follows: section 4.1 gives details about the wearable sensor device and setup for the data acquisition. The algorithm for deriving A and ω features and transition detection (TD) module details are discussed in section 4.2. Experiment protocol is presented in section 4.3. The results of the experiments are given in section 4.4. Section 4.5 discusses classification accuracy of the algorithm, personalization of the system and potential benefits of the system with integration to the wearable robot.
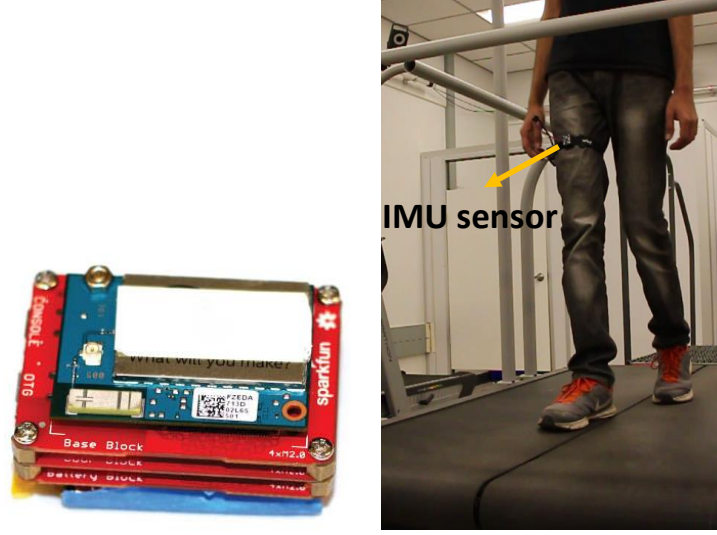
(a) IMU sensor module

(b) The subject wearing wearable sensor device

Figure 4.1: IMU sensor with Intel Edison and subject walking on the treadmill wearing wearable sensor device on his right thigh.

4.1 Human Locomotion Recognition System

The wearable sensor device consists of an inertial measurement unit (IMU) to measure thigh kinematic data in real-time. The sensor configuration, processing unit and the subject wearing the device is displayed in Figure 4.1. The Adafruit BNO055 9-DOF IMU module stacked on the Intel Edison is used for full range motion sensing shown in Figure 4.1(a). It is clear from the Figure 4.1(b) that the wearable sensor device is small in size which allows the subject to wear the device without any discomfort. The sampling rate of the IMU sensor is set to 100 Hz. The code for processing kinematic data, peak detection and the feature extraction is written in python environment. The Intel Edison is chosen due to its high processing speed and ability to handle computations in real-time.

The IMU module also provides Euler angles and quaternions. A calibration procedure is followed for the IMU sensor before placing the sensor on the subject to acquire

reliable measurements. Also, a standing calibration procedure is designed in which the subject need to stand still for 30 seconds before performing the series of activities. This is needed to identify the sagittal direction axis. Once axis is identified, the thigh angle is calculated with respect to the sagittal plane. The wearable sensor device is connected wireless to a desktop to visualize the feature space and classification results in real time. A TCP/IP protocol is setup between the device which transmits the data at 100 HZ. The wireless network configuration finds a balance between system portability and measurement delays.

4.2   Algorithm Description

The human locomotion activities such as walking, jogging, stair ascent and stair descent are periodic in nature. In literature, time-domain and frequency-domain features were computed to perform classification. Then, dimension reduction techniques were applied to reduce the number of features. Most of the work reported in periodic human activity classification were performed off-line. In this chapter, an approach is proposed to extract two features A and ω which helps in classifying periodic activities in real-time. The primary step in this approach is to identify the fundamental frequency f of the activity signal which helps to derive features A and ω.

4.2.1   Finding angular frequency ω

The fundamental frequency f can be identified using any of the three methods:

1. Compute Fast Fourier Transform (FFT) of the signal.

2. Compute autocorrelation function (ACF) of the signal.

3. Peaks search method (PSM): compute the average distance between two adjacent peaks of the signal.
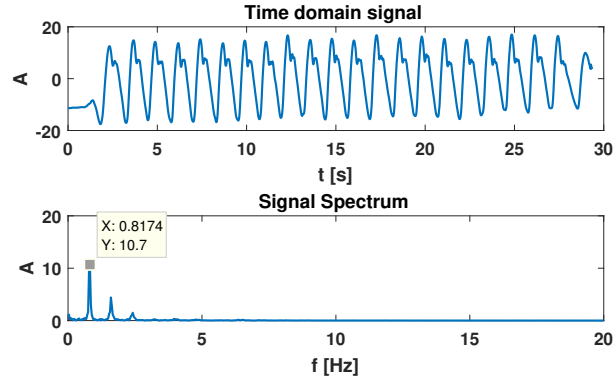
(a) The FFT spectrum of the thigh gyro signal during walking
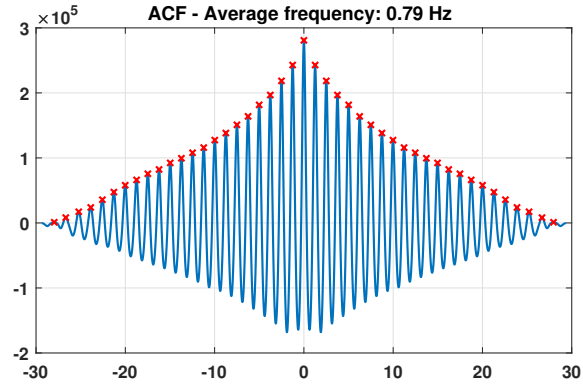
(b) The ACF plot of the thigh gyro signal during walking
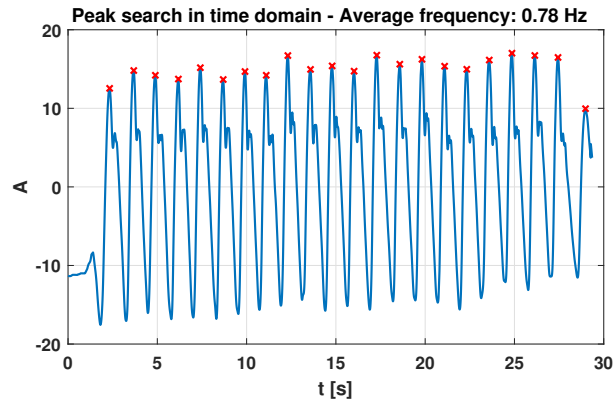
(c) The PSM result of the thigh gyro signal during walking

Figure 4.2: The comparison between three methods: FFT, ACF and PSM for thigh angular data recorded using IMU for a healthy subject. The f estimated using FFT, ACF and PSM are 0.817 Hz, 0.79 Hz and 0.78 Hz.

Among the three methods, FFT computations are expensive in real-time in comparison to the other two methods. The computation of normalized ACF requires the data of two adjacent time windows which results in the lag of f update. Considering this, PSM method is chosen in this work which is not computationally expensive and provides real-time f update. However, it is difficult to detect the peaks of the signal in presence of the noise. Therefore, there is a need for a method that can accurately detect peaks in presence of the noise. In this work, PeakUtils package from python is used for peak detection of the thigh angular data [111]. The comparison between three methods is shown in Figure 4.2. The f is calculated using three methods and it is clear that all the methods provide nearly similar result. The f calculated using FFT, ACF, and PSM methods are 0.82 Hz, 0.79 Hz, and 0.78 Hz, respectively for the thigh gyro signal during walking.

For the first peak detection in gyro signal, time window length ts and ω are not calculated as shown in Procedure 1. The time window construction starts as soon as the second peak is detected and it continues for every consecutive peak detection. The advantage of this time window is that it is adaptive in nature and changes with the pattern of the signal.

4.2.2   Finding amplitude A

As it can be seen from Figure 4.2(a) that the FFT spectrum of the gyro signal during walking resulted in three dominant peaks. This similar pattern is observed in gyro signals of the other periodic activities such as stair ascent and stair descent. The frequency associated with the highest peak is fundamental frequency f and frequencies related to other two peaks are multiples of f i.e., $f_1 = 2f$, $f_2 = 3f$. The other peaks in the spectrum are negligible. Therefore, it is possible to approximate the periodic signal related to these activities with three frequencies f, f_1, f_2 in the following form:

Procedure 1: Compute angular frequency ω

Input: Thigh angular data $g(t)$

Output: The angular frequency ω of the signal

  Start

   $[loct, pkst] = findpeaks(g(t))$ $\triangleright$ findpeaks function finds the location ($loct$)
  and values ($pkst$) of the peaks

   $j = length(loct)$

   $currentj = j,\ previousj = j - 1$

  while $currentj > 1$ **do**

   $ts = \frac{currentj - previousj}{f_s}$ $\triangleright$ f_s: sampling frequency

   $\omega = \frac{2\pi}{ts}$.

   $previousj = currentj,\ currentj = j + 1$

  end

  End

$$g(t) = A_1 e^{j\omega t} + A_2 e^{2j\omega t} + A_3 e^{3j\omega t} \tag{4.1}$$

Where $\omega = \frac{2\pi}{f}$ and $g(t)$ is the gyro signal. The derivative and double derivatives of $g(t)$ gives gyro velocity and gyro acceleration respectively. The feature ω is found using peaks search method and amplitudes A_1, A_2, A_3 can be obtained by solving the following matrix:

$$\begin{bmatrix} g(t) \\\\ \frac{\dot{g}(t)}{\omega} \\\\ \frac{\ddot{g}(t)}{\omega^2} \end{bmatrix} = \begin{bmatrix} e^{j\omega t} & e^{2j\omega t} & e^{3j\omega t} \\\\ je^{j\omega t} & 2je^{2j\omega t} & 3je^{3j\omega t} \\\\ -1e^{j\omega t} & -4e^{2j\omega t} & -9e^{3j\omega t} \end{bmatrix} \begin{bmatrix} A_1 \\\\ A_2 \\\\ A_3 \end{bmatrix} \qquad (4.2)$$

4.2.3 Algorithm summary for A-ω features extraction

1. Construction of time window: identify two consecutive peaks of gyro angle signal $g(t)$ and the distance between these two peaks is the length of the time window used for feature extraction.

2. Using two adjacent peaks, calculate f and ω.

3. Calculate gyro velocity and gyro acceleration and then compute the three amplitudes A_1, A_2, A_3 at every sample point.

4. Calculate the mean of the absolute values of the three amplitudes for all the data points in the time window.

5. The resultant amplitude A is calculated by taking the resultant of the three mean absolute amplitude values:

$$A = \sqrt{|A_{m1}|^2 + |A_{m2}|^2 + |A_{m3}|^2} \qquad (4.3)$$

where A_{m1}, A_{m2} and A_{m3} are the three mean absolute amplitude values for all the data samples in the time window.

6. Identify next peak and repeat the steps 1 to 5

Procedure 2: Compute A

Input: Thigh angular data $g(t)$, Thigh angular velocity $\dot{g}(t)$, and thigh angular acceleration $\ddot{g}(t)$.

Output: A: The amplitude of the signal

Start

$\quad [loct, pkst] = findpeaks(g(t)) \quad \triangleright$ findpeaks function finds the locations $(loct)$ and values $(pkst)$ of the peaks

$\quad j = length(loct)$

$\quad currentj = j, \ previousj = j - 1$

while $currentj > 1$ **do**

$\quad l = loct(previousj) : loct(currentj) \qquad \triangleright$ Construction of the time window

$\quad$ *Compute $A_1(l)$, $A_2(l)$, and $A_3(l)$ for given input $g(l)$, $\dot{g}(l)$, and $\ddot{g}(l)$ using matrix relation given in (7.2)*

$\quad [A_{m1}, A_{m2}, A_{m3}] = [mean(A_1(l)), mean(A_2(l))l, ...$

$\quad ... \ mean(A_3(l))]$

$\quad A = \sqrt{|A_{m1}|^2 + |A_{m2}|^2 + |A_{m3}|^2}$

$\quad previousj = currentj, \ currentj = j + 1$

end

End

For every two peaks, the angular frequency ω and resultant amplitude A are calculated. Then, these features extracted from the training data are trained with ML algorithms to build the classification models.

4.2.4 Machine Learning (ML) algorithms

After preprocessing of the raw data and extraction of features, the next step is to implement the classification algorithms. In this , two classification algorithms linear Support Vector Machine (SVM) and k-nearest neighbors (k-NN) are implemented on the A-ω features space.

Support Vector Machine (SVM)

The SVM classifier is a kernel-based classifier which classifies the data into two or more classes. During the training phase, SVM builds a model, maps the decision boundary for each class and specifies the hyperplane that separates different classes. More details about SVM is given in [112]. Basically, a kernel function is the mapping procedure performed to the training dataset to improve its resemblance to a linearly separable dataset. Some of the commonly used kernel functions are linear, RBF, quadratic, polynomial and multilayer perceptron kernel. In this work, a linear kernel is used considering computation requirements of the real-time classification. It is known that linear kernel performs well with the linearly separable dataset and takes less time to train the model in comparison to the other kernel methods. Therefore, it makes sense to use linear SVM as a classifier, if the features are linearly separable. The performance of the SVM classifier relies on the choice of the regularization parameter C which is known as the hyperplane parameter. The value of C was set to 1.

k-nearest neighbors (k-NN)

The k-NN is the instance based learning algorithm which classifies the objects based on their closest training examples in the feature space. In k-NN, an object is classified based on the majority votes of its neighbors i.e., the object is assigned to the class that is most common amongst its k nearest neighbors, where k is a positive integer [113]. In this work, (k-NN) is implemented using Euclidean distance metrics to locate the nearest neighbors [114]. The Euclidean distance $d(x, y)$ between two points x and y are calculated using the following equation:

$$d(x, y) = \sum_{i=1}^{N} \sqrt[2]{x_i^2 - y_i^2} \qquad (4.4)$$

Where N is the number of features such that $x = x_1, x_2, x_3.......x_N$ and $y = y_1, y_2, y_3.......y_N$. The number of neighbors k is used to classify the new test vector. In our case, N is 2. In this work, weighted k-NN method is used as an another classifier.

4.2.5   Transition detection between the activities

It is important to detect the transitions between the activities. In this work, a method is developed based on the location of the points in the clusters of A-ω feature map. The peaks in the thigh angle are observed during the swing phase of the gait cycle. Therefore, ML algorithms give activity classification result during the swing phase of every gait cycle.

The SVM builds hyperplanes to differentiate different classes and k-NN tries to find the classification result based on the voting result of the nearest neighbors. The transition algorithm compares every two consecutive points in the A-ω feature map. The algorithm for the transition detection is given below:

It is clear from the Procedure 3 that it needed a minimum of three consecutive peaks classification results to check the transitions between the activities. The ad-

Procedure 3: Detect transitions

Input: Feature vector $[A, \omega]$, trained SVM or k-NN model

Output: : T (T equals to 0, 1, and -100 which represent transition, no transition, and error in the transition, respectively)

Start

$\quad j = size([A, \omega])$

while $j >= 3$ **do**

$\quad prev = j - 2$, $mid = j - 1$, $next = j$

$\quad\quad\quad \triangleright$ ML(a) gives classification result using the trained model for a$^{\text{th}}$ feature point

$\quad$ **if** $ML(mid) = ML(prev)$ **then**

$\quad\quad T = 0$ $\hspace{5cm}$ $\triangleright$ No transition

$\quad$ **else**

$\quad\quad$ **if** $ML(mid) = ML(next)$ **then**

$\quad\quad\quad T = 1$ $\hspace{4.5cm}$ $\triangleright$ Transition

$\quad\quad$ **else if** $ML(prev) = ML(next)$ **then**

$\quad\quad\quad T = 0$ $\hspace{2cm}$ $\triangleright$ No transition, $ML(mid)$ classification result is wrong

$\quad\quad$ **else**

$\quad\quad\quad T = $ -100 $\hspace{1.5cm}$ $\triangleright$ Transition result runs into error, detection result is not given at this point

$\quad\quad$ **end**

$\quad$ **end**

end

End

vantage of this algorithm is that along with transition detection, it also identifies false detection of the classification. As shown in the condition of Procedure 3 that if there is a change in classification result between two consecutive points, next point classification result is checked to make sure that the transition really took place. Otherwise, previous point classification result is considered as false detection.

4.3 Experiment Protocol

To assess the real-time classification performance of the proposed approach, the wearable sensor device was tested on six healthy subjects (five men and one woman). Two types of environmental conditions were chosen for the experiments: Controlled (indoor labs) and uncontrolled (outdoors). The age, height, and weight of the subject is shown in Table 4.1. We have the application approved by Arizona State University (ASU) Institutional Review Board (IRB) regarding human subjects experiments. In the controlled environment, the subject was made to do the activity on the instrumented treadmill which has an option to control the speed of the treadmill. In the uncontrolled environment, the subject had the flexibility to complete the activities at his or her own pace in outdoors. However, in some experiments metronome was used to specify the steps rate to the subject. These experiments were designed to perform analysis on the A-ω feature map for same activity with different step rates. For this, the subject was asked to synchronize the steps with the beats sound from metronome. The activities chosen for the controlled environment were level walking, uphill, downhill and running. Three different speeds: slow, medium and fast were set on the treadmill. The speeds set for the three walk states level walking, uphill, and downhill were 0.4 m/s, 0.6 m/s, and 0.8 m/s. For Running, the speeds were 1.4 m/s, 1.7 m/s, and 2 m/s. The time duration of each experiment on the treadmill is one minute each. The slope of the treadmill was set to 0, 0, +10 and -10 degree for level

walking, running, uphill, and downhill. In uncontrolled environment, the subject is made to perform level walking, upstairs, downstairs and jogging. Also, the transitions between the activities were included in uncontrolled environment experiments to test the efficacy of the transition module of the algorithm.

For experiments, the subject was asked to performed three trials of each activity experiment. In this, two trials experimental data was used for training the ML algorithms. Then, the trained ML algorithm is tested on the subject in real-time for the third trial. The metric used for analysis is the total classification accuracy % which is the percentage of correctly classified activities divided by a number of incorrect classifications. This metric was computed in real time and given after the end of the trial.

4.4   Results

The proposed approach in this focuses on subject specific training and testing of the classification algorithm. Therefore, every subject performed three trials of experiments for each activity. The data of first two trials were used to extract A-ω

Subject Id	Age(Y)	Gender	Height (ft)	Weight (lb)
1	30	Male	6	170
2	24	Male	5 11'	l51
3	27	Female	5 4'	115
4	30	Male	5 4'	159
5	25	Male	5 10'	143.3
6	26	Male	6	223

Table 4.1: The details of the subjects participated in the experiment
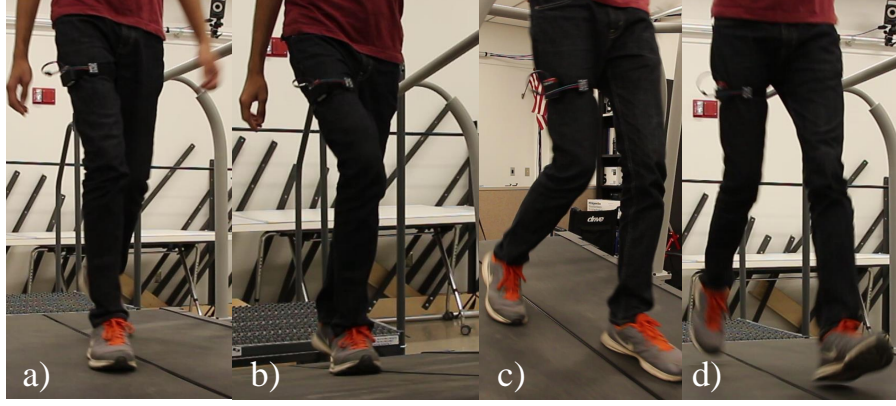
(a) The setup for experiments in indoor laboratory: a) level walking at 0 degree slope , b) uphill at +10 degree slope, c) downhill at -10 degree slope, and d) running at 0 degree slope.

(b) The setup for experiments in outdoors: a) level walking, b) upstairs, c) downstairs, and d)jogging.

Figure 4.3: The experiment setup for all the activities of a healthy subject in both environmental conditions

features and ML algorithms: SVM and k-NN were trained on these features. Then, the trained models were tested for the third trial to verify the classification accuracy.

The A-ω feature map for the test trial on a healthy subject in the controlled environment for slow, medium and fast speeds is shown in Figure 4.4. It is clear from the Figure 4.4 that the features in the map are clearly distinguishable for four activ-
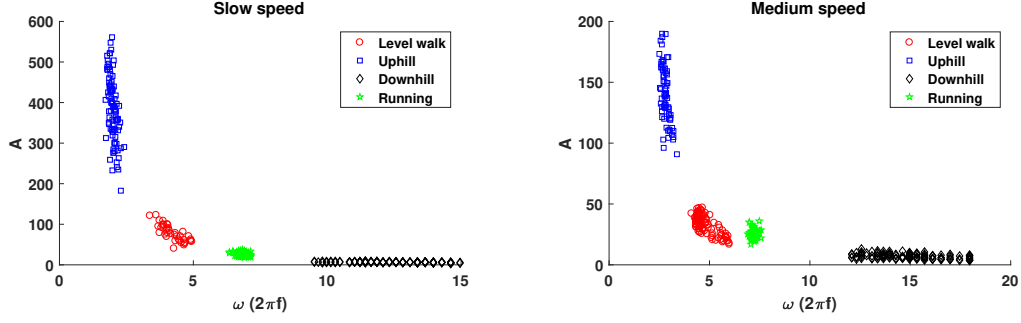
(a) A-ω feature map for slow speeds in the con- (b) A-ω feature map for medium speeds in the

trolled environment   controlled environment
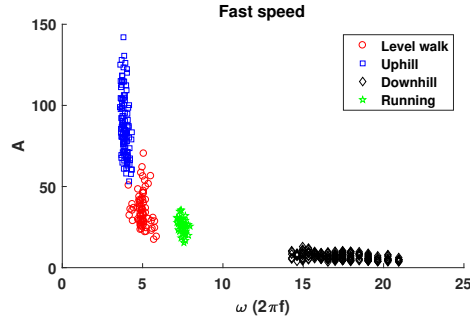
(c) A-ω feature map for fast speeds in the con-

trolled environment

Figure 4.4: A-ω feature map for three different speeds in the controlled environment for a healthy subject in a test trial. The speed setting for level walking, uphill, and downhill was 0.4 m/s, 0.6, and 0.8 m/s, respectively. For running, it was 1.4 m/s, 1.7 m/s, and 2 m/s, respectively.
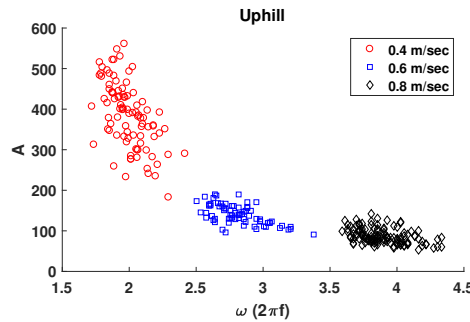
Figure 4.5: The A-ω feature map for uphill activity at three speeds 0.4 m/s, 0.6 m/s, and 0.8 m/s, respectively for a healthy subject in a test trial. It is observed here that as speed increases the ω increases and A decreases.
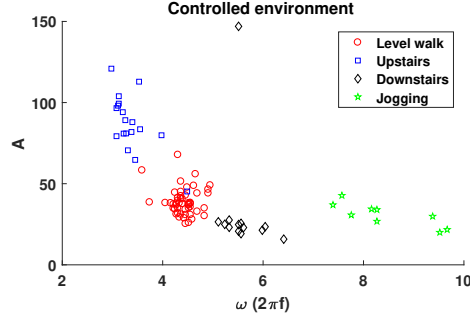
Figure 4.6: The A-ω feature map for locomotion activities for a healthy subject in the uncontrolled environment. Here, the test subjects performs activities at flexible speed in out doors.

ities: level walking, uphill, downhill and running for all the speeds. The amplitude is higher in uphill in comparison with the other activities. Whereas, downhill exhibited less amplitude. It is also observable that the deviation of feature points is more in uphill and downhill when compared to walking and running. A clear distinction in the features is also observable in the same activity such as uphill at different speeds shown in the Figure 4.5. Therefore, it is possible to make a point here that the same activity at different speeds is also differentiable using A-ω features. The feature map for a test trial on a healthy subject in the uncontrolled (outdoor) environment is shown in Figure 4.6. In this trial, the subject performed the activities with flexibility at his or her own pace. The features here in the uncontrolled environment are more spread than the features in the controlled environment for four activities that can be inferred from Figure 4.4 and 4.6. The feature map for a healthy subject at three different step rates for level walking, uphill, and downhill is shown in the Figure 4.7. It is observable that A-ω feature space provides considerable distinction among the same activity at different step rate shown in Figure 4.7.

The controlled environment classification results for slow, medium and fast speeds are presented in terms of the confusion matrices displayed in the Tables 4.2 to 4.4. The subject-specific classification accuracy results for each subject is reported in the
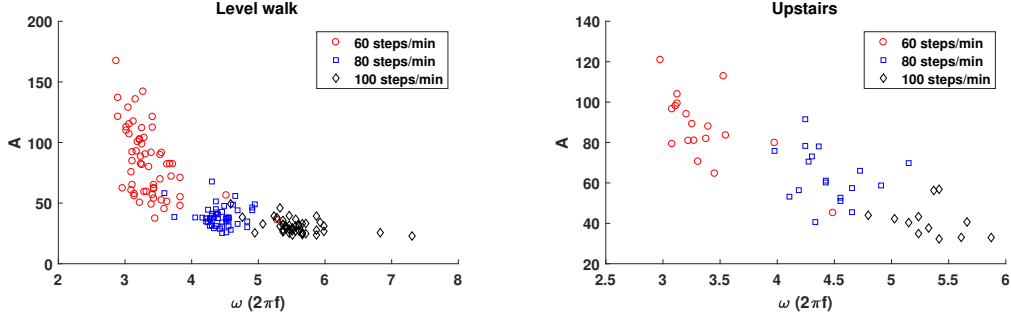
(a) A-ω feature map for level walk activity in uncontrolled environment

(b) A-ω feature map for upstairs activity in uncontrolled environment
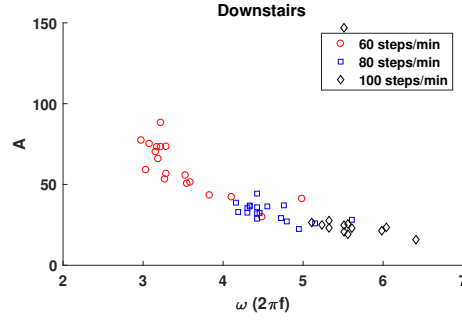
(c) A-ω feature map for downstairs activity in

uncontrolled environment

Figure 4.7: A-ω feature map for three walk states at different step rate in the uncontrolled environment for a healthy subject in a test trial. The step rates considered in this experiment were 60, 80, and 100 steps/min, respectively.

form of bar charts shown in the Figure 4.8. It can be seen from Figure 4.9 and Table 4.5 that the classification accuracies are comparatively less for uncontrolled environment experiments. The transitions are detected with 100% accuracy for all the outdoor experiments.

4.5 Discussion

4.5.1 Classification accuracy

It is clear from Figure 4.8 and 4.9 that the classification accuracy in the uncontrolled environment is comparatively lower than the controlled environment. The

possible reason is that the subject takes flexibility to walk at his/her comfortable speed and may not be uniform in terms of spatial or temporal gait parameters such as stride length or cadence in the outdoors. However, the A-ω feature space still can be able to differentiate the activities. Also, the deviation of the feature points in the map gives inference about the uniformity in the strides. Comparing the feature map of the two environment results, it is clear that feature points in the controlled environment for a corresponding activity are less deviated than the uncontrolled environment which shows that the subject performs more uniform strides in the controlled environment. It should also be noted that this deviation does not affect the feature distinction between the activities. Therefore, ML algorithms SVM and k-NN exhibited good performance in terms of classification using extracted features in both environmental conditions. The A - ω feature map also differentiates the same activity at different speeds in both environmental conditions. It can be seen from the Figure 4.5 that A decreases and ω increases with the increase in the speed of the treadmill that helps to differentiate different speeds of the same activity. This trend is also observed in the feature maps of the activities performed in uncontrolled environment

Activity	Walk	Uphill	Downhill	Running	Accuracy (%)
Walk	173|172	1|2	0|0	1|1	98.8|98.2
Uphill	0|1	158|157	0|0	0|0	100|99.4
Downhill	0|0	0|1	164|163	0|0	100|99.4
Running	8|7	6|6	0|0	254|255	94.8|95.5
					OA = 97.9|97.6

Table 4.2: The slow walk experiment results in controlled environment for both SVM and k-NN represented in the form of confusion matrix. The element in the matrix represent SVM\|k-NN result

at different step rates shown in Figure 4.7. It can be inferred from the confusion matrices shown in Tables 4.2, 4.3 and 4.4 that uphill and downhill activities gets less confused with the other activities. Whereas, level walking and running confuses more. Both SVM and k-NN exhibited high accuracy in slow, medium and fast speed experiments. It can be inferred form the Figure 4.8 that SVM and k-NN exhibited a higher accuracy of 100% , 100% and lower accuracy of 95.6%, 95.3% respectively for slow speed experiments in subjects with ID 1 and 2. For medium speed experiments, it is 100%, 100% and 96%, 96% respectively for SVM and k-NN in the same subjects. The SVM and k-NN exhibited a high percentage of 99.8% and 98.8% and a low percentage of 96% and 95.4% in subjects with Id 1 and 5 for fast speed experiments. In the uncontrolled environment, running activity classification is 100%. The walk states level walking, upstairs and downstairs confuses a lot that can be seen from Table 4.5. From the bar chart shown in the Figure 4.9, it can be seen that SVM exhibited a higher and lower classification accuracy of 97.3% and 88.5% in subjects with Id 2 and 5. Whereas, k-NN exhibited 96.5% and 87% for the same subjects.

Activity	Walk	Uphill	Downhill	Running	Accuracy (%)
Walk	211|208	1|2	2|2	1|3	98.1|96.7
Uphill	0|0	197|197	0|0	0|0	100|100
Downhill	4|1	0|0	210|213	0|0	98.1|99.5
Running	8|11	0|0	1|0	278|276	96.9|96.2
					OA = 98.1|97.8

Table 4.3: The Medium walk experiment results in controlled environment for both SVM and k-NN represented in the form of confusion matrix. The element in the matrix represent SVM|k-NN result

79

4.5.2 Personalized device

The wearable sensor device that is developed in this can be considered a personalized device. The training data given to the algorithm is taken from subject's activity itself. The activity profile changes from subject to subject. For example, gait pattern is not similar and the thigh movement during the locomotion activity can differ from subject to subject. Therefore, it becomes difficult to build a system that is general for all. However, a personalized system with less training data to train the model serves as an alternative solution to this specific problem. Therefore, in this , one such system is proposed which needs 1 to 2 minutes of data of each activity to train the algorithm and be able to provide real-time detection of the activities. Also, the A-ω feature map provides insight into the patterns of the activities performed by a specific subject. The stride to stride comparison is possible through these features. For instance, more deviation in the feature space of one activity gives information that the activity is not performed uniformly. This system is useful in medical as well as sports training, where physiotherapist needs to check the improvement in the subject and athletes needs to improve their performance on a regular basis. Also, these features

Activity	Walk	Uphill	Downhill	Running	Accuracy (%)
Walk	275|273	4|5	0|0	3|4	97.5|96.8
Uphill	0|0	261|261	0|0	0|0	100|100
Downhill	0|0	0|1	275|273	0|1	100|99.3
Running	5|5	2|2	4|5	324|323	96.7|96.4
					OA = 98.4|98

Table 4.4: The Fast walk experiment results in controlled environment for both SVM and k-NN represented in the form of confusion matrix. The element in the matrix represent SVM\|k-NN result

give distinction between all the periodic activities that helps in rehabilitation training of the patients while performing different activities.

4.5.3 Integration to wearable assistive robot

The wearable sensor device can be easily be integrated to any assistive robot that needs to provide assistance during various activities. The adaptive phase oscillators algorithms were proposed for the exoskeleton to assist periodic activities in the literature which needs learning of the signal's parameters [96, 115, 116]. During the transition from one periodic activity to another, it becomes difficult for the adaptive oscillators architecture to learn the parameters of the new signal in a short period. Therefore, the approach proposed in this will be useful in providing frequency and amplitude parameters that are needed for the new signal. However, the current approach needs improvement to account for the new features to provide parameters for the signal. Now, the algorithm detects the periodic activities in real-time. The addition of a prediction module to the current algorithm that can predict the probability of next feature point belonging to a specific activity is needed. For instance, after

Activity	Walk	Uphill	Downhill	Jogging	Accuracy (%)
Walk	108|104	8|10	4|6	0|0	90|86.7
Uphill	14|10	106|110	0|0	0|0	88.3|91.7
Downhill	8|9	0|0	112|111	0|1	93.3|92.5
Jogging	0|0	0|0	0|0	120|120	100|100
					OA = 93|92.3

Table 4.5: The activity results in uncontrolled environment for both SVM and k-NN represented in the form of confusion matrix. The element in the matrix represent SVM$|k$-NN result
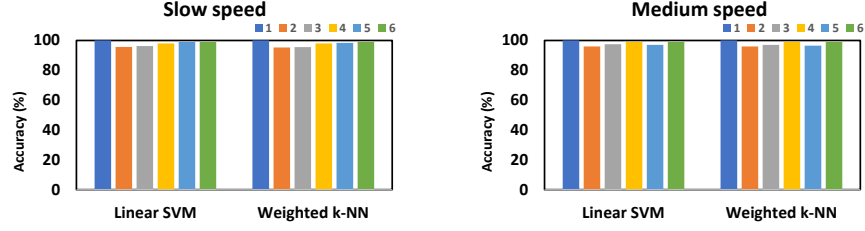
(a) Classification accuracy% for 6 sub-
jects in the controlled environment at
slow speeds

(b) Classification accuracy% for 6 sub-
jects in the controlled environment at
medium speeds
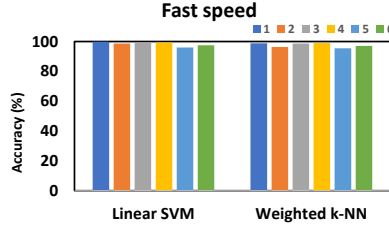
(c) Classification accuracy% for 6 sub-
jects in the controlled environment at
fast speeds

Figure 4.8: Classification accuracies for controlled environment at different speeds
for linear SVM and k-NN
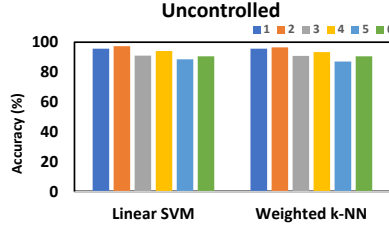
Figure 4.9: Classification accuracy % for 6 subjects in the uncontrolled environment
for linear SVM and weighted k-NN.

detection of two peaks in the thigh angular data, it needs to give current activity
state and also predict the next probable state. This prediction module will be helpful
in tuning the adaptive oscillator parameters and also impedance parameters if the
robot is designed to tune the impedance parameters based on various activities.

In this chapter, an approach for real-time periodic activities classification is pro-

posed which works on 2 dimensional feature space A-ω. The features are extracted from a single IMU attached to the thigh segment of the user. The algorithm is tested in two types of environment: controlled (indoor labs)and uncontrolled (outdoors). The activities considered in this are level walking, uphill, downhill and running on instrumented treadmill, and level walking, upstairs, downstairs and jogging in outdoors. The SVM and k-NN exhibited higher activities classification accuracies in both controlled and uncontrolled environmental conditions. The next step will be the integration of this human locomotion recognition system with the hip exoskeleton that is developed to assist the soldiers in outdoor activities such as level walking, uphill and downhill [117] that is given in chapter 7. Implement the prediction module in addition to this activity detection module that will help to tune the parameters for the adaptive oscillator that will be used in the hip exoskeleton.

Chapter 5

AUTOMATIC VIRTUAL IMPEDANCE ADAPTATION OF A KNEE EXOSKELETON FOR PERSONALIZED WALKING ASSISTANCE

This chapter attempts to address the problem of online tuning of virtual impedance for an assistive robot based on real-time gait measurement data to personalize the assistance for different users. In this work, smart shoes and inertial sensors are employed to measure the ground contact forces and knee joint kinematics, respectively. An automatic impedance tuning (AIT) approach is presented for a knee-joint exoskeleton based on real-time activity recognition and gait phase detection. Human knee joint impedance is identified with the walking data collected on two healthy participants. A Gaussian mixture model (GMM) is employed to map the fuzzy likelihood of various activities and gait phases to the desired robot virtual impedance. Experiments are conducted on these two participants to evaluate the benefit of the proposed algorithm by comparing muscle activities and gait metrics. The results demonstrate that the robot assistive torque is smoother and EMG signal of Vastus Medialis is reduced, compared to constant impedance and finite state machine approaches. It is also noticed that the AIT reduces knee range of motion and step length but increases walking cadence.

This work serves as our first step to tackle the personalization issue of assistive robots from the robot planning and control perspective. We develop an online impedance tuning approach to adaptively control wearable assistive robots. Smart shoes and inertial sensors are employed to collect GCF and kinematic data. Activity recognition and gait phase detection algorithms are developed to understand human walking in real time. Instead of having a deterministic answer on the current activ-

ity and gait phase, a likelihood value is introduced to account for uncertainties and fuzziness. A Gaussian mixture model (GMM) is trained to map the fuzzy likelihood of activities and gait phases to the desired virtual impedance of the robot, based on the identified user knee impedance for different activities and gait phases. The contributions of this chapter include: 1) an *online activity and gait phase detection* approach is developed based on force and kinematic data, 2) an *automatic online impedance tuning* approach is developed based on human knee characterization and GMM to allow smooth transitions and personalize the assistance, and 3) the efficacy of these algorithms is verified by experiments with two human participants and its potential benefit is illustrated using gait and EMG metrics.

The remainder of this chapter is organized as follows: Section 5.1 reviews the related literature for impedance based control strategies. Section 5.2 discusses the mechatronic design of the wearable sensors and assistive robot. In section 5.3, the human knee impedance is studied. Section 5.4 introduces the activity and gait phase detection algorithms. The online impedance tuning algorithm is discussed in section 5.5. Experimental results with two participants are presented in section 5.6.

5.1   Related Work

The proper assistance of wearable robots significantly depend on planning and control. For motion planning of the wearable robots, impedance control has been the most popular approach due to its simple implementation and clear physical intuition [118]. Over the years, the finite state machine (FSM) is a widely adopted strategy to modulate the impedance parameters in the robot controller based on gait phases and activities. To implement FSM, it becomes important to integrate the real-time gait and activity detection algorithms into the high-level control of the assistive robot. Hybrid Assistive Limb (HAL3) is a famous lower-extremity wearable robot. It broadly

classified one walking cycle into support and swing phases based on force resistive sensor threshold, and constant torque is applied to hip and knee joints [119]. Apart from HAL, other companies such as ReWalk [120] and Ekso Bionics [121] built hip-knee exoskeletons and employed FSM controller strategy to assist individuals with SCI. In [122], a FSM based controller is designed for five gait phases to allow variation in impedance for the knee joint. The gait phases are detected based on knee angles and manually defined thresholds of GCFs. A FSM controller is implemented in [123], in which the stiffness of the knee actuator is modulated based on stance and swing phases of the gait cycle. In MINDWALKER exoskeleton, a FSM based impedance controller is designed for nine states in a gait cycle [76]. A FSM based impedance controller is implemented for modulating impedance parameters in the robotic device with knee and ankle actuators for sitting, standing and walking activities in [46], and for stair ascent and descent in [124]. Although FSM has shown promising results, there still remains a major limitation, as it leads to discrete jumps in the impedance parameters during state transitions [76, 125].

In the aforementioned work, the impedance parameters are manually set for different gait phases or activities which requires a lot of time and experience from medical professionals. Moreover, these parameters may differ across users. Therefore, it is not possible to design generalized impedance parameters profile across the users, instead, they need to be personalized based on user's requirements. To address these issues, researchers started focusing on the human joint impedance studies to get more insight on the joint impedance modulation, and to design the assistive robots that mimic the physiological joint behavior [126]. The conventional methods to determine joint impedance involve perturbing the joint in a controlled manner, and describing impedance as the dynamic relationship between applied perturbations and corresponding joint torques [127]. Some developed methods to estimate the elastic

components of the knee joint impedance that depends on muscle activation [128]. Others modeled the knee joint as a spring-damper system and identified knee stiffness, damping and setpoint for gait phases [129]. The results from the aforementioned human studies demonstrated that the human modulates the impedance parameters in a smooth and continuous manner within a gait cycle and these impedance parameters profile changes from subject to subject. Despite ongoing research on human joint impedance studies, there still exists a gap in embedding those insights into impedance-based controller strategy for robots.

Inspired by the aforementioned limitations of the existing work, the main focus of this is to provide smooth impedance modulation for the robotic assistive device to assist the user in a personalized manner. This is approached by imparting the identified impedance parameters in human study experiments to the robot controller. An automatic impedance tuning (AIT) algorithm is proposed which automatically modulates the impedance parameters for gait phases and activities. Smart shoes and inertial sensors are introduced to collect GCF and kinematic data. Activity recognition and gait phase detection algorithms are developed to understand human walking in real time. These algorithms provide fuzzified values instead of deterministic decisions. These fuzzy likelihood values provide flexibility for smoothing the impedance parameters profile. A Gaussian mixture model (GMM) is trained to map the fuzzy likelihood of activities and gait phases to the desired virtual impedance of the robot, based on the identified user knee impedance for different activities and gait phases. The scope of this is to provide assistance during stance and implement zero impedance case to allow user free motion during swing.

5.2 Mechatronic Design

5.2.1 Wearable sensing system

The wireless wearable sensing system comprises inertial measurement units (IMUs) and smart shoes to measure knee joint angles and GCFs. The system is connected to a high-performance computer through a stable wireless ad-hoc network using the TCP/IP protocol. The smart shoes are developed to measure GCFs at four points: heel, first metatarsal joint (Meta 1), fourth metatarsal joint (Meta 4) and toe while the silicone tubes are wound into air bladders and connected to barometric pressure sensors shown in Fig.5.1(a) and (b). The sampling rate of the smart shoes is set to 100 Hz and a model-based filter is implemented to compensate for hysteresis and estimate GCFs from pressure sensor readings in real time [130].

Four IMUs are placed on bilateral thighs and shanks to measure acceleration and angular rate in real time. The placement of IMUs on the participant is shown in Fig.5.1. The combined Bosch Sensortec's BNO055 IMU and an Intel Edison processor is used for motion sensing, as shown in Fig.5.1(d). The sampling rate of all IMUs is set to 100 Hz. The knee angle is estimated by initially aligning the sensor frames of thigh and shank using functional alignment procedure and then calculating the relative orientation using an extended Kalman filter [106].

5.2.2 Knee assistive device (KAD)

A knee assistive device (KAD) is an exoskeleton with a compact rotary series elastic actuator (cRSEA) [131]. In a cRSEA, a worm gear and spur gear combination is used to amplify and change the direction of assistive torque generated by a DC motor. The mechanical design of KAD is shown in Fig.5.1(c). The cRSEA is compact and light with a weight of 1.57 kg to avoid unbalance and discomfort to users. The
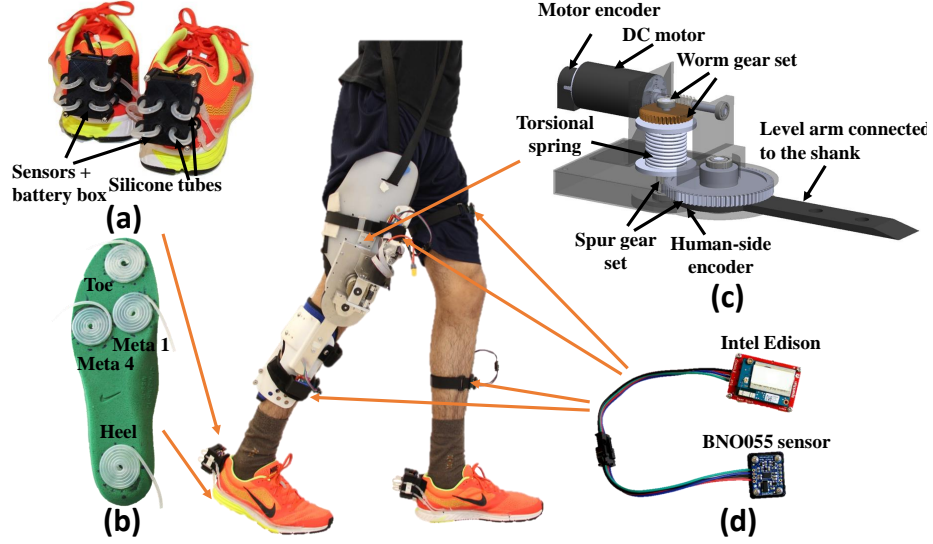
Figure 5.1: Wearable sensing system and knee assistive device

maximum power consumed by the knee joint is about 80W for a male subject with the body weight of 70 kg and during level walking and the knee angular velocity ranges between ±60 rpm [131]. Considering this, Maxon RE40, a 150W DC Motor is used to power the KAD. With a combined gear set reduction ratio of 63.6:1, the end

Component	Specification	Value
Torsion spring	Spring constant	6.59 N·mm/deg
	Max angular deflection	317 degrees
Worm gear	Gear ratio	10:1
	Pressure angle	25 degrees
	Lead angle	18.26 degrees
Spur gear	Gear ratio	6.36:1
	Pressure angle	14.5 degrees
Encoders	Resolution	2000 counts/turn

Table 5.1: Design Specification of KAD Components

89
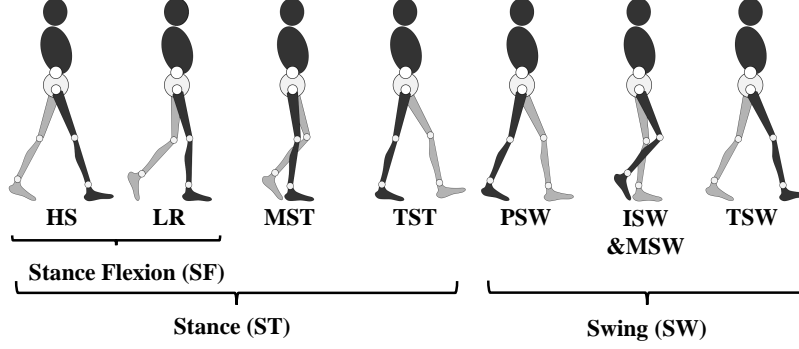
Figure 5.2: The gait cycle of human walking. HS - heel strike, LR - loading response, MST - mid stance, TST - terminal stance, PSW - pre-swing, ISW - initial swing, MSW - mid swing, and TSW - terminal swing.

effector can reach a maximum angular velocity of 120 rpm and the KAD can provide a maximum continuous assistive torque of 11.26 N·m. Two incremental optical rotary encoders (US Digital) are used to measure both motor and human knee angles, which are re-initialized at the beginning of each experiment. The torsion spring serves as a torque sensor and also provides an energy buffer to prevent injuries from unexpected high motor torques. The specifications of the components used in the KAD are given in Table 5.1. The design of KAD targets people with unilateral impairment which affects knee function. In this , the KAD is used to assist right side knee.

5.3   The Study of Human Knee Motion

The scope of this chapter is to provide knee assistance during stance phase by tuning the impedance parameters of the assistive robot. It is important to understand the impedance modulation performed by the human as it is necessary for stable and efficient gait cycle. In a gait cycle, human continuously modulates their joint impedance depending on the activity, speed and terrain. The understanding of human knee impedance is critical for proper virtual impedance of the assistive robot, as shown in Section 5.5.1.

The experiments were set up in the motion capture laboratory which was equipped

90
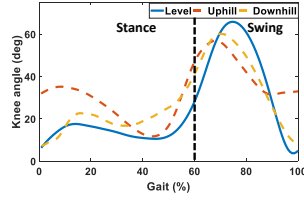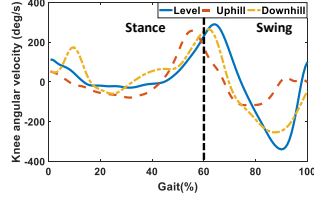
(a) Knee angle

(b) Knee angular velocity
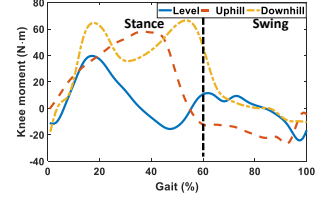
(c) Knee moment
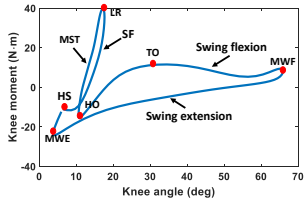
(d) Level walking: moment v.s angle
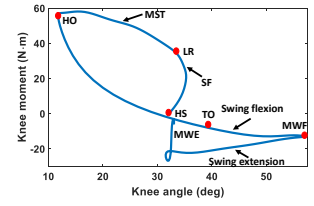
(e) Uphill: moment v.s angle
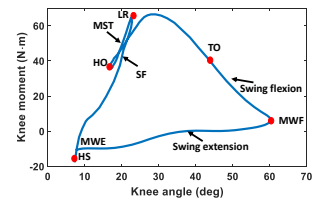
(f) Downhill: moment v.s angle
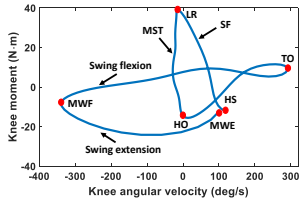
(g) Level: moment v.s angular velocity
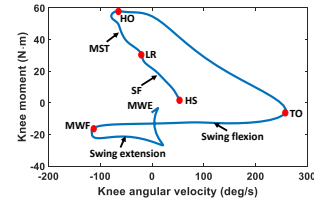
(h) Uphill: moment v.s angular velocity
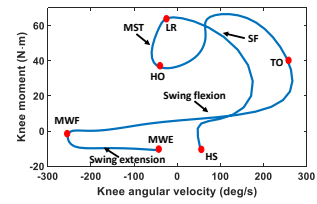
(i) Downhill: moment v.s angular velocity

Figure 5.3: The comparison of knee kinematics and kinetics for three activities experiments performed on a healthy participant. The slope of the treadmill was set to 0, +10, and -10 degree and the speed of the treadmill was 0.8 m/s, 0.6 m/s, and 0.6 m/s for level, uphill, and downhill walking experiments.

with 12 high-speed infrared cameras (Vicon Motion Systems Ltd.,) and instrumented treadmill (Bertec Corporation) at Arizona State University (ASU). Two healthy participants with height and weight 180 cm, 183 cm and 59.96 kg, 77.61 kg, were chosen to participate in the experiments. The activity experiments level, uphill, and downhill walking at 0, +10, and -10 degree slope were planned. The speed of the treadmill was set to 0.8 m/s for the level walking and 0.6 m/s for both uphill and downhill based on the comfort level of the participants. There is a limitation related to the instrumented treadmill that it does not allow changing the slope of the contact surface while running. Therefore, the experiments of three activities were planned separately without focusing on their transitions. There are two objectives associated with performing experiments: 1) to get the kinematics and kinetics data of the knee to study human impedance modulation and also to identify the parameters of the model that will be discussed in section 5.3.1. 2) To get the experimental data to train GMM in AIT algorithm that will be proposed in section 5.5.1. For the experiments, participant worn markers, IMUs, and smart shoes. The knee angle and GCFs data from IMUs and smart shoes will be used as the inputs to activity recognition and gait phase detection modules which is detailed in Sections 5.4.1 and 5.4.2. The ASU Institutional Review Board (IRB) reviewed and approved the studies in this .

5.3.1   Human knee impedance model

This primarily focuses on identifying the knee stiffness and damping during the stance phase of the level, uphill, and downhill walking. In this , a spring damper model is considered for modeling the human knee torque with respect to the knee angle and angular velocity [129]. The kinematics and kinetics data are processed for the right knee as our KAD is designed for right side. The spring damper model is defined as [129]:

Gait phases	Parameters	Activities		
		Level	Uphill	Downhill
Stance flexion	k_{SF}	1.796	3.203	4.418
	b_{SF}	0.011	-0.314	-0.052
	θ_{SF}	12.56	36.46	8.790
Mid stance	k_{MST}	5.716	2.115	5.335
	b_{MST}	-0.293	-0.106	0.064
	θ_{MST}	10.74	37.17	10.13
Terminal stance	k_{TST}	0.426	5.377	3.304
	b_{TST}	-0.462	-0.487	-0.081
	θ_{TST}	0.012	26.37	4.350

Table 5.2: The identified mean stiffness k (N·m/degree), mean damping b (N·m·s/degree) and mean set point θ_0 (degree) for 45 gait cycles of participant 1.

$$T_h(t) = k(\theta_h(t) - \theta_0) + b\dot{\theta}_h(t), \tag{5.1}$$

where $T_h(t)$, $\theta_h(t)$ and $\dot{\theta}_h(t)$ are the human knee moment, angle, and angular velocity, respectively. k, b, and θ_0, represent the knee stiffness, damping, and setpoint, respectively. A gait cycle can be divided into two main phases: stance (ST) and swing (SW). The ST can be further divided into three subphases: stance flexion (SF), mid stance (MST) and terminal stance (TST), as shown in Figure 5.2. The SF phase includes the heel strike (HS) and loading response (LR). In this , k, b and θ_0 are identified for three phases SF, MST, and TST using a least square method with $T_h(t)$ as output and $\theta_h(t)$, $\dot{\theta}_h(t)$ as inputs. The identified k, b and θ_0 for participant 1 are given in Table 5.2.

The knee angle, angular velocity, and moment for the activities for a healthy participant are shown in Figures 5.3(a) to 5.3(c). The knee moment versus angle and knee moment versus angular velocity during one gait cycle for different activities are shown in Figures 5.3(d) to 5.3(i), and it can be seen that the SF takes place from HS to LR. Whereas, MST is from LR to heel off (HO) and the TST is up to toe off (TO). The swing knee flexion is observed from TO to maximum swing flexion (MWF) and swing knee extension takes place up to the next HS. The knee flexion during HS is higher for uphill in comparison with the level or downhill walking which can be seen in Figure 5.3(a). The knee plays a wide range of roles during the execution of the gait, including supporting the body weight and deceleration during stance by applying a large knee moment. The knee undergoes a resistive flexion during SF and a propulsion extension during MST. On the other hand, knee undergoes a ballistic movement demanding a less significant effort during swing phase. This trend is observed in knee moment plots shown in Figure 5.3(c).

The knee stiffness follows a more linear profile in the stance compared to swing in three activities shown in Figures 5.3(d) to 5.3(f). It can be seen from Table 5.2 that maximum stiffness for level and downhill walking is observed during MST phase, but for uphill it is observed during terminal stance, which is also shown in the knee angle-moment plots Figures 5.3(d) to 5.3(f). This can be justified from the biomechanical perspective that the moment where the body begins to transit from force absorption at impact to force propulsion happens during MST in level, and downhill walking. Whereas, this transition happens during TST in uphill walking [132]. The knee damping values for the stance phases in three activities are also shown in Table 5.2. The knee damping values for downhill during MST and TST are
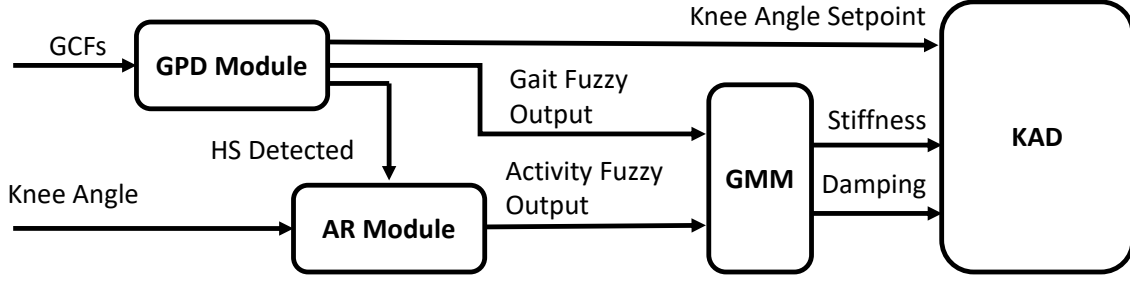
Figure 5.4: The overview of AIT algorithm structure.

relatively high compared to level and uphill walking. This can also be inferred from the knee angular velocity and moment plots shown in Figures 5.3(g) to 5.3(i) that the knee moment is higher in downhill compared to other activities during MST and TST. This is consistent with the biomechanical analysis that higher knee moment is exhibited in downhill to account for the negative slope of the contact surface during MST and TST [132].

The identified knee stiffness, damping, and setpoints in the experiments are used in tuning the actuator impedance for the same participant wearing the KAD. The input to the impedance tuning algorithm for ST phase is set to 10% of the identified impedance exhibited by the participant as shown in Table 5.2. For swing phase, the impedance is set to zero. The percentage value is selected based on both the torque limit of the actuator and peak human knee torque values.

5.4   Human intention estimation algorithm

The overview of the human intention estimation algorithm is shown in Fig. 5.4. This algorithm utilizes the fuzzy logic method [133] and includes two modules: gait phase detection (GPD) and activity recognition (AR). The GPD module detects four phases in every gait cycle: SF, MST, TST, and SW. In addition to the four phases, the GPD module will provide HS detection as well. Meanwhile, the AR module is used to provide estimation of three activities: level, uphill and downhill walking

5.4.1 Gait phase detection (GPD) module

The GPD module's fuzzy logic rule base is inspired by [97], where two hyperbolic functions are used as input membership functions while our GPD module's input and output membership functions are changed to partially overlapped trapezoid and triangular functions, as shown in Fig. 5.5(a) and (b). This change accounts more samples into the gait phase transition period instead of a specific gait phase and provides a smoother gait fuzzy output profile, shown in Fig. 5.6. Once a new gait phase is detected by the GPD module, the value of the knee setpoint will change correspondingly. Also, the outputs of this module will be used as part of the training data set for GMM and the input to AIT which is discussed in Section 5.

5.4.2 Activity recognition (AR) module

An fuzzy inference algorithm was developed in our previous work that can detect six activities in real time [134]. The algorithm is based on the knee angle and GCF

(a) Input membership func-
tions

(b) Output membership
functions
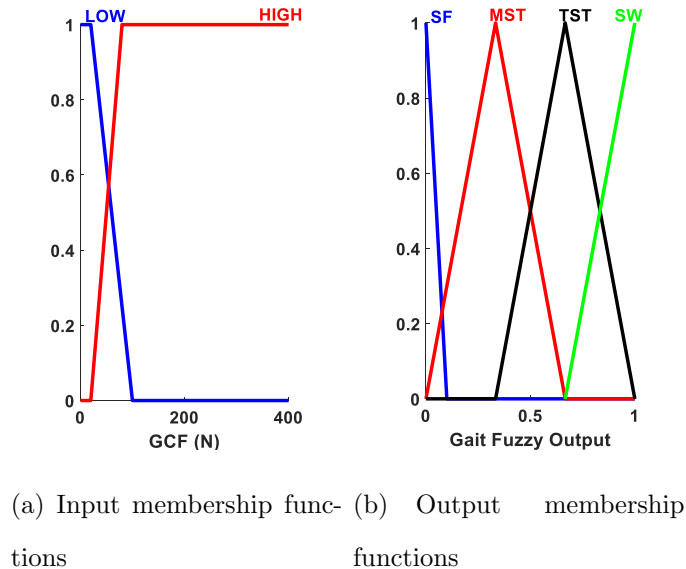
Figure 5.5: Example of the input and output membership functions of the GPD module
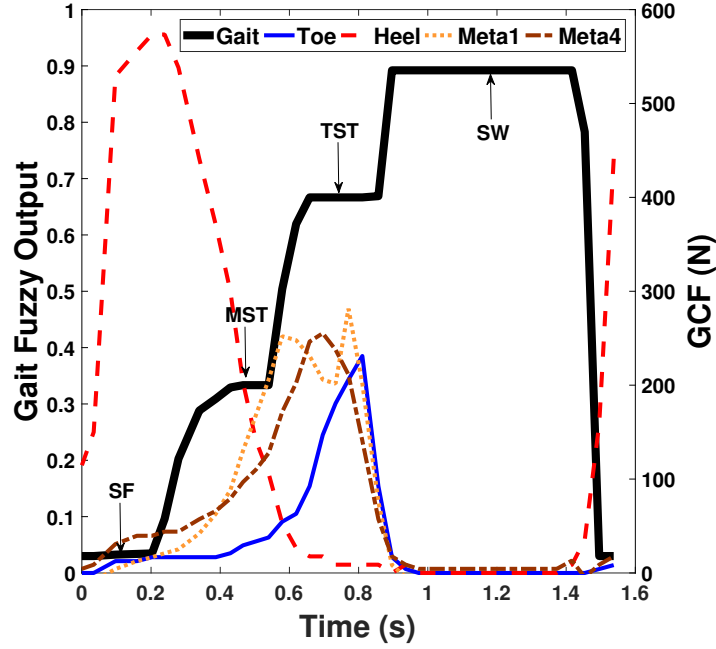
Figure 5.6: The result of the GPD module for a gait cycle of participant 1.

measurements from IMUs and smart shoes. The design of the rule base in Table 5.3 is inspired by the human walking patterns, shown in Fig. 5.3(a). It is obvious that during the SF phase, the right side knee angle is larger in the uphill case compared to the other two activities. This difference brings the definitions of high and low in the rule base for right side. Once the rule base is built, the input and output fuzzy logic membership functions are defined using trapezoid functions. The max method of aggregation and centroid method of de-fuzzification is used to generate a final fuzzy output [134]. Like the output from GPD module, this fuzzy output value will be used in impedance tuning algorithm. However, limited by the treadmill, the module is simplified to detect three activities: level, uphill, and downhill walking. To make it clear, this module will only be activated when the right side HS is detected by GPD module and the output will be kept until the next right HS happens. For both of the participants, the ranges of the activity fuzzy output values defined for level, uphill,

Activity	θ_R	θ_L
Level walk	low	medium
Uphill	high	low
Downhill	low	high

Table 5.3: The rule base for activity detection with θ_R (right) and θ_L (left) knee angles.
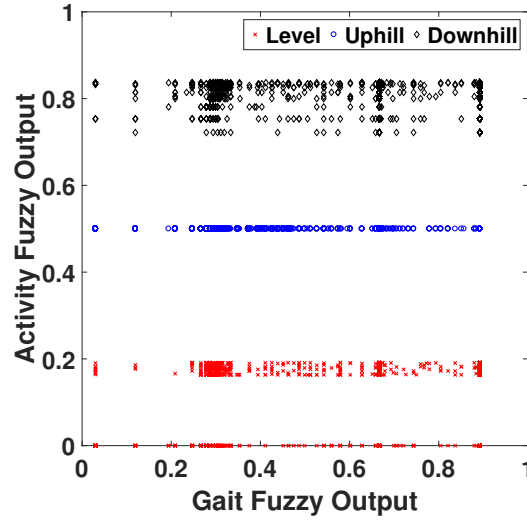
Figure 5.7: The training data set for GMM with participant 1. The participant walks at the speed of 0.8 m/s on the level surface and 0.6 m/s on 10 deg uphill/downhill condition.

and downhill walking are 0–0.3, 0.31–0.6, and 0.61–1, respectively.

5.5   Automatic impedance tuning (AIT) algorithm

The AIT algorithm is an online impedance tuning algorithm which tunes the virtual stiffness and damping values based on the fuzzy outputs from GPD and AR modules. In AIT, a GMM is trained with the gait and activity fuzzy output values obtained from the participant's walking experiments. The training dataset of a healthy participant is shown in Fig. 5.7 in which gait and activity fuzzy values are plotted on x and y axes, respectively. It can be seen from Fig. 5.7 that fuzzy values

98

along y axis is more separated compared to x axis, since the training data does not contain transitions among the activities.

Procedure 4: AIT

Input: l_1, l_2, l_3, l_4: GCF for heel, Meta 1, Meta 4 and toe sensing points, θ_L, θ_R: Left and right knee angle, k_{ij}, b_{ij}: Stiffness and damping values by knee characterization where i and j stand for the activity and gait phase classes, g_0: Threshold of fuzzy likelihood for HS detection

Output: k, b: desired actuator stiffness and damping value

1: $q_2 = 0$ $\triangleright$ AR module initialized with level walking

2: **loop**

3:    $q_1 = GPD(l_1, l_2, l_3, l_4)$ $\triangleright$ Gait fuzzy output q_1 updated

4: **if** $q_1 < g_0$ **then** $\triangleright$ HS detected

5:       $q_2 = AR(\theta_L, \theta_R)$ $\triangleright$ Activity fuzzy output q_2 updated

6: **else**

7:         $\triangleright$ HS not detected $q_2 = q_2$ $\triangleright$ Keep the previous activity detection

8: **end if**

9: $(k, b) = GMM(q_1, q_2, k_{ij}, b_{ij})$ $\triangleright$ Impedance updated

10: **end loop**

5.5.1   Gaussian mixture model (GMM)

The GMM is a parametric probability density function represented as a weighted sum of Gaussian component densities. In this , three activity components (level, uphill and downhill walking) and four gait phase components (SF, MST, TST, and SW) are separately defined on y axis and x axis which forms a 3 by 4 Gaussian components group. The Gaussian component is labeled as C_{ij} where i and j represents the activity
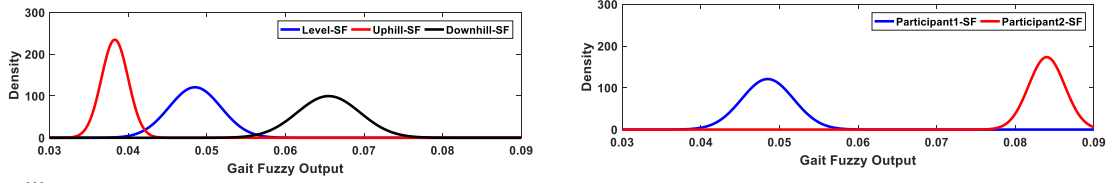
(a) The SF Gaussian components distribution in different activities for participants.

(b) The SF Gaussian components distribution in level walking for participants.

Figure 5.8: Examples of GMM components distribution.

and gait phase components respectively. Meanwhile, the outputs from GPD and AR modules are labeled as q_1 and q_2, respectively. Using the Expected Maximization (EM) method, the parameters of the GMM are identified from the training data [135]. A given new data point (q_1,q_2) firstly generates a feature vector $\mathbf{q} = [q_1, q_2]^T$. Then, the probability of this data belonging to component C_{ij} is given by Bayes rule:

$$p(C_{ij} \mid \mathbf{q}) = \frac{p(C_{ij})p(\mathbf{q} \mid C_{ij})}{p(\mathbf{q})} \tag{5.2}$$

where the prior component weighting factors $p(C_{ij})$ are set to be the same. After the possibility for each component is acquired, the desired actuator stiffness and damping values are calculated as:

$$k = \sum_{i=1}^{3} \sum_{j=1}^{4} p(C_{ij} \mid \mathbf{q})k_{ij}, b = \sum_{i=1}^{3} \sum_{j=1}^{4} p(C_{ij} \mid \mathbf{q})b_{ij} \tag{5.3}$$

where k_{ij} and b_{ij} are the identified stiffness and damping values mentioned in Section 5.3, with 3 activities and 4 gait phases, k and b are the actuator stiffness and damping values for the KAD. The AIT algorithm is described in Algorithm 4. Note that the AR module is executed only in the HS phase once every gait cycle, and the algorithm is initiated at level walking activity ($q_2 = 0$). If the HS is not detected in the next gait cycle, the algorithm will use the last AR module output (q_2) to generate the stiffness and damping values.

In this , the algorithm is reduced to a 1D GMM which focuses on the gait phase transition and its performance is verified for three activities level, uphill, and downhill with inclination angles of 0, +10 and -10 degrees. A comparison of GMM components is shown in Fig. 5.8(a) and (b). As presented in Fig. 5.8(a), the distributions of SF component in three activities: level, uphill and downhill are different which means, for a single participant, the possibilities that a gait fuzzy output value, i.e. $q_1 = 0.05$ belongs to the SF component are dependent on the activity condition. It is also obvious in Fig. 5.8(b) that, in the same activity condition, the distributions of SF component are distinct between the two participants which indicates the possibility that a given input q_1 belongs to the SF component is dependent on participant as well. These variances in the distributions of the GMM components reflect the individual's walking pattern and make this algorithm personalized to each participant.

5.5.2   Control structure of KAD

The impedance parameters need to be tuned for the KAD to provide the personalized assistance. There are two ways in the literature to provide the desired knee assistive torque by: 1) using reference knee trajectory for the gait cycle and 2) providing setpoint knee angle conditions for the gait phases [129]. There are limitations associated with the first method as the participant trajectory may deviate from the reference and it does not follow a constant pattern across gait cycles. To avoid this problem, setpoints are defined for each gait phase separately. The desired knee assistive torque follow

$$T_d(t) = k(\theta_h(t) - \theta_0) + b\dot{\theta}_h(t), \tag{5.4}$$

where T_d is the desired torque, k, b, and θ_0 are the actuator stiffness, damping and set point angle calculated from the AIT algorithm and θ_h is knee angle measurement

101

from human-side encoder. The complete control diagram of the KAD is shown in Figure 5.9. Regarding the rotary series elastic structure of the KAD, the torque is generated by the deflections of two sides of the torsional spring which is also amplified by the spur gear set shown in Figure 5.1. Therefore,

$$T = K_s(\theta_{M*} - \theta_{h*})N_s, \tag{5.5}$$

where T is the torque provided by the KAD, $\theta_{M*} = \theta_M N_W$, $\theta_{h*} = \theta_h/N_s$, θ_M is the motor angle, N_s and N_W are the spur and worm gear ratios, θ_{M*} and θ_{h*} are the worm and spur gear angles. Hence, the position reference for the motor can be calculated using (5.5) and the desired torque given by (5.4), and the torque control problem is converted to a position control problem of the motor. The motor tracks the reference position using a cascaded PID control loop, in which the inner loop controls the motor velocity and the outer loop controls the position.

5.6 Experiments and results

To verify the performance of the AIT algorithm, the same two participants in Section 3 volunteered in the identical experimental setup. The experiment proto-
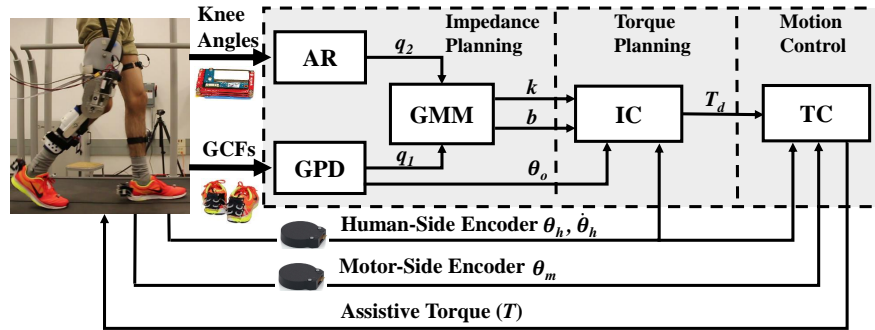
Figure 5.9: Control block diagram for the KAD. θ_0: knee angle setpoint, k: actuator stiffness, b: actuator damping, q_1: gait phase fuzzy output, q_2: activity fuzzy output, θ_h: human knee angle, and, $\dot{\theta}_h$: human knee angular velocity. IC: impedance control. TC: torque control. AR and GPD modules are discussed in Section 5.4.
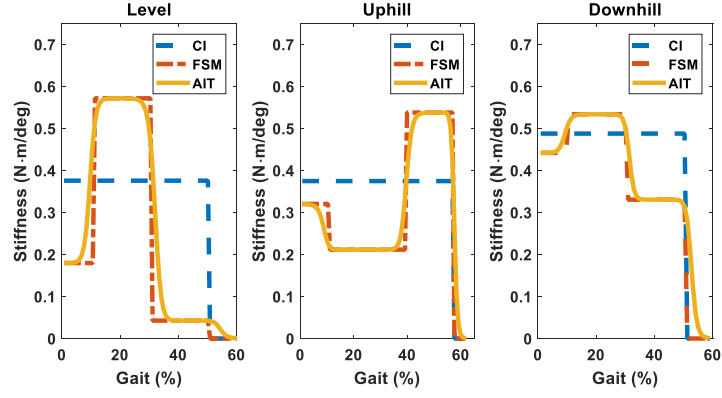
(a) Stiffness profile for three activities.
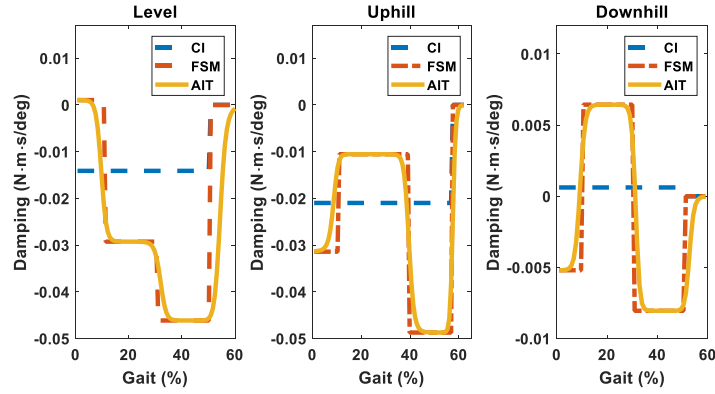
(b) Damping profile for three activities.
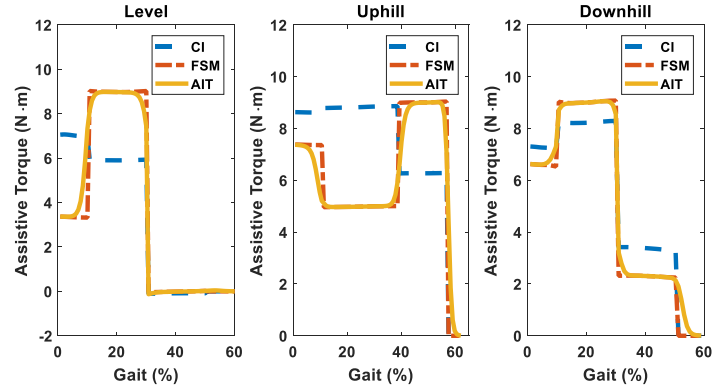
(c) Assistive torque profile for three activities.

Figure 5.10: The impedance parameters and assistive torque profile in level, uphill, and downhill activities for three cases: CI, FSM, and AIT for a healthy participant. The x axis in plots represent gait cycle in terms of percentage.

col mainly consisted of two cases: passive and active. In passive case, the device was not powered and it did not provide assistance to the participant. Whereas, the KAD provided stance assistance for the knee flexion and extension in the active case. Three types of active cases were designed for the experiment protocol: a) constant impedance (CI), b) FSM, and c) AIT. The focus of this section is to compare the performance of the AIT with the two baseline cases: CI and FSM. All the experimental sessions were planned on a single day for a participant. There were five types of sessions proposed: normal walking without KAD (w/o KAD), passive, CI, FSM, and AIT cases for each activity. The time duration for sessions and relax time between the sessions was similar to the protocol given in Section 3. Also, the sequence of the sessions were randomized to make them unbiased.

5.6.1 Impedance and assistive torque

For the implementation of CI and FSM approaches, the gait phase detection outputs need to be deterministic instead of fuzzy. To account for this, the algorithm implemented in [97] was chosen. In the CI case, the impedance was set to a constant predefined value obtained from Table 5.2 throughout the stance phase. The impedance was predefined as 10% of the normal impedance exhibited by the participant in FSM case. In the AIT case, the impedance parameters were set as 10% of the impedance obtained from the trained GMM. The desired assistive torque T_d for KAD for gait phases SF, MST, or TST was given by (5.4). The maximum desired torque for the KAD was set to 9 N·m for all activity sessions as to restrict the actuator from reaching the saturation limit.

The actuator stiffness, damping, and assistive torque for three activities are shown in Fig. 5.10. The profiles of impedance parameters and assistive torque differ for three active cases. It is clear from Fig. 5.10 that the AIT case provided smoother

impedance parameters and assistive torque profiles, and also smoother transitions between the gait phases in contrast to FSM case. It can been seen from Figs. 5.10(a) and 5.10(b) that the stiffness and damping values reaches to zero at nearly 60% of the gait cycle for three activities, which suggests the participant is in swing phase and no assistive torque is provided by KAD. It can be observed from Fig. 5.10(c) that the knee assistive torque for level walking drops closer to zero at nearly 30% of the gait cycle which is not the case in downhill or uphill walking. The reason is that the stiffness and damping values of the level walking are much lower in TST compared to SF or MST. It should be noted that applying smoothing function, for instance, the sigmoid function to FSM impedance parameters profile can lead to smoother transitions between the states. However, the drawback in such approach is parameters of the sigmoid function need to set manually to account for slope and time shift. In the case of AIT algorithm, the smoother transitions happen due to fuzzy likelihood values obtained from the trained GMM model specific to participant shown in section V. Therefore, the steepness and time shift of the transitions in AIT are participant specific. To compare the performance of proposed AIT with the standard CI and FSM approaches, there is a need to define relevant metrics. The details about the metrics are given in the following subsection.

5.6.2   Metrics and results

Three types of metrics were chosen for comparison: 1) joint kinematics, 2) gait parameters and 3) muscle activities. For muscle activity comparison, an EMG sensor was attached to vastus medialis as it plays a crucial role in generating knee assistive torque for the stance phase in all the three activities [136].

105
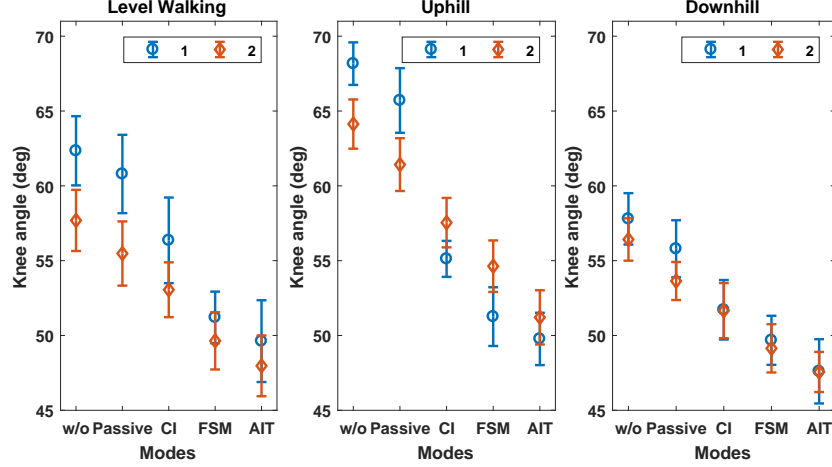
Figure 5.11: The mean knee ROM with SD for 45 gait cycles in three activities for two participants.

Joint kinematics and gait parameters

The right knee range of motion (ROM) for the two participants is shown in the Fig. 5.11 with the mean and standard deviation (SD) from 45 gait cycles during five cases. It is clear from Fig. 5.11 that the right knee ROM decreases for the active case in comparison to w/o KAD and passive cases for three activities. The participants exhibited lowest knee ROM in AIT case.

The right side step length was computed as the KAD is designed for right knee assistance. The cadence and the average right side step length in meters were calculated for 45 gait cycles shown in the Table 5.4. It is clear from Table 5.4 that cadence increases and the step length reduces with assistance. The AIT case exhibited higher cadence and lower step length in all the three activities, which can be inferred from Table 5.4. The device in passive case adds extra weight to participant's body and lower the performance of walking that is reflected in gait parameters. However, the KAD helps participants spend less effort on the knee joint in active case.

Activity	Cases	Participant 1		Participant 2	
		p_1	p_2	p_1	p_2
Level	w/o KAD	79.65	0.523	86.15	0.492
	Passive	80.84	0.511	87.21	0.478
	CI	81.16	0.497	87.67	0.457
	FSM	82.08	0.475	88.61	0.448
	AIT	82.62	0.471	89.16	0.436
Downhill	w/o KAD	83.71	0.418	90.19	0.378
	Passive	84.32	0.405	91.96	0.366
	CI	85.16	0.383	92.82	0.351
	FSM	85.79	0.374	93.09	0.348
	AIT	86.21	0.365	94.45	0.341
Uphill	w/o KAD	69.31	0.449	77.47	0.464
	Passive	70.21	0.437	78.55	0.453
	CI	71.04	0.424	79.64	0.445
	FSM	72.32	0.416	80.98	0.438
	AIT	73.14	0.410	81.64	0.429

Table 5.4: The cadence p_1 (steps/min) and average step length p2 (m) for 45 gait cycles in all cases.

Muscle activity

The maximal voluntary contraction (MVC) experiment on vastus medialis was performed prior to all experiment sessions on each participant to get the reference of the muscle activity. The procedure for MVC experiment was followed as given in [137]. The processing of the EMG signals involves full-wave rectification, detrending, and low pass filtering using 5th order Butter-worth filter [138]. The EMG signals were recorded with a sampling rate of 1000 Hz. Two metrics for muscle activity were chosen: 1) Average EMG activity reduction ($P\%$): first, the average of the peak

(a) Level walking

(b) Uphill walking

(c) Downhill walking
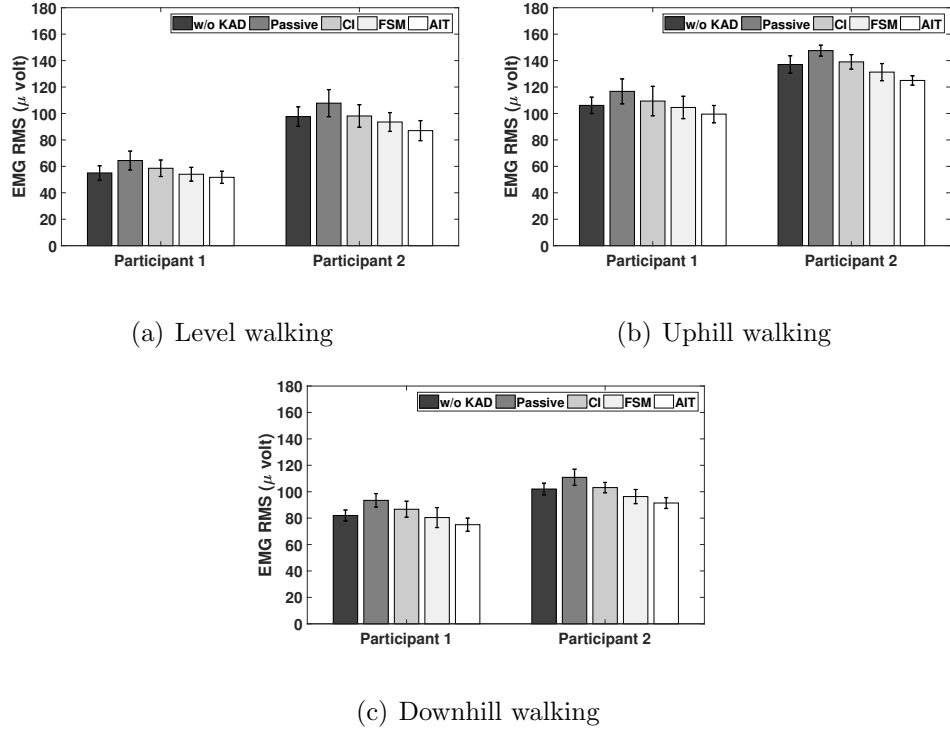
Figure 5.12: The average RMS of EMG signals of vastus medialis with SD measured for 45 gait cycles in three activities and five cases, respectively.

values of the processed EMG signals was normalized with respect to MVC value for all five cases; Second, $P\%$ was obtained by computing the percentage reduction of those values in passive and three active cases with respect to w/o KAD case. In conclusion, $P\%$ metric gives the measure of change in normalized muscle activation levels in four cases with respect to normal walking. 2) Average root mean square (RMS) of EMG: The RMS of the processed EMG signal with a moving fixed time window is calculated.

The average RMS of the EMG signals with SD during three activities for 45 gait cycles are reported using a bar chart in Fig. 5.12. Along with the four cases, w/o KAD case is included for comparisons. It is clear that the AIT performed best in reducing the average RMS value of the EMG signals. The passive and CI cases showed more average RMS in EMG signals in comparison with w/o KAD. This can be explained

Activity	case	Participant 1	Participant 2
Level	Passive	-11.19%	-8.06%
	CI	-4.78%	-1.48%
	FSM	1.53%	5.07%
	AIT	6.64%	9.27%
Downhill	Passive	-8.16%	-6.57%
	CI	-5.17%	1.05%
	FSM	1.77%	6.33%
	AIT	5.80%	10.99%
Uphill	Passive	-6.95%	-9.14%
	CI	-3.40%	-4.82%
	FSM	2.69%	2.07%
	AIT	8.14%	6.78%

Table 5.5: The average EMG activity reduction ($P\%$) for 45 gait cycles in all cases.

by the weight of the KAD device on the participant. The FSM showed nearly the same or less RMS value compared to w/o KAD. This can also be verified from $P\%$ displayed in Table 5.5. The passive and CI case showed negative $P\%$ which suggests that the normalized EMG value increased in comparison with the w/o KAD case.

5.7   Discussion

The KAD assists the participants in stance phase and follows zero impedance strategy during swing phase. It can be seen from the knee angular velocity plot shown in Fig. 3(b) that the swing phase is characterized by high angular velocities. During high angular velocities, the KAD response is increasingly governed by the intrinsic stiffness of the joint which results in resisting torque. Therefore, this alternative

assistance and resistance provided by the KAD during stance and swing phases of the gait cycle influences the participants knee ROM. As shown in Fig. 5.11, the reduced knee ROM is observed in active cases in comparison to passive or w/o KAD case. Also, the other reason could be that the device introduces inertia and friction due to its weight, which leads to decreased knee ROM. From Table 5.4, it is clear that the participants exhibited increased cadence and decreased step length. The probable reason can be that as the speed of the treadmill is fixed, the subject need to compensate for reduced knee ROM with increased cadence. This is confirmed in the study of Aoyagi et al. where the inertia of assistive device results in a reduced range of pelvic motion during zero impedance case [139]. Also, a decrease in knee ROM is observed when walking with LOPES lower limb orthosis in zero impedance case [140]. From the studies [139] and [140], it was shown the reduced joint ROM caused direct effect on gait parameters: step time, step length, and stance time. Also, the subjects showed a tendency to take shorter and quicker steps. As KAD follows zero impedance strategy in swing phase, similar results of reduced knee ROM are observed.

The percentage improvement of the RMS value of the EMG signals for participant 1 in the AIT case compared to w/o KAD for level, uphill, and downhill walking are 6.03%, 6.22%, and 8.52%. Whereas, FSM showed 1.8%, 1.4%, and 1.92% improvement. Similarly, for participant 2, the AIT case exhibited a noticeable improvement in EMG RMS value with respect to w/o KAD that is 10.88%, 8.80%, and 11.36% for level, uphill and downhill walking. Similar results can be inferred by looking at $P\%$ for both the participants. The FSM and AIT active cases provided nearly equal assistive torques for gait phases. However, a clear distinction in the muscle activity is observable and AIT performs better than FSM. The possible reason can be that AIT provides smoother impedance and torque profile for the actuator in comparison with the FSM.

110

5.7.1 Clinical implications

The approach proposed in this addresses the limitations of FSM and provides smooth continuous impedance parameters using the identified human joint impedance. The approach has the potential to become a personalized training system for patients. More experiments need to run to define the impedance parameters for the fuzzy clusters of gait and activity based on the requirements of the patients and the GMM will output the impedance parameters adaptively. As a proof of concept, the knee joint is considered in this . It is possible to extend this framework to multiple joints. As the AIT approach provides flexibility in designing the impedance parameters for the clusters of gait and activity, it will be advantageous in clinical settings, as it allows variability in walking pattern, more personalized walking patterns. Also, AIT can provide different impedance parameter profiles, thereby providing various levels of assistance depending on early, mid, and final stages of rehabilitation.

Regarding the effectiveness of this approach in rehabilitation, a clinical protocol with a therapist is needed, in practice, to evaluate the method of automatic impedance modulation and its effect on patients. With this purpose, a graphical user interface (GUI) will be useful for the therapists, in order to facilitate the monitoring of variable such as knee ROM, step length, or cadence and choosing impedance profile.

5.7.2 Limitations of this study

Due to the limitation of the slope change operation of instrumented treadmill used for the experiments, the transitions between different activities are not evaluated. Therefore, the three activity experiments are conducted separately. In future experiments, the activity transitions will be included. In experiment trails, the speed is fixed along with slope of the treadmill. The speed change during experiments might

111

have provided more insights into the study of human impedance modulation. In this study, the AIT approach is evaluated on healthy subjects and not on impaired subjects. It will be useful to observe the fuzzy likelihood profiles of gait and activity for impaired subjects. In this work, the AIT approach is designed to make it suitable for rehabilitation training in the indoor environment. The authors believe that the AIT have the potential for the applications in outdoors as well. However, the complexity of the problem increases in terms of gait speed, terrain conditions, and more activities.

To summarize, an online impedance tuning algorithm was proposed for a knee exoskeleton to provide personalized assistance based on simultaneous detection of activity and gait phase. Human knee impedance was characterized by collected walking data. The uncertainty of activity and gait phases was modeled with a fuzzy likelihood, and a GMM was developed to determine the desired robot impedance. The AIT was compared with CI and FSM approaches in a study with two participants. The AIT algorithm led to reduction of vastus medialis muscle activity, and it also yielded increased cadence and reduced step length in comparison to baseline approaches.

Chapter 6

THE ASSESSMENT OF OVERALL STABILITY OF HUMAN-LEAD SYSTEM USING METRICS DERIVED FROM DYNAMICAL SYSTEMS THEORY

A variety of Lower Extremity Assistive Devices (LEADs) have been proposed for gait assistance to elderly and patients with neurological issues. The main focus of these systems is to provide assistance, however, the dynamic gait stability of the human-LEAD system has not been examined thoroughly. This focuses on assessing the stability metrics derived from dynamical systems theory to evaluate unilateral knee assistance applied to the healthy participants, and moreover, to understand the influence of unilateral assistance on the walking pattern from chaotic dynamics perspective. A knee assistive device (KAD) is designed to provide unilateral knee assistance to the right knee joint during the stance phase. In this , we hypothesize unilateral knee assistance applied during stance phase as the perturbation applied to the human in a gait cycle, and stability is defined as the gait that does not lead to falling in spite of perturbations. The metrics related to global stability (the maximum Floquet multiplier Max FM), local stability (divergence exponents λ_s and λ_l), and variability (median absolute deviation MAD) are considered. These metrics are derived for joint angle time series of bilateral hip, knee, and ankle joints. Additionally, a biomechanical metric, the minimum margin of stability (b_{min}) between the center of pressure and center of mass is assessed. Full biped model walking simulations are performed to understand the influence of the assistance on the normal walking pattern. To assess the stability metrics for the human-LEAD system, experiments are conducted on 8 healthy participants for five conditions: normal walking, passive, zero impedance, finite state machine (FSM), and automatic impedance tuning

113

(AIT). The Max FM and λ_s yield statistically significant results, showing that the unassisted (left) leg is more stable for unilateral right knee assistance conditions (FSM and AIT) when compared to the normal walking condition due to inter-limb coordination. On the other hand, MAD and λ_l converged well to bipedal simulation results, showing that the variability and chaotic order of walking pattern during assistance is lower than the normal walking. The assessment of stability metrics for human-LEAD system presented in this set foundations to better analyze the dynamic stability of the human-LEAD system and further improve the control strategies of the assistive devices to maintain both gait stability and gait variability.

6.1   Related work

The aging in population has become a socio-economic problem in many countries. A survey from the United Nations reveals that people older than 60 years which are 11.5% of the global population in 2012, will be nearly doubled by 2050 [141]. Aging is reflected by reduced daily physical activities due to increased muscle weakness. This deterioration of muscles could further accelerate the degradation of the neuromusculoskeletal systems and their interactions and may lead to impaired gait disorders [142]. Similar problems are prevalent in patients encountered with stroke and spinal cord injuries. These neurological injuries and weaknesses of the skeletal muscles seriously limit the ability of the patients to perform walking [143]. Current research challenges mainly focus on the development of new assistance modes that help the elderly/patients to improve their walking performances and to restore lost or impaired motion control. Lightweight and wearable robotic Lower Extremity Assistive Devices (LEADs) provide one promising solution by assisting their walking [144]. Some successful examples include Hybrid Assistive Limb known as HAL (Cyberdyne, Japan) [145], Rewalk (Argo Medical Technologies, Israel) [120], Ekso (Ekso Bionics, USA)

114

[121], and Vanderbilt Exoskeleton (Vanderbilt University, USA) [146].

One main concern among the elderly and patients with neurological diseases is falling during walking which pose a major challenge and can lead to serious health problems [147, 148]. In the aforementioned examples for LEADs, the major focus is put on providing assistance to improve walking performance and the assessment of the dynamic gait stability of the combined human LEAD system is not considered [149, 72]. The metrics related to muscle activity and metabolic cost are assessed to evaluate the level of assistance provided by LEAD to the human [149]. However, there has not been much focus put on evaluating dynamic gait stability of the human-LEAD system. Dynamic stability is defined as the response of the system to the perturbations such that the states of the system do not go unbounded and stay within a certain range. Therefore, we can define the stable gait as the gait that does not lead to falling in spite of perturbations [150]. We hypothesize that LEAD as an external device attached to the body may induce perturbations during assistance and may influence the inherent stability of the human. Therefore, it becomes important to study the human gait and introduce stability metrics as an assessment to compare the inherent stability of human with the overall dynamic gait stability of the human-LEAD system.

The stability assessment methods allow discrimination of the individuals at the risk of falling. Although many gait stability criteria have been proposed, there is still no commonly accepted method to assess locomotor stability. Most of these metrics reflect the robustness (the ability to respond to large perturbations such that the system states stay in safe range) and the performance (how quick the system can respond to the perturbations and stay in the safe range) [150]. Nevertheless, these measure can still be used to assess the likelihood of falling as they quantify how system respond to perturbations.

There are metrics derived from dynamical systems theory (the maximum Lyapunov exponent, the maximum Floquet multiplier, variability measures, and long-range correlations) for stability assessment during gait. The computation of these metrics is based on the time series data of kinematics and/or gait parameters. Dingwell et al. used the maximum Lyapunov exponent to estimate gait stability [151]. The maximum Lyapunov exponent (λ) quantifies the average logarithmic rate of divergence of a system after a small perturbation. For chaotic systems, (λ) is always negative. The lesser the λ value, the more stable is the system. In many gait studies, the maximum Lyapunov exponents are defined over two regions, 0 to 1 stride (labelled as λ_s), 4 to 10 strides (labelled as λ_l). Lockhart and Liu reported that a greater λ_s in fall-prone elderly subjects than in normal elderly subjects [152]. McAndrew et al. reported that gait destabilization by means of support surface perturbations or visual scene perturbations was reflected in λ_s, but probably not in λ_l [153]. This finding has recently been confirmed by Hak et al, who even showed a dose-response relationship between the amplitude of the perturbations applied and the increase in λ_s [154]. In summary, the findings obtained in experimental studies suggest that, in actual human gait, λ_s, but not λ_l, as a valid measure to estimate the probability of falling.

Another measure derived from dynamic systems theory is the concept of orbital stability which was defined by computing the maximum Floquet multiplier which quantifies the rate of convergence or divergence of continuous gait variables (e.g. segmental motions and joint angles) towards a limit cycle (e.g. the nominal gait cycle). The system with the maximum FM value less than 1 is considered as a stable system. The lesser the Max FM below 1, the more orbitally stable is the system. Granata and Lockhart reported that the maximum Floquet multiplier was larger in a group of four fall-prone elderly (i.e. elderly who had a self-reported history of falling) than in four elderly controls [155]. In [153], the maximum Floquet multiplier showed expected

effect on gait destabilization by means of visual perturbation experiments. However, in [156], the maximum Floquet multiplier does not correspond to the probability of falling. The concept of orbital stability showed mixed results in relation to the probability of falling. Some used the variability of certain parameters over strides as a measure to assess stability during walking. The median absolute deviation was proposed as a measure for gait variability [157, 158]. In general, the median absolute deviation is more robust than the standard deviation, and may thus be a good choice to use as an indicator of variability [159]. Others tried long-range correlation which exhibit dependencies i.e., future variations are dependent on past variations [160]. These long-range correlation metrics did not show any experimental evidence related to the falling.

Apart from the measures from dynamical systems theory, the biomechanical measures are the most commonly used to assess stability during gait due to their general principles and physical intuition. In a study, the extrapolated center of mass (margin of stability) is derived for the subjects who are destabilized using the platform and visual perturbations [161]. It is found that during destabilized conditions, subjects walked with a higher margin of stability, indicating that subjects were actually more stable when walking in a destabilizing environment. Some introduced the concept of stabilizing and destabilizing forces to assess stability during gait [162]. However, these metrics did not show any experimental evidence relating to the risk of falling.

6.1.1   Chaos and Optimal Variability

Human gait is not strictly periodic. Any variations from the periodic pattern have traditionally been considered to be noise in the neuromuscular system [163]. However, later investigations have shown that these variations follow chaotic structure [164, 165]. To understand gait variability, we cite [166], a theoretical model (predictability

117
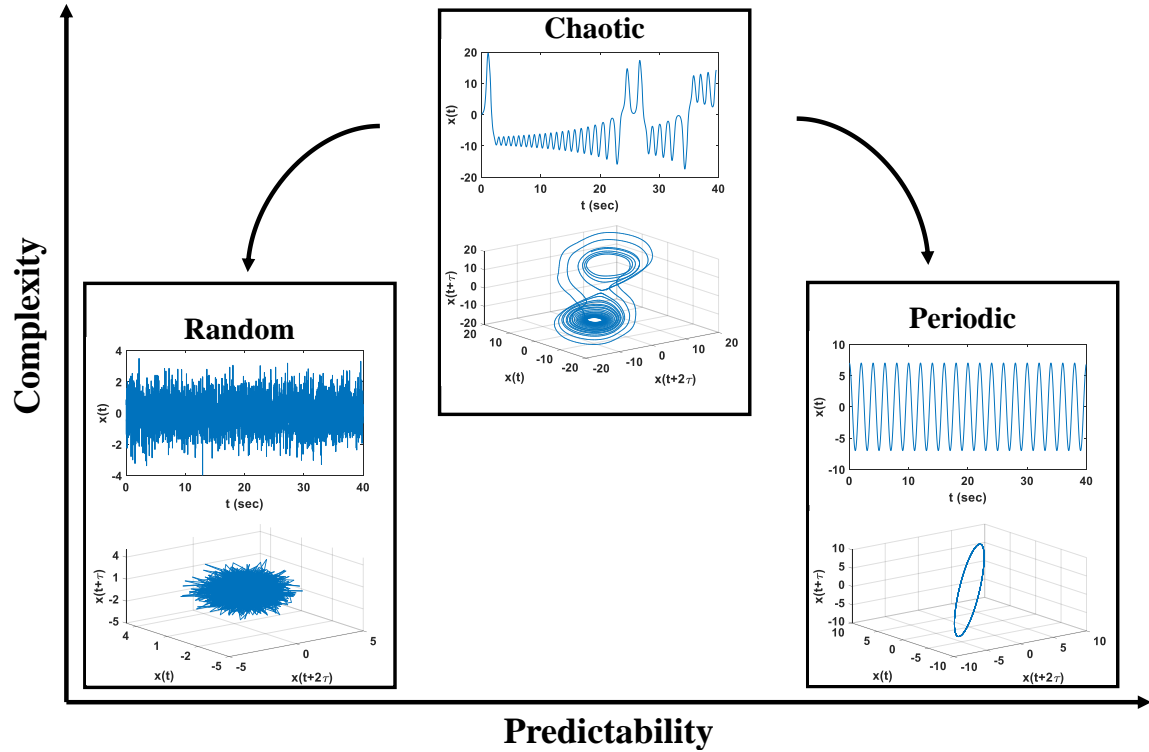
Figure 6.1: Theoretical model for optimal variability illustrated using random, chaotic, and periodic signals. Behavior in terms of variability should be viewed in a continuum as being more or less predictable (on the x-axis) or exhibiting or not chaos (on the y-axis).

vs complexity) proposed to explain movement variability as it is related to motor learning and health. The model is based on the idea that mature motor skills are associated with optimal movement variability that reflects the adaptability of the underlying control system. The principle of optimality in movement variability is pioneering in the sense that it relates in an inverted U-shape relationship the presence of chaotic temporal variations in the steady state output of a healthy biological system with the concept of predictability (shown in Figure 6.1). Practically at this optimal state of movement variability (chaotic block), the biological system is in a healthy state and is characterized by exhibiting chaotic temporal variations in the steady state output (i.e., the uppermost point along the inverted U-shaped function), attaining high values only in the intermediate region between excessive order (i.e., maximum

predictability) and excessive disorder (i.e., no predictability). Thus this variability has deterministic structure and reflects the adaptability of the system. This model provides an explanation for the neuromuscular control of the human gait. This implies that the stride to stride variability follows chaotic structure i.e., optimal variability. Also, chaotic systems are described as being both stable and flexible. This system has an ergodotic property that the trajectories come close to a fixed point's neighborhood but never converge to the specific point. Therefore, useful insights will be gained studying human gait from chaos perspective and stability metrics related to chaos and nonlinear dynamics will be useful in assessing the stability of the human gait.

In the previous chapter, we developed an impedance based control strategy known as automatic impedance tuning (AIT) algorithm for KAD. The AIT algorithm displayed better performance in terms of EMG muscle activity reduction compared to the baseline approaches constant impedance (CI) and finite state machine (FSM). However, the dynamic stability of human wearing KAD is not discussed. In this chapter, the focus is put on the evaluation of the influence of KAD on the inherent dynamic stability of the human. To assess dynamic gait stability of the human-KAD system, the stability metrics are derived from dynamical systems theory. The dynamical systems and chaos theory is adopted to understand the human walking pattern. As a primary step, simulations are performed on a full bipedal model with hip, bilateral knee, and bilateral ankle joints to understand chaos in gait. To assess the influence of assistive device through simulations, an active actuator at the knee joint is implemented. Then, to verify the simulation results and assess the stability metrics, the experiments are performed on eight healthy participants. The metrics derived from dynamical system theory such as the maximum Floquet multiplier, the finite-time Lyapunov exponents and median absolute deviation (MAD) variability measures are used on the lower limb joint kinematic time series. Along with these

metrics, the extrapolated center of mass ($XCoM$) is used as a biomechanical measure. As a LEAD system, in this chapter, a knee assistive device (KAD), which provides assistive torque to the knee joint is used. Five types of walking modes are tested on each participant: normal walking, passive (KAD not active), zero impedance (ZI), a finite state machine (FSM), and automatic impedance tuning (AIT).

The chapter is organized as follows: Section 6.2 gives details about the experimental setup and hardware used in the experiments. Section 6.3 introduces the stability metrics derived from dynamical systems theory and biomechanics. Section 6.4 discusses the results of biped simulations and stability metrics for all the experiment cases. Section 6.5 assesses the stability metrics results obtained in the results and discusses the effects of unilateral assistance on both legs.

6.2   Methods

6.2.1   Experimental Protocol

The experiments for this were setup in the motion capture laboratory equipped with 12 high-speed infrared cameras (Vicon Motion Systems Ltd.,) and instrumented treadmill (Bertec Corporation) at Arizona State University (ASU). The ASU Institutional Review Board (IRB) reviewed and approved this study. The details of the healthy participants volunteered in this experiment are given in Table 1. The experimental protocol mainly consisted of five sessions: normal walking, passive, zero impedance (ZI), the finite state machine (FSM), and automatic impedance tuning (AIT). In passive case, the knee assistive device (KAD) was not powered and it did not provide assistance. In ZI case, the impedance parameters of the KAD was set to zero and the KAD tracked the knee range of motion of the human without providing assistance. In FSM and AIT conditions, the KAD provided assistive torque to the

right knee. The slope and speed of the treadmill for the walking experiments was set to 0 degrees and 0.8 m/s, respectively. Each session lasted for three minutes. The participants relaxed for 15 minutes before starting the next session. All the sessions were planned on a single day. Also, the sequence of the sessions was randomized to make them unbiased. The experiment setup for the participant walking on the treadmill is shown in Figure 6.2.

For the experiments, the participants wore 16 reflective markers, KAD, and smart shoes. The Vicon cameras capture markers at a frame rate of 100 Hz. The instrumented treadmill captures 3D ground reaction forces at 1000 Hz. The plug-in gait Vicon computes the lower body joint angular displacements and gait parameters using measurements from cameras and instrumented treadmill. The smart shoes provide ground contact forces (GCFs) measurements in real-time. Using GCFs measurements, the impedance parameters of KAD are modulated for both FSM and AIT conditions. The implementation details for tuning the impedance parameters of KAD for FSM and AIT conditions are given in chapter 5. The knee angle and knee torque data collected from the normal walking session was used to identify the human knee impedance parameters. Then, smart shoes GCFs data along with identified human impedance parameters were used to train the AIT algorithm.

6.2.2   Hardware Design

The knee assistive device (KAD) design targets people with unilateral impairment which affects knee function. In this , the KAD is used to assist right side knee. A knee assistive device (KAD) is an exoskeleton with a compact rotary series elastic actuator (cRSEA). In a cRSEA, a worm gear and spur gear combination is used to amplify and change the direction of assistive torque generated by a DC motor. The mechanical design of KAD is shown in Figure 6.3 (a). The cRSEA is compact
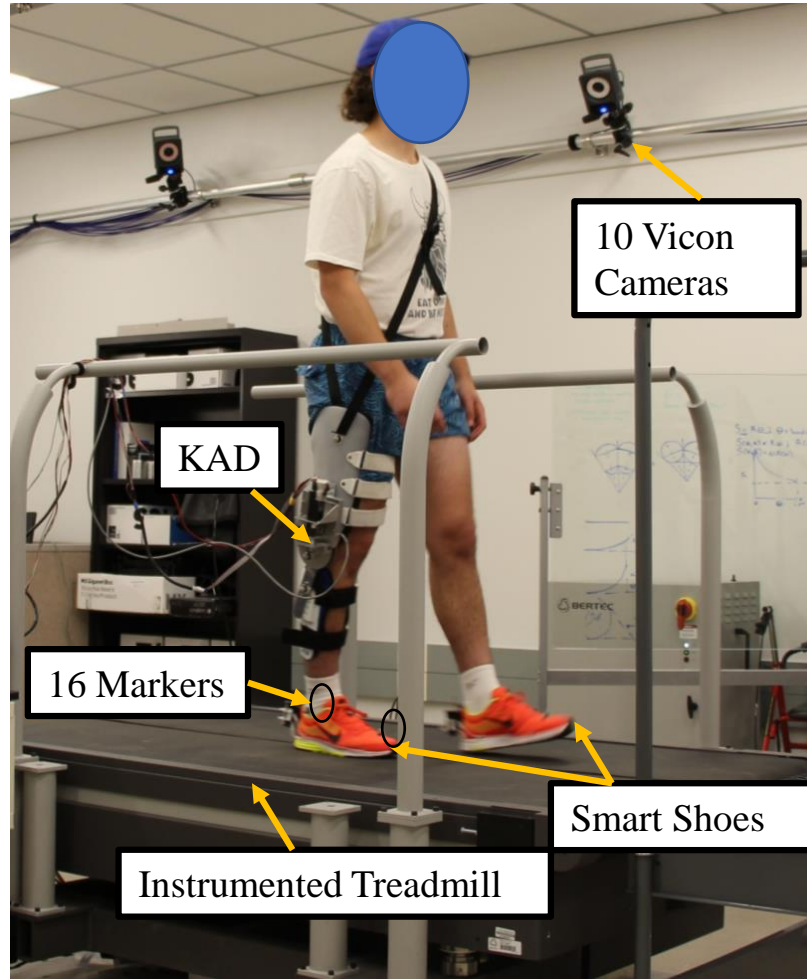
Figure 6.2: Experiment setup: participant walking on the instrumented treadmill wearing reflective markers, smart shoes, and KAD.
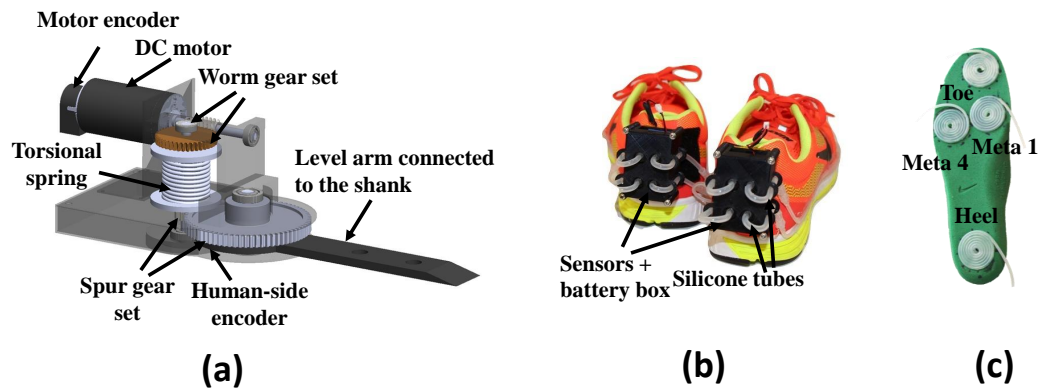
Figure 6.3: Hardware design of the wearable system. (a) The CAD for knee assistive device (KAD). (b) sensor box and (c) shoe insoles of the smart shoes

ID	Gender	Age	Height (cm)	Weight (kg)
1	Male	23	180	60
2	Male	20	175	94
3	Male	25	178	69
4	Male	22	182	61
5	Male	24	173	62
6	Male	26	172	67
7	Male	29	165	70
8	Male	20	175	79

Table 6.1: The details of healthy participants volunteered for the experiments.

and light with a weight of 1.57 kg to avoid unbalance and discomfort to users. The maximum power consumed by the knee joint is about 80W for a male subject with the body weight of 70 kg and during level walking and the knee angular velocity ranges between ±60 rpm Considering this, Maxon RE40, a 150W DC Motor is used to power the KAD. With a combined gear set reduction ratio of 63.6:1, the end effector can reach a maximum angular velocity of 120 rpm and the KAD can provide a maximum continuous assistive torque of 11.26 N·m. Two incremental optical rotary encoders (US Digital) are used to measure both motor and human knee angles, which are re-initialized at the beginning of each experiment. The torsion spring serves as a torque sensor and also provides an energy buffer to prevent injuries from unexpected high motor torques.

The smart shoes are developed to measure GCFs at four points: heel, first metatarsal joint (Meta 1), fourth metatarsal joint (Meta 4) and toe while the silicone tubes are wound into air bladders and connected to barometric pressure sensors shown in Figure 6.3 (b) and (c). The sampling rate of the smart shoes is set to 100 Hz and a

model-based filter is implemented to compensate for hysteresis and estimate GCFs from pressure sensor readings in real time [130]. The gait phases are detected using the fuzzy logic based algorithm developed in [134].

6.3   Stability Metrics

6.3.1   Measures from dynamical systems theory

There are two types of stability: global or orbital stability, and local stability. Global stability refers to the ability of the system to accommodate finite perturbations [167]. Whereas, local stability refers to the sensitivity of the system to infinitesimally small perturbations [165]. In this section, three measures derived from dynamical systems theory are described, namely the maximum Lyapunov exponent, the maximum Floquet multiplier, and median absolute deviation (MAD). These measures are generally computed from a steady-state walking pattern without any external perturbations other than those that are present in the system itself.

State space reconstruction

It is important to reconstruct the state space for time series signals for both local and orbital stability analysis. The state spaces for each individual time series are constructed from the original data and time-delayed copies using standard techniques given in [168]

$$S(t) = [x(t), x(t + \tau), x(t + 2\tau), ..., x(t + (d_E - 1)\tau)] \tag{6.1}$$

where $S(t)$ is the d_E dimensional state vector, $x(t)$ is the original one-dimensional data. τ and d_E are the time delay and embedding dimension. The time delays are calculated from the first minimum of the average mutual information (AMI) function [168]. The embedding dimensions are determined from global false nearest neighbors

(GFNN) analysis [168]. An example for the computation of d_E and τ is shown in Figure 6.4 (b) and (c). In Figure 6.4 (b), the FNNs (%) does not change for $d_E > 5$. This implies the optimal d_E for time series signal $x(t)$ is 5. The first minimum in the plot between AMI and τ occurs at 36th sample, which implies the optimal time delay τ should be 36. It should be noted that as long as τ is reasonable and d_E is sufficiently large, the reconstructed state space exhibit same dynamical properties as the original state variables. Thus, the results of local and orbital stability analysis will be insensitive to moderate changes in the parameters.

Local stability

The local stability measures provide a direct way to analyze the chaotic order of the system using finite-time divergence exponents. The local stability is quantified by estimating the average exponential rates of divergence of initially neighboring trajectories in state space as they evolved in time. These local divergence exponents provide a direct measure of the system's sensitivity to local perturbations. Positive exponents indicate local instability and larger exponents indicate greater sensitivity to local perturbations.

The nearest neighbor points in adjacent trajectories in the reconstructed state space represent the effects of small local perturbations of the system. The average exponential divergence for each embedded time series is provided by the algorithm given in [169]. The euclidean distance between neighboring trajectories are computed as a function of time and averaged overall original pairs of initially nearest neighbors. The local divergence exponents (λ) are estimated from the slopes of linear fits to these exponential divergence curves.

$$y(i) = \frac{1}{\Delta t} < \ln[d_j(i)] > \tag{6.2}$$
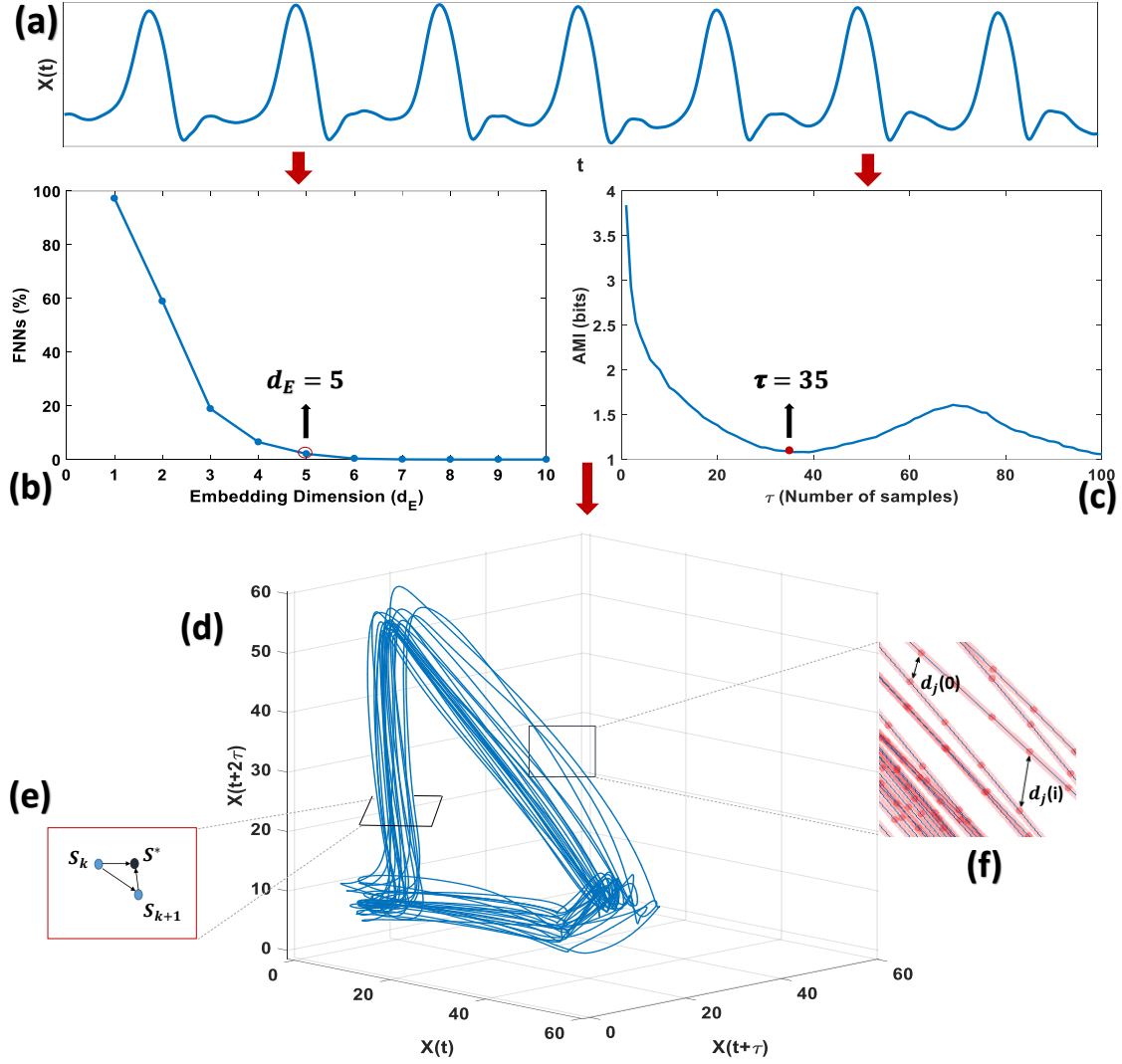
Figure 6.4: The representation of the process of the FM and λ calculation from the kinematic time series data: (a) sample knee joint time series data. (b) and (c) the FNNs and AMI plots resulting from the time series, to calculate the proper embedding dimension (d_E) and time delay (τ). (d) the three dimensional view of the reconstructed state space from the time delayed copies of the time series data (the original state space is 5 dimensional). (e) representation of a 2d map to calculate the FM values. (f) diverging of the distance between neighbouring trajectories which will be reflected in λ values.

Where $d_j(i)$ is the Euclidean distance between jth pair of the initially nearest neighbors after i discrete time steps (i.e., $i\Delta t$ seconds) as shown in Figure 6.4(f), and $< . >$ denotes average over all pairs of j. The embedding dimension of the reconstructed

126

space j is determined using GFNN analysis [168]. The short-term exponent (λ_s) is calculated from the slopes of linear fits to the divergence curve between 0 and 1 stride. The long-term exponent is calculated between 4 and 10 strides.

Orbital stability

The orbital stability concept is based on the assumption that the gait has a fixed period. It is defined using Floquet multipliers (FMs) that quantify, discretely from one gait cycle to the next, the tendency of the system's state to return to the periodic limit cycle orbit after small perturbation [170]. FMs are the eigenvalues of the Jacobian of the map. The first step for calculating the FMs is to normalize the state space data of each stride to 101 samples (0-100% gait cycle) as previously done in [171]. This will allow us to define 101 maps for the system as

$$S_{k+1} = F(S_k) \tag{6.3}$$

where k is the index of the individual strides and S_k represents the system state given in (6.1) for a single point in normalized time within each gait cycle. Limit cycle trajectories that correspond to single fixed points in each map is

$$S^* = F(S^*) \tag{6.4}$$

For walking data, fixed points at each section (i.e., each % of the gait cycle) are defined by the average trajectory across all the strides with in a trail. Orbital stability at each section is estimated the effects of small perturbation away from these fixed points, using a linear approximation of (6.4) given by

$$[S_{k+1} - S^*] = J(S^*)[S_k - S^*] \tag{6.5}$$

where $J(S^*)$ is the Jacobian matrix for the system at each section. The FMs are the eigenvalues of $J(S^*)$. Any deviation from the fixed point is multiplied by FM

of the subsequent cycle. Therefore, the condition for the limit cycle to be orbitally stable is that the complex valued FMs must have magnitude < 1 (i.e., must all lie inside the unit circle). The limit cycle FMs with magnitude > 1 are considered as orbitally unstable. For statistical analysis, the largest of the maximum FMs (Max FM) across all sections are extracted as this represents the instant during the gait cycle that is most unstable.

Variability

The measured variability in the complex dynamical system may arise from the deterministic dynamics of the system itself (for example chaotic attractor, which is the case for human gait). In such case, variability is a just a reflection of multiple degrees of freedom available to the system and does not imply destabilization of the system. Although, the variability in the biological system is likely to obtain from either noise or deterministic sources, it is difficult to separate them. However, on a pragmatic level, the variability is critical to the stability of the walking which gives the insights regarding state deviation which may lead to falling. In general, the median absolute deviation is more robust than the standard deviation, and may thus be a good choice to use as an indicator of variability [26]. For continuous variables such as joint angle time series, they are first separated into individual strides using heel strike events. These individual strides are then time normalized (0-100%) and aligned. For each of the aligned time intervals, the variability is then calculated using median absolute deviation (MAD) metric.
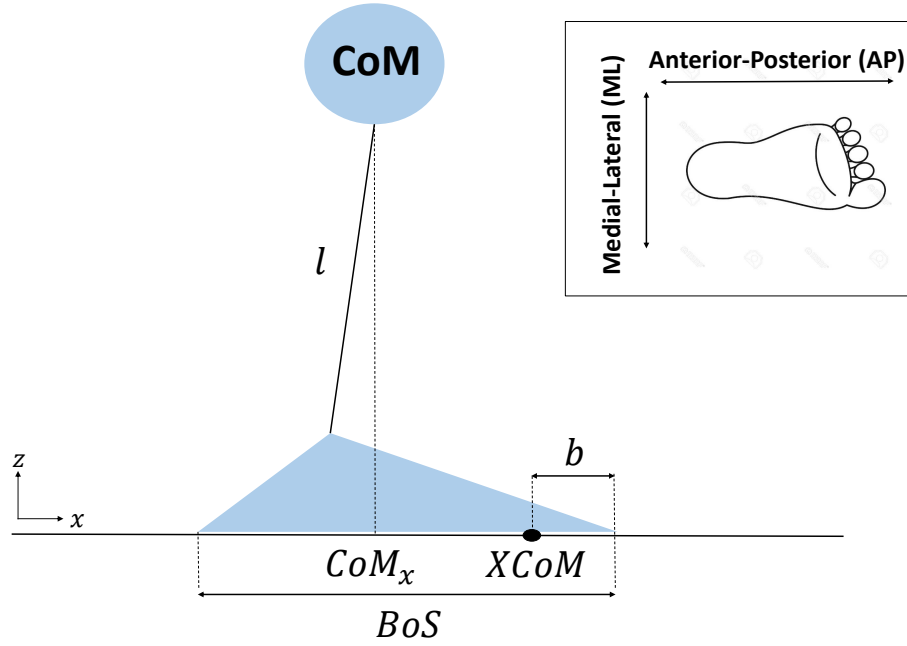
Figure 6.5: Schematic representation of inverted pendulum model to calculate the minimum margin of stability (b_{min}) in AP direction

6.3.2 Measures from Biomechanical Principles

The Extrapolated Center of Mass (Margin of Stability)

The extrapolated center of mass ($XCoM$) method extends the condition of the static equilibrium of the inverted pendulum model, in which the CoM must be positioned over the base of support (BoS) by adding a linear function of the velocity of the CoM to the CoM position [172]. This concept is widely used to describe human walking, and is a representative of gait robustness. In theory, this method describes how close an inverted pendulum is to falling, given the position and velocity of its CoM, and the positions of the margins of its BoS as shown in Figure 6.3.2. The $XCoM$ can be used to calculate the spatial margin of stability 'b'.The margin of stability refers to the distance between CoM and border of the BoS. The calculation is derived in [172] for unperturbed walking. Given the position and velocity of the CoM, the $XCoM$

129

can be calculated as:

$$XCoM = CoM + \frac{V_{CoM}}{\omega_0} \tag{6.6}$$

$$\omega_0 = \sqrt{\frac{g}{l}} \tag{6.7}$$

where V_{CoM} is the velocity of CoM, ω_0 is the pendulum eigenfrequency, g is the acceleration of gravity, and l is the pendulum length, which in this case will be the height of the position of CoM. The margin of stability can be defined as:

$$b = BoS - XCoM \tag{6.8}$$

Which is a representative of the maximum perturbation to the CoM before the inverted pendulum become unstable (CoM moving past the BoS). The minimum of b (b_{min}) shows the most unstable point within a step [172].

For the calculation of margin of stability, the positions of CoM and BoS need to be determined. The center of pressure (CoP) is estimated using the force measurements from the instrumented treadmill. It is assumed that BoS coincides with the CoP [173]. The CoM can be estimated using the filtering of the CoP estimates as given in [173].

6.4   Results

6.4.1   Biped Walking Simulations

Although the control of the gait can arise from the nervous system, the mechanical factors such as mass, inertia, and gravitational forces influence the behavior of the human's gait. Therefore, it is important to understand how the external assistive devices influence the dynamics and chaotic structure of the human locomotion. These insights will be gained through the walking simulations of a full bipedal model i.e., combining the stance and swing legs together. Later the results will be compared to
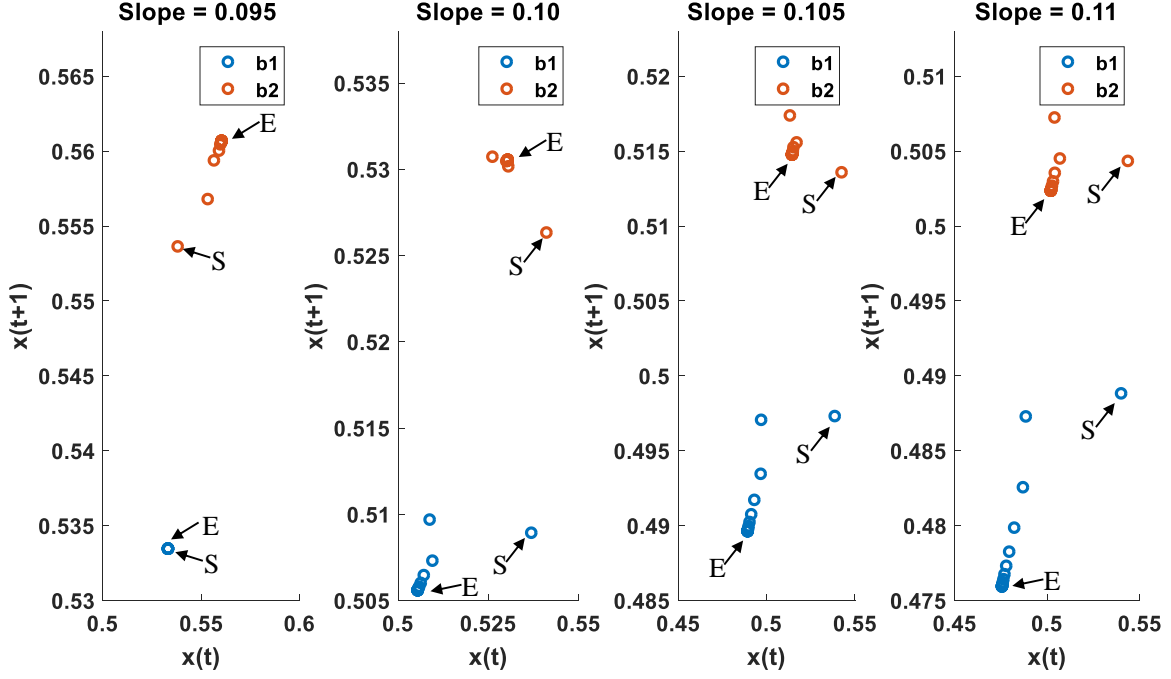
Figure 6.6: Poincare sections of step time for bipedal walking model at four different slopes (0.095 rad, 0.10 rad, 0.105 rad, and 0.11 rad) for two conditions: b1(normal biped walking) and b2(biped walking with assistance). S and E represent the start and end period of the walking.

the experimental results with the assistive device to see how closely the biped model can simulate the effect of assistance on human gait dynamics from Chaos perspective.

Biped dynamics

The dynamics of the biped were taken from [174]. There were separate models given for stance and swing legs, which were coupled through interaction forces. The coupled dynamics for the two legs were given in [174]. For simplicity, the symmetry was assumed in the full biped. The energy for the locomotive pattern was supplied to the model via a slightly sloped rigid walking surface ($\gamma < 0.12$ radians). The stance period was divided into three phases: heel contact, flat foot and toe contact for which appropriate holonomic contact constraints were defined. The biped model converges

to stable, natural looking gait using joint impedance control. The control torque of each joint was constructed using an energetically passive spring-damper coupled with phase-dependent equilibrium points. This control paradigm was adopted to generate dynamic walking gaits that preserve the ballistic swing motion and the energetic efficiency down slopes that were characteristic of human locomotion. The model parameters for the biped model consisted of the average values from adult males reported in [174]. The human torque for a single joint in υ is given by

$$\upsilon_j = -K_{pj}(\theta_j - \bar{\theta}_j) - K_{dj}\dot{\theta}_j \tag{6.9}$$

where K_{pj}, K_{dj}, and $\bar{\theta}_j$, respectively, correspond to the stiffness, damping, and equilibrium angle of the joint $j \in \{a, k, h, sk, sa\}$. Here a, k correspond to the ankle and knee joints of the stance leg, and sa, sk correspond to the ankle and knee joints of the swing leg. h represents the hip joint of the biped robot. To incorporate the knee assistance into these simulations, an additional similar impedance based control strategy was implemented given stiffness and damping parameters as 25% of the human impedance parameters. It is to be noted that assistance was provided in both stance and swing phases of the biped walking due to the limitation of the simulation framework to separate stance and swing phases separately. However, in experiments with participants, the KAD provides knee assistance only in stance phase.

Biped simulation results

The biped simulations were dependent on the initial leg conditions and slope of the rigid walking surface (γ). Here simulations were performed at four different slopes from 0.095 radians to 0.11 radians with the increment of 0.05 radians for 100 footfalls each. In simulations, two cases: biped without knee assistance (b_1) and biped with knee assistance (b_2) were analyzed. The model's walking pattern was analyzed using

maps on the step time interval for each foot step of the model.

The maps for the step interval time for the bipedal walking at four different slopes are given in Fig. 6.6. For $\gamma = 0.095$ radians, the biped model walked at same step time interval (period 1) for every step of the continuous walking pattern in $b1$ case. Whereas, in $b1$, biped increased walking pattern to period 6 chosen alternate step time intervals. For $\gamma = 0.1$ radians, the biped model in b_1 exhibited higher locomotive order with period 7. However, for the $b2$ case, the order decreased to period 4. This similar trend was observed for other two slopes $\gamma = 0.105$ radians and $\gamma = 0.110$ radians that biped model in $b2$ exhibited lower locomotive order (period 5 and period 7) than in $b1$ (period 8 and period 10). All simulations have shown that biped model started with a period on the map marked with 'S' and converges to a stable limit cycle i.e., a specific period in map marked with 'E'. The simulations results were consistent except for $\gamma = 0.095$ radians, the biped walking model with assistance exhibited lower order in comparison with the normal bipedal walking without assistance. In both cases, $b1$ and $b2$, the biped exhibited a stable walking pattern, converged to a stable limit cycle. The difference is seen in terms of the number of step time periods utilized i.e., the order of the walking pattern. It is clear from the results that the assistance makes biped walking pattern reduced to lower order but still maintain stability. The inference from the simulations is that the assistance reduces the chaotic order of the gait i.e., decreases the gait variability, but still maintains gait stability.

6.4.2   Orbital and Local Stability

Orbital stability results

Six joint segment angle time series i.e., bilateral hip, knee, and ankle joints were considered. Using GFNN, the embedded dimension for the state space reconstruction
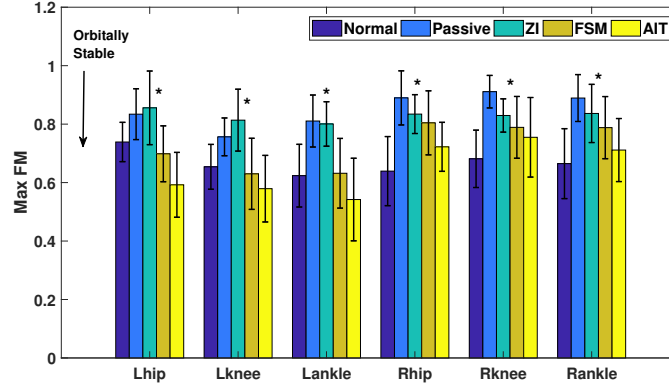
(a) Max FM for five conditions.
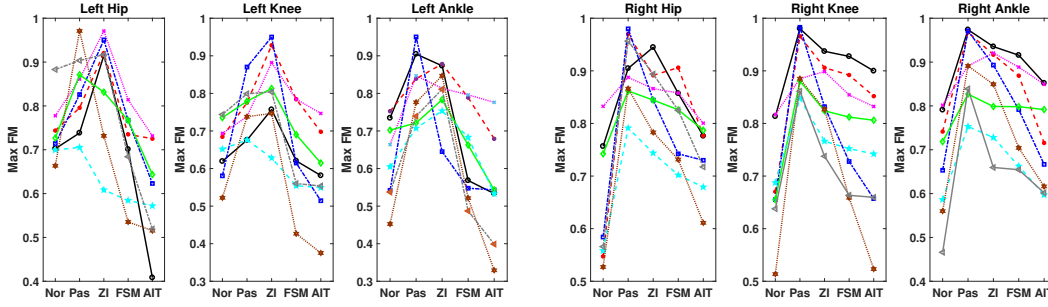
(b) Subject×condition plots (left side).

(c) Subject×Condition plots (right side).

Figure 6.7: Orbital stability results for five conditions. (a) Max FM values for all six time series measures examined. Error bars indicate between subject pooled standard deviations. Differences were statistically significant for all six time series. (b) subject × condition interaction plots for left side joint segments, (c) subject × condition interaction plots for right side joint segments, where ANOVA revealed significant differences.

was found out to be five for all the cases. The embedded state space for each time series exhibited a strong periodic structure with an expected stride to stride variability during walking. The four-dimensional maps were possible with five-dimensional data. For the computation of the FM values, 100 strides of joint segment time series were used. The strides were segmented using heel-strike events detected using force measurements from the instrumented treadmill. These 100 continuous strides were taken from the middle of the session removing start and end 30 seconds of data each.

The mean and SD of the maximum FM values (Max FMs) for eight healthy participants for six segments during five conditions is shown in Figure 6.7. Differences between the Max FMs for five conditions were analyzed using three factor (participant × condition × segment) ANOVA analysis. The p values were computed to determine the statistical significance. The statistical significance was judged based on $p \leq 0.05$. The Max FMs were statistically significant for all six joint segment time series with respect to both subjects and conditions. The statistical significance in Max FMs here refers to Max FMs that are statistically different in both subject as well as condition wise. Therefore, subject × condition interaction plots are given for all participants to visualize the variation of the MAX FMs during five conditions for each participant as shown in Figure 6.7(b) and 6.7(c). It can be seen from Figure 6.7(b) that Max FMs during assistance in AIT and FSM conditions were lower than normal walking for the left leg joint segments. Whereas, passive and ZI cases exhibited higher FM values than normal walking. This similar trend was followed on the right side joint segments (shown in Figure 6.7(c)) for passive and ZI case. However, the Max FMs for AIT and FSM were slightly higher than normal walking for the right leg joint segments. We expected that wearing KAD will increase Max FM compared to the normal walking. Our hypothesis was confirmed for the right leg. However, for the left side, the KAD active conditions (FSM and AIT) exhibited lower Max FMs than normal walking. The passive and ZI conditions exhibited higher Max FMs for both legs.

Local stability results

The algorithm to compute divergence exponents λ_s and λ_l was shown to be robust for small data sets [169]. The extracted 100 continuous strides were first divided into 33, 33, and 34 strides. Then, λ_s (0 and 1 stride) and λ_l (4 and 10 strides) were computed

for all six joint segments for these 3 stride blocks and then averaged them to obtain final λ_s and λ_l. The same (participant × condition × segment) ANOVA analysis was performed to determine statistical significance.

The local divergence exponents λ_s and λ_l exhibited positive divergence values for all the five cases which infer that the system is chaotic in nature. The higher the divergence value, the higher is the order of the chaotic system. It can be seen in the Figure 6.8(a) that the λ_s estimates were statistically significant for all the joint segments. Also, they followed the trend similar to that of the Max FMs in joint segments with respect to five conditions. Whereas, the trend of λ_l are much different from that of Max FMs and λ_s. The statistical significance for λ_l can be seen in left knee, right hip, right knee, and right ankle, respectively. All participants exhibited the Max FM values below the unit circle, which implies that they were orbitally stable. However, they exhibited positive local divergence exponents which imply that they were locally unstable. The less positive value means less locally unstable. From Figures 6.7 and 6.8, it is clear that the participants were more orbitally stable and less locally unstable in the AIT for the left leg, and normal walking for the right leg. This result is interesting as the assisted side becomes less stable and unassisted side becomes more stable in AIT compared to the normal walking. The λ_l infer that the participants were locally less unstable for all the joint segments except left hip in AIT compared to the four other cases. Whereas, the participants were more locally unstable for all the joint segments in normal walking.

6.4.3   Variability results

The stride to stride variability was evaluated for six joint segment angles for all the conditions in 8 participants. The mean and SD of the joint angle trajectories for one participant is shown in Figure 6.9. The median absolute deviation (MAD)

136
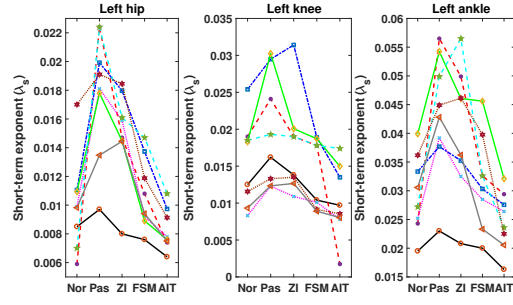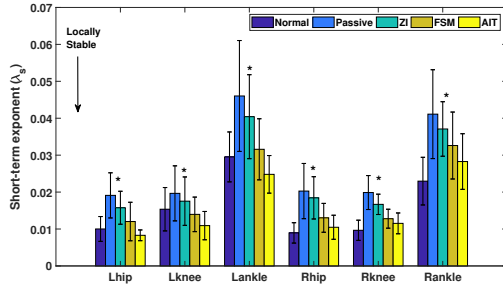
(a) Short-term exponent (λ_s) for five conditions.

(b) Subject×Condition interaction plots for left leg.
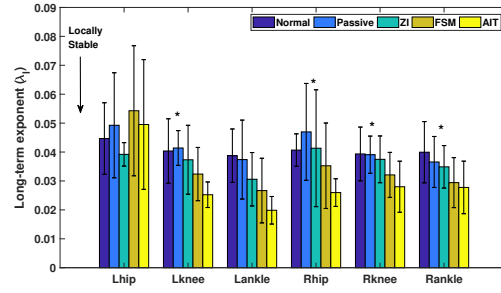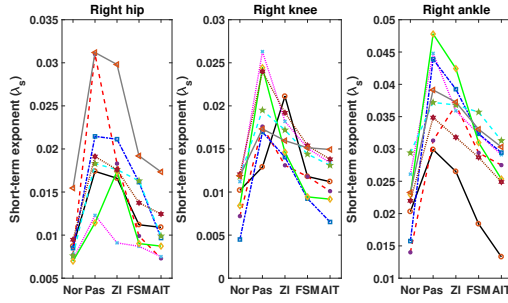
(c) Subject×Condition interaction plots for right leg.

(d) Long-term exponent (λ_l) for five conditions.
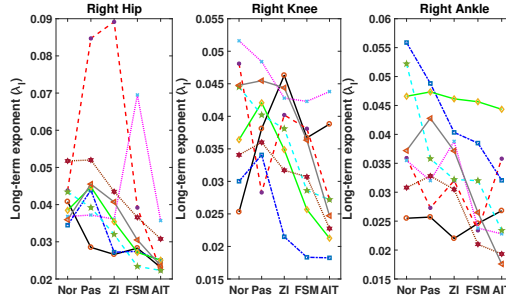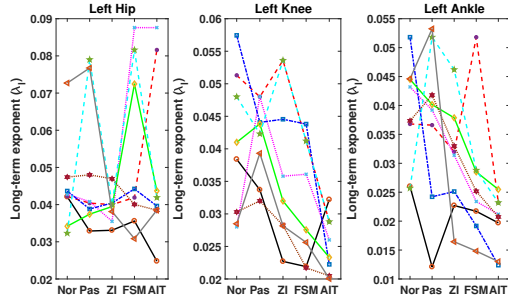
(e) Subject×Condition interaction plots for left leg.

(f) Subject×Condition interaction plots for right leg.

Figure 6.8: Local stability results for five conditions. (a) and (d): the mean and SD of λ_s and λ_l for all six time series were examined. Error bars indicate between subject pooled standard deviations. Differences were statistically significant for all six time series. (b) and (e): subject × condition interaction plots for left side joint segments, (c) and (f): subject × condition interaction plots for right side joint segments, where ANOVA revealed significant differences.

segment	Normal*	Passive*	ZI*	FSM*	AIT*
Left hip	**0.85±0.099**	0.89±0.179	1.19±0.844	0.79±0.136	**0.66±0.089**
Left knee*	**1.51±0.223**	1.41±0.375	1.69±0.789	1.26±0.359	**1.13±0.206**
Left ankle*	**0.98±0.212**	0.96±0.413	1.17±0.661	0.79±0.153	**0.69±0.109**
Right hip*	**1.30±0.380**	1.37±0.474	1.10±0.201	1.31±0.508	**0.85±0.181**
Right knee	**1.72±0.451**	2.06±0.299	2.09±0.551	2.25±0.619	**1.56±0.227**
Right ankle*	**1.61±0.439**	1.43±0.442	1.24±0.378	1.33±0.535	**0.95±0.215**

Table 6.2: The mean and SD of MAD (variability) for 8 participants (segment×condition). '*' indicates statistical significance between the subjects ($p \leq 0.05$).

measure was used as an metric to evaluate variability as it is more robust than the typical SD measure. The mean and SD of six joint angles i.e., for both left and right leg joint angles are displayed in Table 6.2. It can be seen from the Table 6.2 that AIT exhibited less MAD values for all the joints compared to four other conditions. The MAD values were higher for right knee compared to other five joints which is due to KAD. The reason is that the weight of the KAD influences the right knee joint's range of motion (ROM) and increases variability. This increased variability of knee joint ROM may cause changes to the knee joint loads applied during gait and may influence the walking pattern. Comparing MAD values for both normal walking and AIT, it is clear that the KAD reduced normal kinematic variability of the participants in AIT.

6.4.4   Extrapolated XCoM (margin of stability) results

The extrapolated (XCoM) concept was used to study the stability in both mediolateral (ML) and anteroposterior (AP) directions. In general, XCoM values were negative in AP direction stating that gait cannot be stopped within that step. The
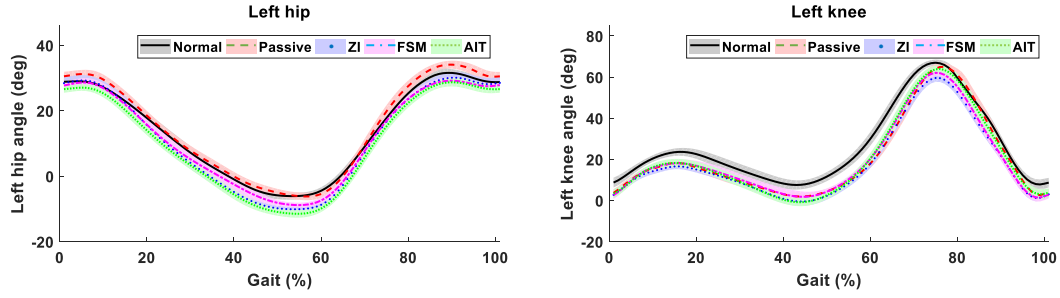
(a) Left hip angle

(b) Left knee angle
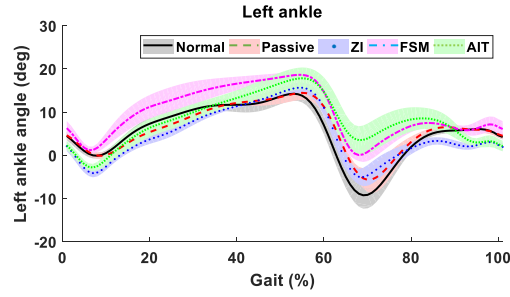
(c) Left ankle angle
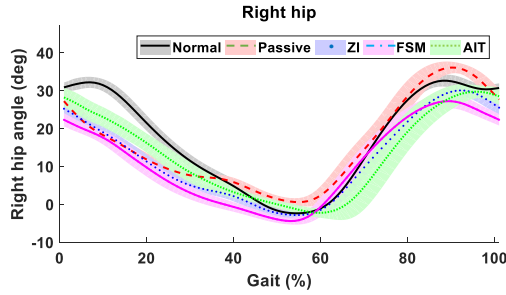
(d) Right hip angle
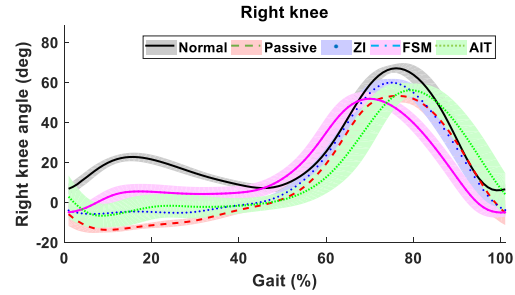
(e) Right knee angle
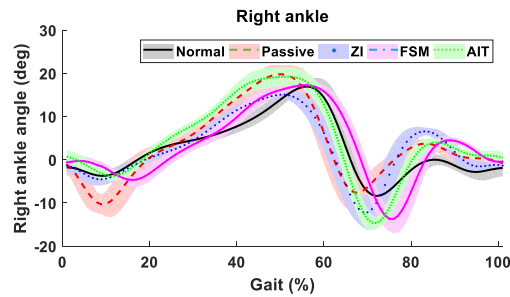
(f) Right ankle angle

Figure 6.9: The mean and SD of the left and right leg joint angles for 100 strides for one participant. The right leg joints SD is comparatively higher than left leg joints.

139
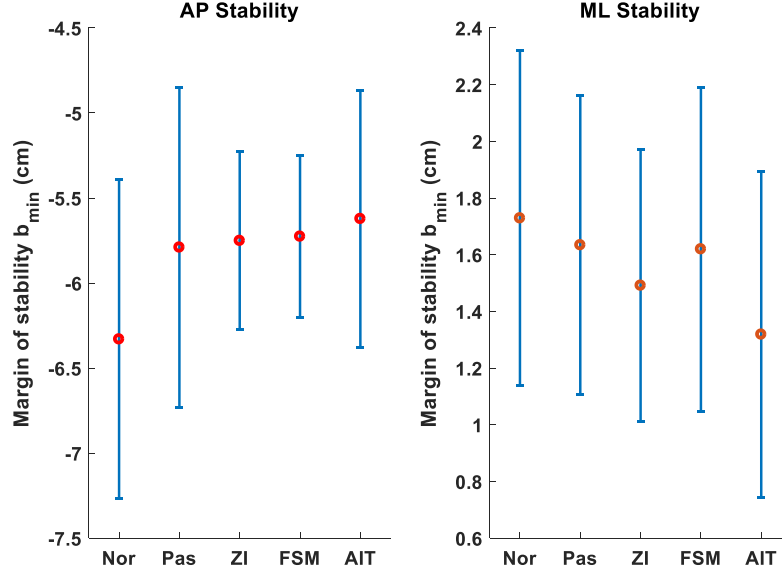
Figure 6.10: The mean and SD of margin of stability (b_{min}) values in both ML and AP directions for 8 participants for five conditions.

mean and SD of b_{min} values for all participants in both ML and AP directions are plotted in the Figure 6.10. The p values for ML and AP stability are 0.0359, 0.1537 and 0.001, 0.004 with respect to participant and condition, respectively. This means AP stability results are statistically significant ($p \leq 0.05$) with respect to both participant and condition, respectively. Whereas, the ML stability results are statistically significant ($p \leq 0.05$) with respect to the participant. It can be seen from Figure that b_{min} mean value is lower compared to other cases in AP direction which means the participants in AIT exhibits lesser instability compared to other cases. Whereas, in ML direction, the trend of mean values of b_{min} were reverse that of in AP direction which implies that participant exhibited less mediolateral stability in AIT.

6.5   Discussion

6.5.1   Assessment of Stability Metrics

It is important to evaluate if there exists any correlation between the metrics derived from dynamical system theory to have a better understanding of the stability metrics. To achieve this, correlation factor (r^2) for fitting a linear model were calculated related to both segments and conditions. For segment-based analysis, each segment is considered separately containing 40 points (subjects $\times$ condition). The statistical significance was judged based on Bonferroni correction $p < 0.05/30$ where 30 is the number segments (6) $\times$ Condition (5). This similar analysis was performed for conditions for which 48 (number of segment $\times$ condition) data points were considered. The results are shown in table 6.3. Almost no strong correlation or statistical significance were observed except for $\lambda_s \times \lambda_l$ of left knee and ankle ($\%r^2 > 29$, $p < 0.0001$). However, it was excepted that the correlation between λ_s and λ_l would be stronger since they both are the measure of local stability. It is also can be seen from the results that generally the correlation are stronger on the left side than the right side (the side with the KAD). In the condition-based analysis, it can be seen that the correlations were much weaker, which inferred that each segments stability should be analyzed separately. The other hypothesis that in FSM and AIT the correlations are higher compared to normal walking, is not strongly supported, as the r^2 values are only slightly higher for these two modes compared to normal. Since FM and λ_l both showed a similar trend of how they change condition wise for all segments and subjects (Figure 6.7 and Figure 6.2 (a) to (c)), a further analysis was done to judge the statistical significance of this hypothesis. The ANOVA analysis on (FM-$\lambda_s)\times$ Condition interaction showed that the difference of this pair of stability metrics in different conditions for each segment are statistically significant ($P < 0.005/6$),

141

meaning FM and λ_s trends over different conditions are similar.

Some clinical studies reported the correlation of Max FMs and λ_s to the actual fall incidence. For instance, the Max FMs showed expected correlation to the probability of falling in gait destabilization experiments with visual perturbations [153]. Some reported a greater λ_s in fall-prone elderly subjects than in normal elderly subjects [152]. There are no optimal values for stability metrics to maintain dynamic gait stability are not defined in the literature [150]. However, our experiment protocol was not designed to assess stability metrics for fall incidence. The focus was to assess the influence of the assistive device on the inherent dynamic gait stability of the human. Practically, the results reported in this study does not directly correlate to the probability of falling. To the best of knowledge of the authors till date, the stability assessment metrics were not defined in the literature to assess the dynamic gait stability of the human wearing LEAD. This study serves as an initial foundation to assess the dynamic gait stability of the human-LEAD system. In literature, Max FMs and λ_s when compared to λ_l and MAD correlated well with the probability of falling in various studies [150]. Therefore, Max FMs and λ_s metrics are evaluated to assess the dynamic gait stability of the human-KAD system. Whereas, λ_l and MAD are used to assess gait variability. The Max FMs and λ_s displayed statistical significant results that the unassisted side in AIT is more stable compared to other cases. The improved stability could be due to smooth transitions between the gait phases and reduced unexpected perturbations between stance and swing.

6.5.2   The Effects of Unilateral Assistance

To the best of knowledge of the authors, the overall dynamic stability analysis of human-LEAD system subjected to unilateral knee assistance was not performed in the past. We hypothesize that knee assistance provided by KAD is a type of per-

| | %r^2 | | | | | |
Segment-wise	FM×λ_s	FM×MAD	λ_s×MAD	FM×λ_l	MAD×λ_l	λ_s×λ_l
Left hip	16.3	12	2.2	1.4	0.5	0.8
Left knee	16.3	20.9	8.7	15.5	3.1	44*
Left ankle	13.5	13.9	2.9	4.6	3.7	29.4*
Right hip	19.6	5.8	3.2	7.6	7.9	9.3
Right knee	16.3	8.7	4.3	4.3	5.8	13.7
Right ankle	5.7	0.4	5.2	0.3	18.8	15.7
Condition-wise						
Normal	8.7	4.7	0.4	0.0	0.0	1.5
Passive	1.0	7.8	6.2	1.5	4.8	0
ZI	0.5	1.2	2.8	0.4	1.0	0
FSM	0.9	14.6	3.5	4.0	0.1	4.0
AIT	0.3	12.5	2.0	6.0	0.8	5.7

Table 6.3: Correlation between metrics derived from dynamical systems theory

turbation, although useful perturbation. This unilateral assistance to a specific joint will help us to understand intra and inter lower-limb joints behavior with respect to assistance. Also, this will gain insights into inter-limb coordination during such scenarios. Based on the experimental evidence from the literature, Max FM and λ_s were the most reliable measures to assess local and global stability [150]. It can be seen from Figures 6.7(a) and 6.8(a) that Max FM and λ_s for assistance conditions FSM and AIT are lower than normal walking for the left (unassisted) leg. Whereas, for the right leg, AIT and FSM exhibited slightly higher Max FM and λ_s than normal walking. Both Max FM and λ_s showed a similar trend with respect to five conditions ($P < 0.001$). This result can be analyzed from the human locomotor adaption

paradigm. In literature, there were motor adaptation studies conducted to examine bilateral responses subjected to unilateral limb perturbations [175, 176, 177]. The perturbations produced bilateral changes in kinematics. In studies [178, 179, 180], the unilateral perturbations evoked contralateral leg responses. In [178], the unilateral stiffness perturbations using variable stiffness treadmill (VST) evoked repeatable and scalable evoked muscle activity and kinematic response of the contralateral leg. Also, they provide strong evidence that supra-spinal activity can be evoked by inducing unilateral stiffness perturbations. These studies provide experimental evidence that human neuromuscular system trains to unilateral perturbations in such a way that it compensates the perturbations by responses from the unperturbed leg. In our case, it is possible that participants adopted the similar strategy to compensate the perturbations in the right (assisted) leg by responses from the left leg. From the adaptation strategy perspective, the responses from the unassisted leg would have acquired both reactive feedback mechanisms or predictive feed-forward mechanisms to counteract perturbations in the right leg. In passive and ZI cases, the KAD is just adding the extra weight of 2.3 kg to the right leg and not providing assistance, it causes discomfort to the participants. This is similar to the studies performed in the past by adding weight to a limb providing resistance while walking [181, 182, 183]. The bilateral adaptation was observed showing variability in kinematics. Therefore, Max FM and λ_s are generally higher for both legs in passive and ZI conditions.

6.5.3 Convergence of Biped Simulation Results

The biped results have shown that the order of the walking decreases with assistance compared to normal bipedal walking. The results of the biped walking simulations converge well with λ_l and MAD results. The λ_l has been used as a measure to study chaotic order and variability in the system in most of the studies [150].

144
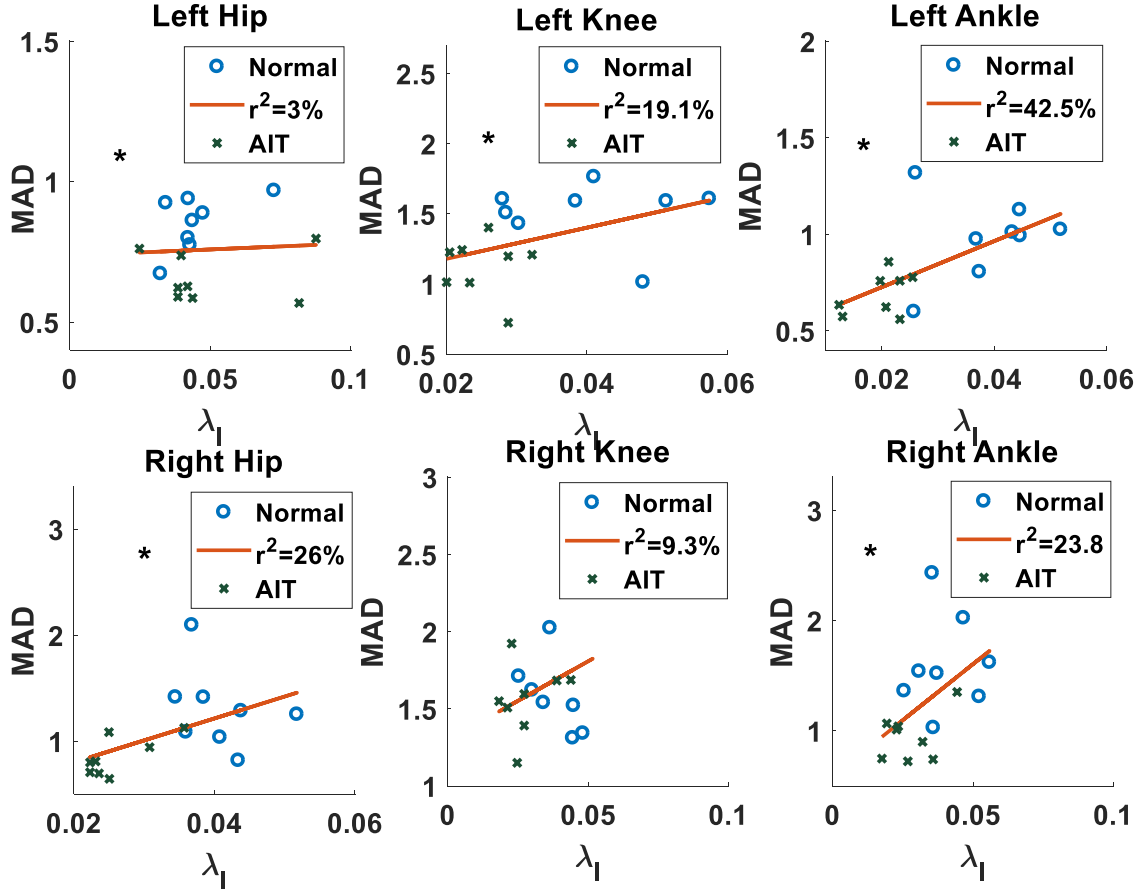
Figure 6.11: Correlations between λ_l and MAD for all six time series examined. The comparisons with these two metrics was statistically significant for all joints except right knee after Bonferroni correction ($p \leq 0.004$). For 5 statistical significant comparisons, ($3\% \leq r^2 \leq 42.5\%$). Although there is no strong linear correlation between MAD and λ_l, they follow similar trend that they are higher for normal walking condition and lower for AIT.

ANOVA statistical significance test $\lambda_l \times$ MAD $\times$ condition (normal and AIT) was conducted for five joints except right knee. The result was statistically significant for all five joints ($p \leq \frac{0.05}{12}$) showing that both λ_l and MAD decreases from normal to AIT. Although, from the r^2 values shown in the Figure 6.11, it is clear that there is no strong correlation between λ_l and MAD. The statistical significance value is based on Bonferroni correction, 12 is the number of comparisons (segment $\times$ condition). Therefore, it is possible to make inference that λ_l gives measure of chaotic order and

variability in the system. Whereas, λ_l gives the measure of the local stability. This inference agrees with the results from the studies [150].

6.5.4 Limitations of this Study

In this study, the muscle activities of lower limb muscles were not recorded. The muscular response of bilateral joints will give more insights into the relationship between dynamic gait stability and lower-limb muscular responses. Also, it will help us to understand how the participants apply the compensatory actions to perturbations with the unassisted leg from muscular level. Also, this study was conducted at the constant slope (0 degrees) and speed (0.8 m/s) of the treadmill. Multiple speeds and slope of the treadmill will provide more insights into the stability of the human-lead system with respect to various conditions. Also, overground experiments were not conducted in this study. The main reason is that participants exhibit more variability during overground walking. The outdoor experiments with different terrains will be helpful to evaluate the dynamic gait stability of the human-KAD system. As a first step to study the stability of the human-KAD system, the experiments were conducted on the treadmill with constant speed, where participants exhibit less variability.

To summarize, the overall dynamic gait stability of the human-LEAD system subjected to unilateral knee assistance was studied. The participants in AIT condition exhibited more dynamic stability on left side in terms of Max FM and λ_s compared to other four conditions. Whereas, for the right (assisted) side, higher dynamic stability is observed in normal walking. The biped walking simulation results showed that the variability decreases with joint assistance. The metrics λ_l and MAD converged to these simulation results showing that participants exhibited less kinematic variability in AIT compared to normal walking.

146

Chapter 7

HUMAN LOCOMOTION ACTIVITIES ASSISTANCE USING $A - \omega$ FEATURES BASED ADAPTIVE OSCILLATOR

In this chapter, an adaptive oscillator method known as amplitude omega adaptive oscillator ($A\omega AO$) is proposed for providing bilateral hip assistance during human locomotion activities. A real-time human locomotion recognition algorithm is integrated to $A\omega AO$ to make it robust for different locomotion activities. The human locomotion recognition algorithm comprises of both low-level (to detect activities) and high-level classifiers (to detect transitions between the activities). The support vector machine (SVM) and discrete hidden Markov model (DHMM) are used as low-level and high-level classifiers, respectively. The human locomotion recognition algorithm is trained using two-dimensional features amplitude (A) and omega (ω) obtained from thigh angle measurements using a single inertial measurement unit (IMU). $A\omega AO$ is a trajectory free method in the sense that this method provides user assistance irrespective of the human movements and require no other sensing than thigh angle measurements from IMU. In $A\omega AO$, the pool with four adaptive oscillators (AOs) is used to estimate the filtered thigh angle trajectory. This pool converges to the frequency and the phase of the signal adaptively. To account for amplitude convergence, the amplitude parameters of the oscillators need to be reinitialized based on the locomotion activity which is provided by human locomotion algorithm. In addition to the adaptive oscillators, the Gaussian kernel functions based nonlinear filter is used to predict the future estimates of the thigh angles. These predicted estimates along with the user thigh angles are used to calculate hip assistive torque in real-time which attracts user joint in the force field. To verify the efficacy of the proposed ap-

147

proach, experiments were performed using hip exoskeleton for superior augmentation (HeSA) on three healthy subjects. The human locomotion algorithm reported higher classification and prediction accuracy of 95.2% and 94.9%, respectively.

7.1 Related Work on Adaptive Oscillators

In recent years, the robotic assistive devices to aid human locomotion have gained huge popularity due to its applications in various fields. This increasing interest is primarily based on three reasons. First, aging population has become a critical concern among the developed countries. It is estimated that the people older than 60 years which are 11.5% of the global population in 2012, will be nearly doubled by 2050 according to the United Nations survey report [1]. A strong decline is locomotor skills is observed among the aged population. Also, there is a high incidence of gait disorders and lower-limb impairments which are prevalent for most of their age such as stroke is associated with hemiparesis and cardiovascular diseases lead to lower-limb amputation [184]. Therefore, there is a need for assistive devices that can provide stable, efficient, and autonomous locomotion assistance [57, 185]. Second, the people with lifelong disabilities such as spinal cord injured (SCI) patients are interested in the assistive device to enhance their locomotion skills. Third, the assistive devices are of huge interest for power augmentation purposes in industrial and military applications.

Extensive reviews of the types of wearable assistive devices and their control strategies is given in [8, 149]. These review reveal that there is still an existing need to maintain reliable human-robot interactions while evolving in complex environments with minimum effort from the user. Also, the assistive devices need to adapt to the movements of the user. Therefore, it becomes important to first identify the user's activities in real-time and then integrate it into the controller strategy of the robot to provide seamless interaction between the user and robot. The MINDWALKER

148

exoskeleton was developed to assist SCI patients with noninvasive brain control [186]. However, brain-machine interfaces (BMI) complexity limits their applications in daily-life ambulation. Some used electromyography (EMG) signals information from the user to drive the lower-limb exoskeletons [187, 188, 189]. In Hybrid Assistive Limb (HAL) unilateral knee exoskeleton, the features extracted from EMG signals are used to provide knee flexion and extension assistive torque [190]. Apart from HAL, there are only a few exoskeletons that uses EMG signals to estimate user's intentions. The reason is that the EMG signals are not reliable as they are prone to the noise in the measurement system, sensitive to the human motions, and power of the signal varies on daily basis. Also, the robustness of the EMG sensing is prone to fade in prolonged use because of the skin temperature variations, swearing, and relative movements between the skin and the electrode. Therefore, alternative approaches have recently abandoned brain and EMG sensing and preferred networks of mechanical sensors to minimize the invasiveness of the interface and increase its dependability. The commercial lower-limb orthosis is often controlled monitoring the mechanical feature of the human-exoskeleton system, such as the tilting of the trunk [79, 80]. In [81], the on-board sensors potentiometer (to measure hip joint angle) and an IMU (to detect foot contact) are used to perform human activities classification and then control the hip exoskeleton to provide assistive torque to the users during various activities.

The impedance-based controller strategy for the assistive devices has become popular due to its simplicity and intuitiveness [191]. This strategy is based on defining impedance parameters specific to gait phases or human activities such as walking and running. The finite-state machine (FSM) is the mostly used impedance based control strategy used in assistive devices. The FSM has been implemented by many different groups and with a wide variety of devices [82, 83, 46]. However, FSM exhibits sharp changes in impedance parameters when the state i.e., gait phase or the activity

changes. This may cause discomfort to the user and reduce the assistance efficiency offered by the wearable robot. This motivated researchers to develop adaptive oscillators (AOs) method to continuously synchronize with the user's movements and provide assistance adaptively. The AOs proved to learn the frequency and the phase of the periodic signals of the locomotion activities and predict the future trajectories. Seo et al. [93] used an adaptive frequency oscillator to assist the hip during gait. They use a series of adaptive frequency oscillators to estimate the state of the phase angle and then, use a multidimensional table to select what kind of torque assistance they provide given the estimated value. A. Jan Ijspeert et al. [95, 94, 96] also uses a phase based oscillator to provide assistance to periodic motions. In their case, they synchronize adaptive oscillators with the external signal and then estimate position and velocity. The aforementioned approaches, although learns the parameters of the signal, their system architecture is very complex and delays in providing controller input.

The main objective of this is to provide intuitive, robust, and adaptive control strategy for the assitive device which can decode the user's locomotion activities in real-time and can provide coherent and collaborative assistance to the user based on their activities. To identify human activities in real-time, a low level classifier (SVM) is trained on the feature vector containing A and ω. On the top of low-level classifier, a high-level classifier (DHMM) is used to detect the transitions between the activities. This human locomotion recognition algorithm is integrated to the pool of AOs to make this approach robust to any locomotion activity. Also, a Gaussian kernel based non-linear filter is used to predict the future thigh angle trajectory of the user. The contributions of this include:

1. Extending our previous work of real-time human locomotion algorithm to account for transitions between the locomotion activities using DHMM approach
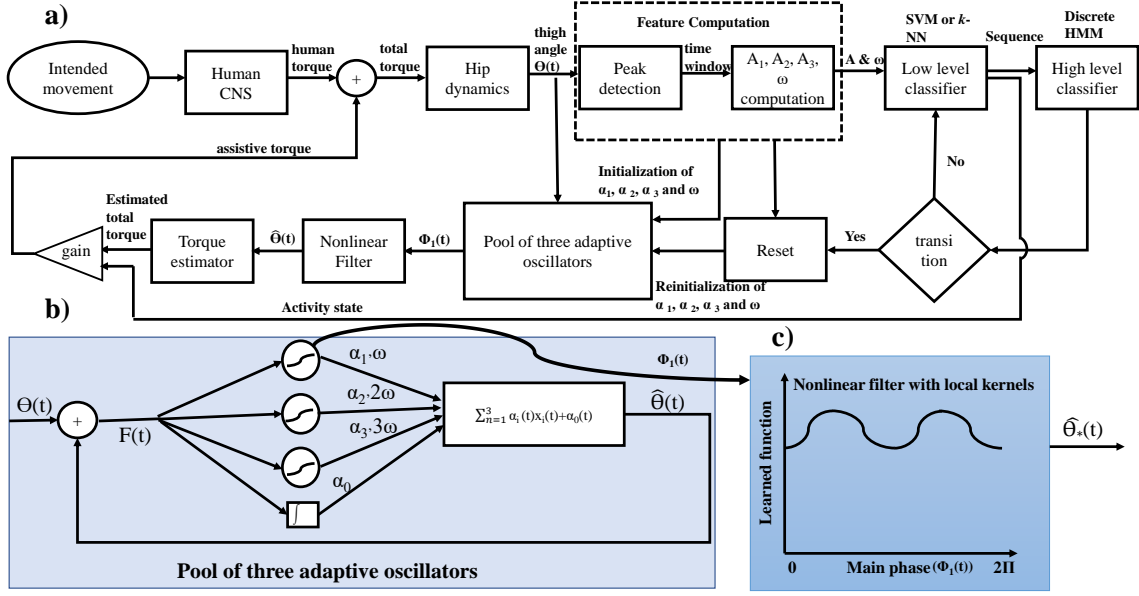
Figure 7.1: a) Block diagram of the integrated system (human + assistive device). This system mainly consists of feature computation block, human locomotion recognition algorithm (low-level classifier + high-level classifier) block and controller strategy (pool of adaptive oscillators + nonlinear filter with local kernels) for assistive device. b) Pool of adaptive oscillators learning periodic input signal $\theta(t)$. c) Kernel based nonlinear filter mapping the main phase $\phi(t)$ of the periodic signal to the input envelope.

2. Proposing re-initialization (RI) approach for the AOs to converge to the amplitude change that happens when locomotion activity changes.

3. Real-time trajectory prediction of the periodic signals related to four locomotion activities: walking, jogging, going upstairs, and going downstairs.

4. Validation of the proposed approach through experiments on three healthy exoskeleton wearing HeSA.

The rest of the chapter is structured as follows: Section 7.2 talks about the hardware used in this . Section 7.3 details the approach of human locomotion recognition algorithm (low-level and high-level classifiers). Section 7.4 discusses the framework of

Figure 7.2: The hardware overview of HeSA.

$A\omega AO$ approach. Section 7.5 gives the details of the experimental setup and discusses the results of both human locomotion algorithm and $A\omega AO$.

7.2 Hardware Setup

A bilateral hip exoskeleton HeSA (Hip exoskeleton for Superior Augmentation) is developed to provide bilateral hip assistance to the user. The design of the HeSA is displayed in the Fig. HeSA applies assistive torque at the bilateral hip using two direct-drive motors. The specifications of the direct drive motor include rated voltage, power, and torque of 24 V, 180 W, and 11.2 N·m. The Maxon controller ESCON

is used as the motor driver. The electronics are powered through a portable lipo battery.

Two inertial measurements are mounted on bilateral thighs to measure thigh angles in real-time. The placement of IMUs on the participant is shown in Fig. The combined Bosch Sensortec's BNO055 IMU and an Intel Edison processor are used for motion sensing, as shown in Fig.7.2. The sampling rate of all IMUs is set to 100 Hz. The human locomotion algorithm (SVM and DHMM) runs on the Intel Edison processor. In real-time, the processor communicates with the ESCON to generate input signals to drive the motor. Also, the wearable sensor device is connected wirelessly to a desktop to visualize the results in real-time. A TCP/IP protocol is set up between the device which transmits the data at 100HZ. The wireless network configuration finds a balance between system portability and measurement delays.

7.3 Human Locomotion Recognition Algorithm

7.3.1 Feature extraction

The algorithm is trained using a feature vector consisting of two features A and ω which are derived from the adaptive time window. An adaptive time window is built using two consecutive peaks detected using peak detection algorithm. Thus, the time window is adaptive in nature as it depends on the frequency of the thigh angle signal. Here, an assumption is made that thigh angle signal during any locomotion activity can be approximated using three harmonics. It is given in the following form:

$$g(t) = A_1 e^{j\omega t} + A_2 e^{2j\omega t} + A_3 e^{3j\omega t} \tag{7.1}$$

Where $\omega = 2\pi f$, f is the fundamental frequency of the signal and $g(t)$ is the gyro signal. The derivative and double derivative of $g(t)$ give gyro velocity and gyro

acceleration, respectively. The feature ω is found by calculating the length of the adaptive time window and amplitudes of the three harmonics A_1, A_2, and A_3 can be obtained by solving the following matrix:

$$
\begin{bmatrix} g(t) \\ \\ \frac{\dot{g}(t)}{\omega} \\ \\ \frac{\ddot{g}(t)}{\omega^2} \end{bmatrix} = \begin{bmatrix} e^{j\omega t} & e^{2j\omega t} & e^{3j\omega t} \\ \\ je^{j\omega t} & 2je^{2j\omega t} & 3je^{3j\omega t} \\ \\ -1e^{j\omega t} & -4e^{2j\omega t} & -9e^{3j\omega t} \end{bmatrix} \begin{bmatrix} A_1 \\ \\ A_2 \\ \\ A_3 \end{bmatrix} \tag{7.2}
$$

The resultant amplitude A is calculated by taking the resultant of the three mean absolute amplitude values:

$$
A = \sqrt{|A_{m1}|^2 + |A_{m2}|^2 + |A_{m3}|^2} \tag{7.3}
$$

where A_{m1}, A_{m2} and A_{m3} are the three mean absolute amplitude values for all the data samples in the time window. For every two consecutive peaks, A and ω are calculated. These features are used for training the low-level classifier.

7.3.2   Low-level classifier

The support vector machine (SVM) is used as a low-level classifier to perform locomotion activities detection. The SVM classifier is a kernel-based classifier which classifies the data into two or more classes. During the training phase, SVM builds a model, maps the decision boundary for each class and specifies the hyperplane that separates different classes. More details about SVM is given in [112]. Basically, a kernel function is the mapping procedure performed to the training dataset to improve its resemblance to a linearly separable dataset. Some of the commonly used kernel functions are linear, RBF, quadratic, polynomial and multilayer perceptron kernel. In this work, a linear kernel is used considering computation requirements

154

of the real-time classification. It is known that linear kernel performs well with the linearly separable dataset and takes less time to train the model in comparison to the other kernel methods. Therefore, it makes sense to use linear SVM as a classifier, if the features are linearly separable. The performance of the SVM classifier relies on the choice of the regularization parameter C which is known as the hyperplane parameter. The value of C was set to 1. In this work, the training labels are given to the four activities as well as the transitions between these activities.

7.3.3   High-level classifier

Discrete hidden Markov model (DHMM) [192] is used as a high-level classifier on the top of SVM. The main objective of the DHMM is to predict the next probable state (activity) using the past sequence of the activities classified by SVM. DHMM treats discrete time sequences as the output of the Markov process whose states cannot be observed directly.

A DHMM which has N states $Q = q_1, q_2, , q_N$ and M output symbols $V = v_1, v_2, ..., v_M$ is fully specified by the triplet $\lambda = A, B, \pi$. The state transition matrix A with dimension $N \times N$ is represented as

$$A = \{a_{ij}|a_{ij} = P(s_{t+1} = q_j|s_t = q_i)\}, \tag{7.4}$$

Where a_{ij} indicate the probability of transition from ith state to jth state and s_t is the state at time step t. The output probability matrix B with dimension $N \times M$ is given as

$$B = \{b_j|b_j = P(s_{t+1} = v_j|s_t = q_i)\}, \tag{7.5}$$

and the initial state distribution vector is the state at time step t. The emission probability matrix B with dimension $N \times M$ is given as

$$\pi = \{\pi_i|\pi_i = P(s_1 = q_i)\}. \tag{7.6}$$

155

Finally, the prediction problem can be formulated as the given the sequence of observations such as walking, jogging, and upstairs from the SVM classifier, what is the next probable activity? It can be obtained using the Forward-Backward algorithm given in [193]. According to it, the future hidden state (q_{t+1}) can be predicted given past observations $(v_{1:t})$ and past hidden state (q_t) by

$$P(q_{t+1}|q_t, v_{1:t}) = \sum_{x_t} P(q_{t+1}|q_t)P(q_{t+1}|v_{1:t}) \tag{7.7}$$

7.3.4   Algorithm Summary

The steps of the human locomotion algorithm training are shown in the Figure 7.3. The algorithm training and testing can be summarized into:

Training

First, the low-level classifier SVM is trained using the feature vector containing A and ω features.

- Obtain the confusion matrix from the trained SVM classifier.

- Use the obtained confusion matrix to initialize emission probability matrix (B) for the training of DHMM.

- Randomly initialize the state transition matrix (A).

- Finally, train the DHMM on the sequence of the activities classified i.e., observations through SVM using Baum Welch algorithm to obtain an optimal A and B. In our case, the length of the sequential data is chosen to two.

Testing

The testing of the SVM and HMM is performed simultaneously. The testing procedure is listed in the following steps:
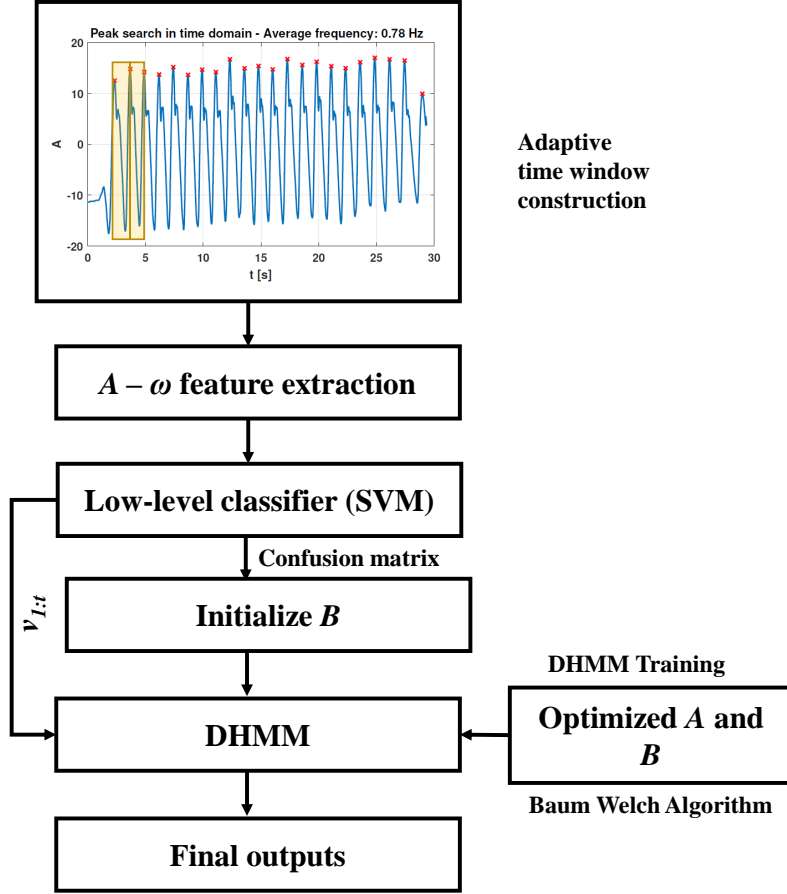
Figure 7.3: The steps of human locomotion recognition algorithm (SVM + DHMM) training. The confusion matrix from trained SVM is used to initialize the emission probability matrix B of DHMM. The optimized state transition matrix A and B are found using Baum Welch algorithm.

- SVM gives real-time activity detection results. This classification results are used as observations for DHMM model.

- Future hidden state i.e., next probable activity state is given using Forward-Backward algorithm.

The human locomotion algorithm (SVM and DHMM) is integrated to the pool of adaptive oscillators to give inference about the current activity and predict future activity state as shown in Fig. 7.1(a).

7.4   Real-time Prediction of Periodic Signals

7.4.1   Pool of AOs

The pool of AOs configuration given in [194] is applied to learn the intrinsic parameters of the periodic signal such as frequency and phase of the signal. However, the number of AOs is reduced to four by integrating real-time human locomotion algorithm which can initialize the parameters for the AOs. This makes the algorithm less computationally intensive. The pool of AOs is shown in Figure 7.1(b). The equations for the pool of AOs are :

$$\dot{\phi_i}(t) = i\omega(t) + \nu F(t)cos\phi_i(t), \tag{7.8}$$

$$\dot{\omega}(t) = \nu F(t)cos\phi_1(t), \tag{7.9}$$

$$\dot{\alpha}(t) = \eta F(t)sin\phi_i(t), \tag{7.10}$$

where, $\phi(t)$ and $\omega(t)$ are the oscillator phase and intrinsic frequency of the periodic signal. α is the amplitude of the input signal. ν is the learning parameter that determines the speed of the phase synchronization of the periodic teaching signal $F(t)$. η is the integration gain. The periodic teaching signal $F(t) = \theta(t) - \hat{\theta}(t)$, $\hat{\theta}(t) = \sum_{i=0}^{3} \alpha_i(t)sin\phi_i(t)$, and $i \in [0,3]$ are the four parallel oscillators. The 0th oscillator is just an integrator which learns the input offset. The phase of the 0th oscillator $\phi_0(t) = \phi_0(0) = \pi/2$.

This configuration of AOs is suitable for the periodic teaching signal $F(t)$ with fixed amplitude, varying frequency, and phase. However, if the amplitude of $F(t)$ changes, the learning signal takes a significant amount of time to converge to the new amplitude as the parameters of the AOs were chosen for the fixed amplitude. Therefore, it is necessary to reinitialize parameters $(\alpha_1, \alpha_2, \alpha_3)$ based on the new

amplitude. Additionally, ω is reinitialized for the new signal. Thus, re-initialization helps the pool of AOs to converge to the varying amplitude of the periodic signal as well. The decision to whether reinitialize the parameters or not is made by Human locomotion recognition algorithm as shown in Fig. 7.1(a). Therefore, this modified AOs based approach is robust to various locomotion activities.

7.4.2 Kernel-based Nonlinear Filter

To improve the quality of the signal estimate and predict the future signal trajectories, a kernel-based nonlinear filter given in [195, 196] is used. This approach is a supervised learning problem which trains between the main phase $\phi_1(t)$ and the input estimate $\hat{\theta}_*(t)$ and given by:

$$\hat{\theta}_*(t) = \frac{\sum \psi_i(\phi_1(t))w_i}{\sum \psi_i(\phi_1(t))} \tag{7.11}$$

where $\psi_i(\phi_1(t))$ is a set of Gaussian-like kernel functions. w_i are the weights of the kernel based non-linear filter. This non-linear filter constructs a series of the local mappings of the input $\hat{\theta}_*(t)$ as a function of the main phase $\phi_1(t)$. The online version is implemented using recursive least squares.

The ϕ_t in equation (7.12) is changed to $\phi_t + \Delta_\phi$ changed in order to provide the estimates of the future signal trajectory. Therefore, equation (7.12) becomes

$$\hat{\theta}_{*,\Delta}(t) = \frac{\sum \psi_{i,\Delta}(\phi_1(t))w_i}{\sum \psi_{i,\Delta}(\phi_1(t))} \tag{7.12}$$

$\hat{\theta}_{*,\Delta}(t)$ is the prediction of the future thigh angle trajectory. The estimated future position of thigh angle $\hat{\theta}_{*,\Delta}(t)$ can be used to provide assistive torque as

$$\tau_e(t) = k_f(\hat{\theta}_{*,\Delta}(t) - \theta(t)) \tag{7.13}$$

$\tau_e(t)$ and k_f are the desired assistive torque and field stiffness, respectively. For simplicity, field damping is not considered to obtain desired assistive torque. This

159

Subject Id	Age(Y)	Gender	Height (ft)	Weight (lb)
1	24	Male	5 11'	l51
2	25	Male	5 10'	143.3
3	26	Male	6	223

Table 7.1: The details of the participants who took part in the experiment. W, U, D, and J represent walking, going upstairs, going downstairs, and jogging.

assistance is intuitive in the sense as it adapts to the user's thigh motion to provide assistance based on the locomotion activity.

7.5   Results and Discussion

7.5.1   Experimental Setup

Three healthy participants took part in the experiments. The details of the participants are given in Table 7.1. The participant wearing HeSA and performing level walking and downstairs is shown in the Fig. 7.4. The Arizona State University (ASU) Institutional Review Board (IRB) reviewed and approved our study. Two experimental sessions were planned on each subject in the outdoors. The first session was conducted to train and test the human locomotion algorithm. Four activities walking, going upstairs, going downstairs, and jogging and transitions between these activities were included in the experimental trial. Each participant performed three experimental trials. Out of which, two trials of data were used to train the algorithm and remaining trial data is used to test the algorithm. In the second session, the experiments were conducted with Hesa robot. The participants wore the Hesa robot and performed all the activities continuously.

Activity	W	U	D	J	W-U	U-D	D-J	J-U	U-W	D-W	W-D	J-W	Accuracy (%)
W	269	13	18	0	0	0	0	0	0	0	0	0	89.6%
U	9	261	0	0	0	0	0	0	0	0	0	0	96.7%
D	11	0	259	0	0	0	0	0	0	0	0	0	95.9%
J	0	0	0	450	0	0	0	0	0	0	0	0	100%
W-U	0	0	0	0	30	0	0	0	0	0	0	0	100%
U-D	0	0	3	0	0	25	0	0	2	0	0	0	83.3%
D-J	0	0	0	0	0	0	30	0	0	0	0	0	100%
J-U	0	0	0	0	0	0	0	15	0	0	0	0	100%
U-W	4	0	0	0	0	2	0	0	9	0	0	0	75%
D-W	3	0	0	0	0	0	0	0	0	12	0	0	80%
W-D	0	0	4	0	0	0	0	0	0	0	11	0	73.3%
J-W	0	0	0	0	0	0	0	0	0	0	0	15	100%
													OA = 95.2%

Table 7.2: The classification result of the low-level classifier SVM for four activities and 8 transition events. W, U, D, and J represent walking, going upstairs, going downstairs and jogging activities.

Rule	Previous state	Current state	Next state
1	walk	walk	walk
2	walk	$T_{walk-up}$	up
3	$T_{walk-up}$	up	up
4	walk	up	N/A

Table 7.3: Example showing the possible prediction results corresponding to two sequential states

Figure 7.4: The participant 1 performing (a) level walking and (b)downstairs experiments.

Activity	W	U	D	J	N/A	Accuracy (%)
W	256	0	2	0	36	87%
U	0	261	0	0	9	96.6%
D	4	0	254	0	14	93.3%
J	0	0	0	450	0	100%
						OA = 94.9%

Table 7.4: The prediction results of future activities using high-level classifier DHMM
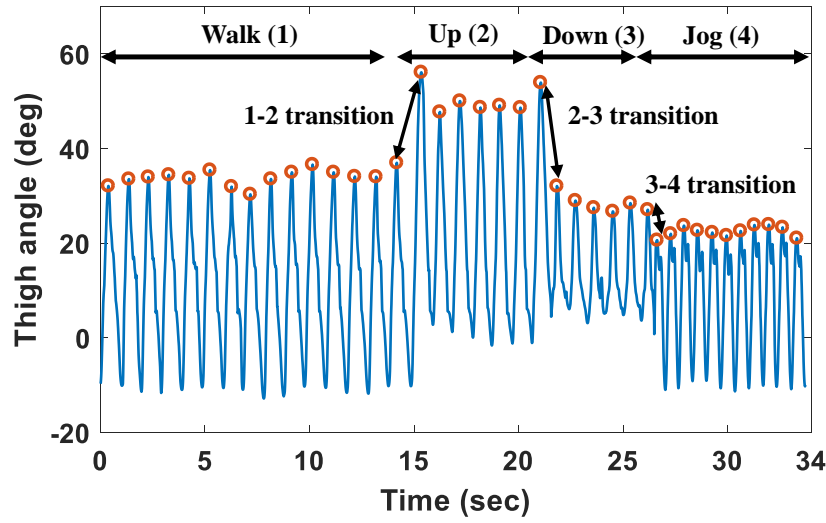
(a) The thigh angle signal for four locomotion activities.
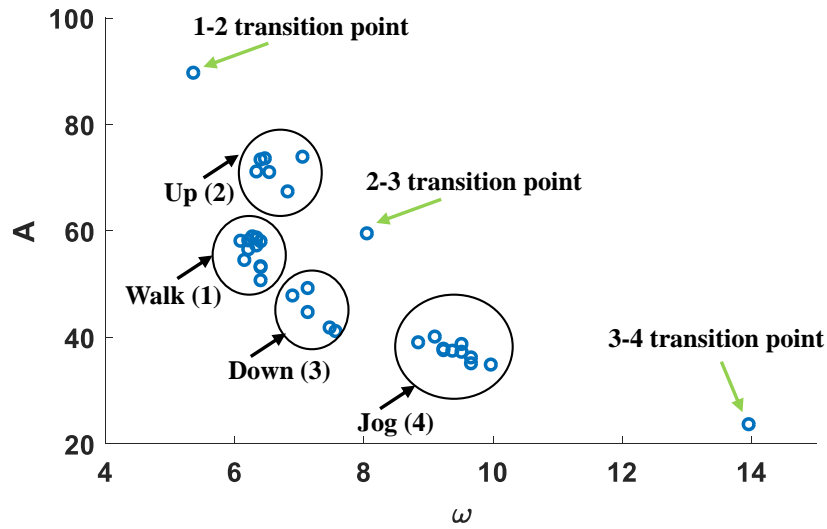
(b) A-ω feature space showing the clusters of activities and transitions.

Figure 7.5: The thigh angle recorded for participant2. a) displays the peak detection of the thigh angle recorded during four locomotion activities: walking, going upstairs, going downstairs, and jogging. b) shows the distinction between the clusters of lcomotion activities and transition points in the $A - \omega$ feature space.

7.5.2 Classification and Prediction Results

The participant's thigh data and $A - \omega$ feature space for four locomotion activities walking, going upstairs, going downstairs, and jogging is shown in the Fig. 7.5. It

can be observed from the Fig. 7.5(b) that transitions points clearly differ from the clusters of the activities. It is intuitive in the sense that when locomotion activity changes, the A and ω of the thigh signal varies and leads to a sudden change in $A - \omega$ point in the feature space. In our previous work, SVM was trained with activity labels only and transition points were not labeled. The reason was that the trained SVM ignores the transition points as outliers as there were only a few transition points. However, in this work, we labeled transitions along with the activities considering transition points will be useful in predicting the transitions. Therefore, along with the four activity labels, eight transitions labels were included in the training of the algorithm. The activities walking, jogging, going upstairs, and going downstairs were denoted as W, J, U, and D. Transitions were labeled as activity 1- activity 2. For example. the transition between W and U was labeled as W-U. The classification results of SVM for three healthy subjects are shown in Table 7.2 in terms of the confusion matrix. The overall accuracy of the detection of activities and transitions is 95.2%. The classification accuracy of the activities and transitions between the activities are 96% and 90%, respectively.

The confusion matrix of the trained SVM is used to initialize B of DHMM. The sequential input for the DHMM consists of two observations: previous and current activity which are classified using SVM. An example is shown in the Table 7.3 for the possible prediction output corresponding to two sequential inputs. The transition between the activities happens only after the transition point. For example, in the Fig 7.5, it is clear that the transition between W and U happens only if there is a transition point W-U in between W and U. Therefore, DHMM gives N/A (not available) output, if two activity inputs are in the sequence as given in Table 7.3. The prediction result using high-level classifier is shown in the Table 7.4. The prediction accuracy of DHMM is 94.9%.

7.5.3 Trajectory generation results

The difference in the filtered estimate and predicted a future estimate of the thigh trajectory provided by $A\omega AO$ alone, $A\omega AO$ and nonlinear kernel filter is shown in the Fig. 7.6. It can be seen that $\hat{\theta}_{*,\Delta}(t)$ provide a good estimate of the future thigh angle trajectory. As it can be seen in the Fig. 7.1(a), the output of DHMM decides whether to reset the amplitude parameters of AOs or not. The reinitialization procedure mainly involve three reasons. If the output of the DHMM infers transition in the state, the next state is checked whether it matches with the transition state to reinitialize the parameters. Otherwise, the transition detection is considered as the wrong result. If the output of the DHMM is N/A, it means there is no transition point in between the activities. In that case, the next two classification results were checked to confirm the transition. This procedure helps to decrease the misclassifications and increase the accuracy of the transitions. It can be seen in the Fig. 7.7 that transition happens between walking and going upstairs activity. The comparison is given with and without reinitialization. It is clear that without reinitialization, the $\hat{\theta}_{*,\Delta}(t)$ does not properly converge to the amplitude of the upstairs signal. Whereas, reinitialization helps to improve $\hat{\theta}_{*,\Delta}(t)$ estimate when the activity changes.

7.5.4 Hip assistive torque generation

The desired assistive torque for HeSA is generated based on the prediction estimate of the future thigh position given by kernel based non-linear filter. An example for the hip assistive torque generation in real-time for participant 2 while performing locomotion activities is given in Fig. 7.8. We included the zero torque condition when changing from one activity to another for two purposes: i) to identify the correct locomotion activity and ii) to learn the signal trajectory of new locomotion
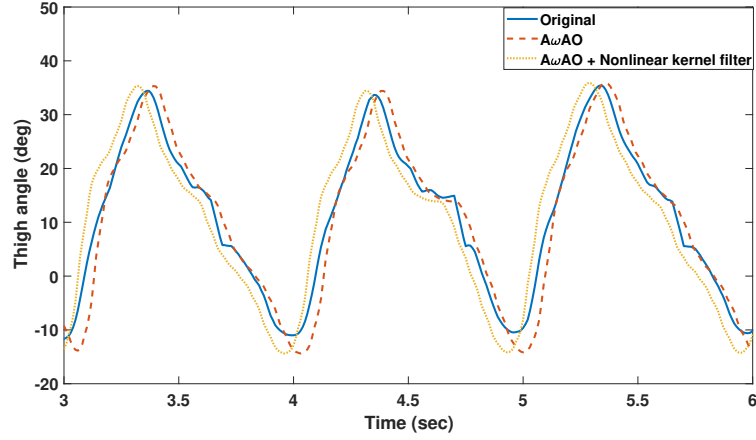
Figure 7.6: The comparison between the filtered estimate and future prediction estimate of the thigh angle trajectory during walking. The Gaussian kernel functions based non-linear filter provide a good future estimate $\hat{\theta}_{*,\Delta}(t)$ of the thigh angle trajectory.
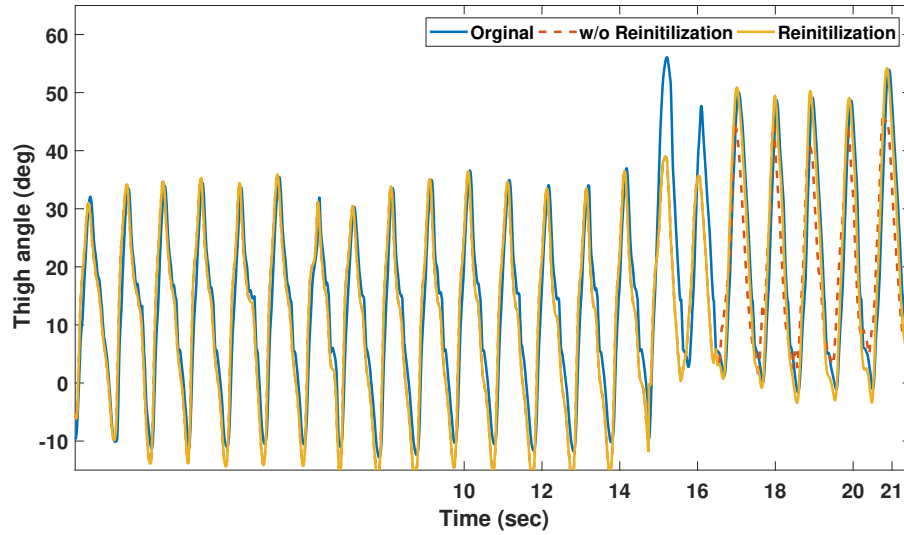
Figure 7.7: The comparison between AOs with and without reinitilization of the amplitude parameters for walking to going upstairs activity transition. The AOs with reinitilization converge faster to the amplitude of the transition activity.
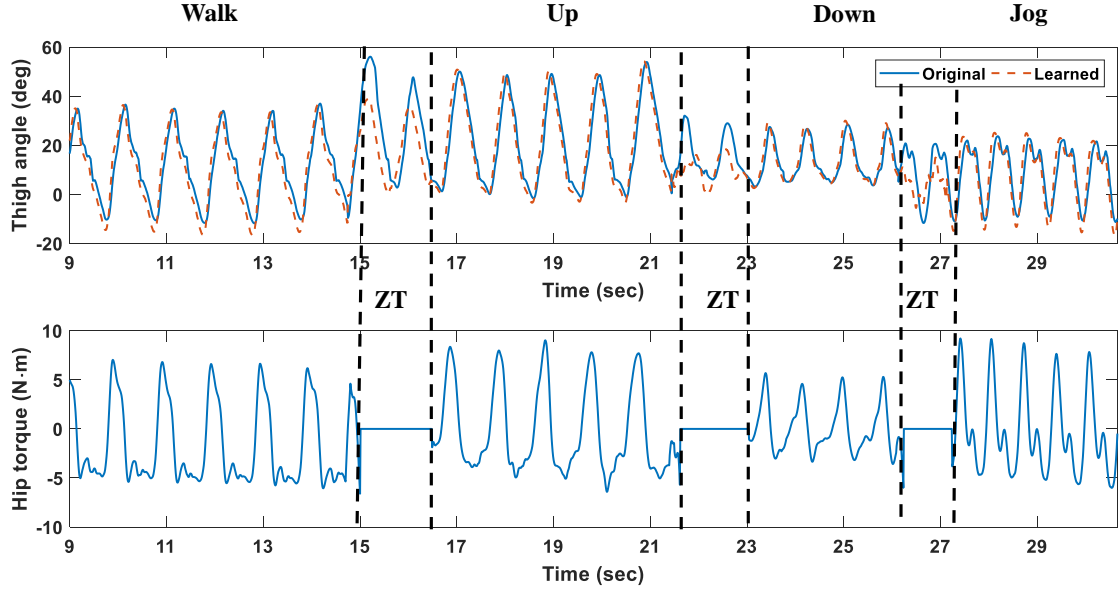
Figure 7.8: The example of assistive torque generation during four activities and transitions.

activity. The zero torque mode helps to acquire safety of the participant when activity changes. A threshold condition of 7 degree is defined for difference between predicted and original thigh trajectory to initiate zero torque condition. It can be seen from the Fig 7.8 that HeSA provides appropriate assitive torque based on the locomotion activity and zero torque when transitions happen.

Chapter 8

CONCLUSION

To summarize, an approach for the hysteresis compensator was designed as a part of this dissertation. The static and dynamic calibration tests were performed on each sensing coil to get the training data that is required to establish the model between internal pressure readings from the sensor and the GCF. An human activity recognition algorithm called as intelligent fuzzy inference (IFI) algorithm was proposed using smart shoes and IMUs. This algorithm achieved significant accuracy in both subject dependent and independent experiments. The inference can be drawn that the algorithm is more of a generalized one and does not require subject specific data to train the algorithm.

Another human activity recognition algorithm was proposed which classified periodic activities with the help of a single sensor. This system was easy to wear and eliminated the problem of mounting multiple sensors on the body for users. Although, this required subject specific data to train the algorithm, it only needed 2 to 3 minutes of data of each activity. This makes it more of a personalized system. Both indoor and outdoor experiments were performed to evaluate the efficacy of the algorithm in different conditions.

The problem of modulating the virtual impedance of the wearable robot based on activities and gait phases detection was addressed using an automatic impedance tuning (AIT) algorithm. A Gaussian mixture model (GMM) was employed to map the fuzzy likelihood of various activities and gait phases to the desired robot virtual impedance. Experiments were conducted on two participants to evaluate the benefit of the proposed algorithm by comparing muscle activities and gait metrics. The

results demonstrated that the robot assistive torque is smoother and EMG signal of Vastus Medialis is reduced, compared to constant impedance and finite state machine approaches.

To evaluate the effectiveness of both AIT and unilateral assistance on the inherent stability of the healthy subjects, the metrics were derived from dynamical systems theory to assess the overall stability of the human-LEAD system. The participants in AIT condition exhibited more dynamic stability on left side in terms of Max FM and λ_s compared to other four conditions. Whereas, for the right (assisted) side, higher dynamic stability is observed in normal walking. The biped walking simulation results showed that the variability decreases with joint assistance. The metrics λ_l and MAD converged to these simulation results showing that participants exhibited less kinematic variability in AIT compared to normal walking.

To provide bilateral assistance during locomotive activities, an adaptive oscillator based method was proposed. This adaptive oscillator was based on A and ω features. A low-level classifier SVM was trained to perform activity classifications. On the top of low-level classifier, DHHM was built to perform future activity predictions. The $A\omega AO$ along with non-linear kernel filter predicted future trajectories of thigh angle which was used to attract assistive device to the user's force field. To verify the efficacy of the proposed approach, experiments were performed using hip exoskeleton for superior augmentation (HeSA) on three healthy subjects. The human locomotion algorithm reported higher classification and prediction accuracy of 95.2% and 94.9%, respectively.

8.1 Future Work and Research Opportunities

In this dissertation work, the performance of human activity recognition algorithms was evaluated with experiments on healthy subjects. It will be helpful to

evaluate the performance of IFI and $A\omega$ methods on patients with abnormal gaits.

For AIT approach, activity transitions can be included to evaluate its performance during transitions. The AIT can be tested in outdoor environmental conditions. EMG sensors can be put on the muscles around the knee to comprehensively study the effect of the modulation of impedance parameters, and patients can be recruited to evaluate the efficacy of AIT in abnormal gaits. From a stability perspective, the future work could be studying the effect of unilateral assistance from the muscular level of lower limb joint muscles. This will help us to understand how humans adapt to assistance and modify their control strategy from muscular level. Also, optimizing the controller strategy of the knee assistive device using insights from these studies will be helpful. A similar study can be conducted on patients with abnormal gaits to study their walking pattern from the dynamical systems theory perspective. It will be interesting to see the application of these metrics to study abnormal gaits.

$A\omega AO$ can be improved to track fast transitions and generate faster future trajectory predictions. Currently, the method is based on subject-specific training. It can be improved to make the approach to be subject independent. This work can be extended by transforming the human locomotion algorithm into a semi-supervised or unsupervised approach to account for more activities and transitions.

References

[1] J. M. Ortman, V. A. Velkoff, H. Hogan, *et al.*, *An aging nation: the older population in the United States.* United States Census Bureau, Economics and Statistics Administration, US Department of Commerce, 2014.

[2] P. Lum, D. Reinkensmeyer, R. Mahoney, W. Z. Rymer, and C. Burgar, "Robotic devices for movement therapy after stroke: current status and challenges to clinical acceptance," *Topics in stroke rehabilitation*, vol. 8, no. 4, pp. 40–53, 2002.

[3] S. Patel, H. Park, P. Bonato, L. Chan, and M. Rodgers, "A review of wearable sensors and systems with application in rehabilitation," *Journal of neuroengineering and rehabilitation*, vol. 9, no. 1, p. 21, 2012.

[4] W. Meng, Q. Liu, Z. Zhou, Q. Ai, B. Sheng, and S. S. Xie, "Recent development of mechanisms and control strategies for robot-assisted lower limb rehabilitation," *Mechatronics*, vol. 31, pp. 132–145, 2015.

[5] V. S. Huang and J. W. Krakauer, "Robotic neurorehabilitation: a computational motor learning perspective," *Journal of neuroengineering and rehabilitation*, vol. 6, no. 1, p. 5, 2009.

[6] I. Díaz, J. J. Gil, and E. Sánchez, "Lower-limb robotic rehabilitation: literature review and challenges," *Journal of Robotics*, vol. 2011, 2011.

[7] J. Robertson, N. Jarrassé, and A. Roby-Brami, "Rehabilitation robots: a compliment to virtual reality," *Schedae*, vol. 1, no. 6, pp. 77–94, 2010.

[8] W. Huo, S. Mohammed, J. C. Moreno, and Y. Amirat, "Lower limb wearable robots for assistance and rehabilitation: A state of the art," *IEEE systems Journal*, vol. 10, no. 3, pp. 1068–1081, 2016.

[9] C. J. Walsh, D. Paluska, K. Pasch, W. Grand, A. Valiente, and H. Herr, "Development of a lightweight, underactuated exoskeleton for load-carrying augmentation," in *Robotics and Automation, 2006. ICRA 2006. Proceedings 2006 IEEE International Conference on.* IEEE, 2006, pp. 3485–3491.

[10] A. M. Dollar and H. Herr, "Lower extremity exoskeletons and active orthoses: challenges and state-of-the-art," *IEEE Trans. Robot.*, vol. 24, no. 1, pp. 144–158, 2008.

[11] C. V. N. Index, "Global mobile data traffic forecast update 2014–2019 white paper.(2015)," *URL: http://www. cisco. com/c/en/us/solutions/collateral/service-provider/visual-networking-index-vni/white_ paper_c11-520862. pdf.*

[12] A. Salarian *et al.*, "Quantification of tremor and bradykinesia in parkinson's disease using a novel ambulatory monitoring system," *IEEE Transactions on Biomedical Engineering*, vol. 54, no. 2, pp. 313–322, 2007.

[13] N. L. Keijsers *et al.*, "Ambulatory motor assessment in parkinson's disease," *Movement Disorders*, vol. 21, no. 1, pp. 34–44, 2006.

[14] S. H. Roy *et al.*, "Resolving signal complexities for ambulatory monitoring of motor function in parkinson's disease," in *Engineering in Medicine and Biology Society, EMBC, 2011 Annual International Conference of the IEEE*. IEEE, 2011, pp. 4836–4839.

[15] G. Uswatte *et al.*, "Validity of accelerometry for monitoring real-world arm activity in patients with subacute stroke: evidence from the extremity constraint-induced therapy evaluation trial," *Archives of physical medicine and rehabilitation*, vol. 87, no. 10, pp. 1340–1345, 2006.

[16] J. Cancela *et al.*, "Feasibility study of a wearable system based on a wireless body area network for gait assessment in parkinsons disease patients," *Sensors*, vol. 14, no. 3, pp. 4618–4633, 2014.

[17] A. Weiss *et al.*, "Can an accelerometer enhance the utility of the timed up & go test when evaluating patients with parkinson's disease?" *Medical Engineering and Physics*, vol. 32, no. 2, pp. 119–125, 2010.

[18] S. K. Prajapati *et al.*, "A novel approach to ambulatory monitoring: investigation into the quantity and control of everyday walking in patients with subacute stroke," *Neurorehabilitation and Neural Repair*, vol. 25, no. 1, pp. 6–14, 2011.

[19] S. Huang, C. Luo, S. Ye, F. Liu, B. Xie, C. Wang, L. Yang, Z. Huang, and J. Wu, "Motor impairment evaluation for upper limb in stroke patients on the basis of a microsensor," *International journal of rehabilitation research*, vol. 35, no. 2, pp. 161–169, 2012.

[20] P. T. DallAlba *et al.*, "Cervical range of motion discriminates between asymptomatic persons and those with whiplash," *Spine*, vol. 26, no. 19, pp. 2090–2094, 2001.

[21] S. J. M. Bamberg, A. Y. Benbasat, D. M. Scarborough, D. E. Krebs, and J. A. Paradiso, "Gait analysis using a shoe-integrated wireless sensor system," *IEEE transactions on information technology in biomedicine*, vol. 12, no. 4, pp. 413–423, 2008.

[22] A. M. Howell, T. Kobayashi, H. A. Hayes, K. B. Foreman, and S. J. M. Bamberg, "Kinetic gait analysis using a low-cost insole," *IEEE Transactions on Biomedical Engineering*, vol. 60, no. 12, pp. 3284–3290, 2013.

[23] C. Strohrmann, S. Patel, C. Mancinelli, L. C. Deming, J. J. Chu, R. Greenwald, G. Tröster, and P. Bonato, "Automated assessment of gait deviations in children with cerebral palsy using a sensorized shoe and active shape models," in *Body Sensor Networks (BSN), 2013 IEEE International Conference on*. IEEE, 2013, pp. 1–6.

[24] B. Lo, J. Pansiot, and G.-Z. Yang, "Bayesian analysis of sub-plantar ground reaction force with bsn," in *Wearable and Implantable Body Sensor Networks, 2009. BSN 2009. Sixth International Workshop on*. IEEE, 2009, pp. 133–137.

[25] J. M. Neugebauer, D. A. Hawkins, and L. Beckett, "Estimating youth locomotion ground reaction forces using an accelerometer-based activity monitor," *PLoS One*, vol. 7, no. 10, p. e48182, 2012.

[26] D. Staudenmann, I. Kingma, A. Daffertshofer, D. F. Stegeman, and J. H. van Dieën, "Improving emg-based muscle force estimation by using a high-density emg grid and principal component analysis," *IEEE Transactions on Biomedical Engineering*, vol. 53, no. 4, pp. 712–719, 2006.

[27] Q. Shao, D. N. Bassett, K. Manal, and T. S. Buchanan, "An emg-driven model to estimate muscle forces and joint moments in stroke patients," *Computers in biology and medicine*, vol. 39, no. 12, pp. 1083–1088, 2009.

[28] A. V. Hill, "The heat of shortening and the dynamic constants of muscle," *Proc. R. Soc. Lond. B*, vol. 126, no. 843, pp. 136–195, 1938.

[29] U. J. Naeem, C. Xiong, and A. A. Abdullah, "Emg-muscle force estimation model based on back-propagation neural network," in *Virtual Environments Human-Computer Interfaces and Measurement Systems (VECIMS), 2012 IEEE International Conference on*. IEEE, 2012, pp. 222–227.

[30] G. Colombo, M. Joerg, R. Schreier, and V. Dietz, "Treadmill training of paraplegic patients using a robotic orthosis," *Journal of rehabilitation research and development*, vol. 37, no. 6, p. 693, 2000.

[31] P. K. Artemiadis and H. I. Krebs, "On the potential field-based control of the mit-skywalker," in *Robotics and Automation (ICRA), 2011 IEEE International Conference on*. IEEE, 2011, pp. 1427–1432.

[32] S. K. Banala, S. H. Kim, S. K. Agrawal, and J. P. Scholz, "Robot assisted gait training with active leg exoskeleton (alex)," *IEEE transactions on neural systems and rehabilitation engineering*, vol. 17, no. 1, pp. 2–8, 2009.

[33] S. K. Banala, S. K. Agrawal, S. H. Kim, and J. P. Scholz, "Novel gait adaptation and neuromotor training results using an active leg exoskeleton," *IEEE/ASME Transactions on mechatronics*, vol. 15, no. 2, pp. 216–225, 2010.

[34] J. F. Veneman, R. Kruidhof, E. E. Hekman, R. Ekkelenkamp, E. H. Van Asseldonk, and H. Van Der Kooij, "Design and evaluation of the lopes exoskeleton robot for interactive gait rehabilitation," *IEEE Transactions on Neural Systems and Rehabilitation Engineering*, vol. 15, no. 3, pp. 379–386, 2007.

[35] J. Pransky, "The pransky interview: Russ angold, co-founder and president of ekso labs," *Industrial Robot: An International Journal*, vol. 41, no. 4, pp. 329–334, 2014.

[36] A. Chu, H. Kazerooni, and A. Zoss, "On the biomimetic design of the berkeley lower extremity exoskeleton (bleex)," in *Robotics and Automation, 2005. ICRA 2005. Proceedings of the 2005 IEEE International Conference on.* IEEE, 2005, pp. 4345–4352.

[37] A. B. Zoss, H. Kazerooni, and A. Chu, "Biomechanical design of the berkeley lower extremity exoskeleton (bleex)," *IEEE/ASME Transactions On Mechatronics*, vol. 11, no. 2, pp. 128–138, 2006.

[38] E. Guizzo and H. Goldstein, "The rise of the body bots [robotic exoskeletons]," *IEEE spectrum*, vol. 42, no. 10, pp. 50–56, 2005.

[39] 2017–, [Online; accessed 19-March-2018]. [Online]. Available: www.army-technology.com/projects/human-universal-load-carrier-hulc

[40] 2018–, [Online; accessed 19-March-2018]. [Online]. Available: http://bleex.me.berkeley.edu/research/exoskeleton/exoclimber/

[41] J. R. Kwapisz *et al.*, "Activity recognition using cell phone accelerometers," *ACM SigKDD Explorations Newsletter*, vol. 12, no. 2, pp. 74–82, 2011.

[42] N. A. Capela *et al.*, "Feature selection for wearable smartphone-based human activity recognition with able bodied, elderly, and stroke patients," *PloS one*, vol. 10, no. 4, p. e0124414, 2015.

[43] Z. Sheng *et al.*, "An adaptive time window method for human activity recognition," in *Electrical and Computer Engineering (CCECE), 2015 IEEE 28th Canadian Conference on.* IEEE, 2015, pp. 1188–1192.

[44] H.-Y. Lau *et al.*, "Support vector machine for classification of walking conditions using miniature kinematic sensors," *Medical & biological engineering & computing*, vol. 46, no. 6, pp. 563–573, 2008.

[45] H. Pham *et al.*, "A lle-hmm-based framework for recognizing human gait movement from emg," in *Robotics and Automation (ICRA), 2015 IEEE International Conference on.* IEEE, 2015, pp. 2997–3002.

[46] H. A. Varol *et al.*, "Multiclass real-time intent recognition of a powered lower limb prosthesis," *IEEE Transactions on Biomedical Engineering*, vol. 57, no. 3, pp. 542–551, 2010.

[47] F. J. Ordóñez and D. Roggen, "Deep convolutional and lstm recurrent neural networks for multimodal wearable activity recognition," *Sensors*, vol. 16, no. 1, p. 115, 2016.

[48] B. Chen *et al.*, "A new strategy for parameter optimization to improve phase-dependent locomotion mode recognition," *Neurocomputing*, vol. 149, pp. 585–593, 2015.

[49] H. Rezaie and M. Ghassemian, "An adaptive algorithm to improve energy efficiency in wearable activity recognition systems," *IEEE Sensors Journal*, vol. 17, no. 16, pp. 5315–5323, 2017.

[50] H. Huang *et al.*, "A strategy for identifying locomotion modes using surface electromyography," *IEEE Transactions on Biomedical Engineering*, vol. 56, no. 1, pp. 65–73, 2009.

[51] L. J. Hargrove *et al.*, "Non-weight-bearing neural control of a powered transfemoral prosthesis," *Journal of neuroengineering and rehabilitation*, vol. 10, no. 1, p. 62, 2013.

[52] K. Zhang *et al.*, "Assessment of human locomotion by using an insole measurement system and artificial neural networks," *Journal of Biomechanics*, vol. 38, no. 11, pp. 2276–2287, 2005.

[53] A. M. Khan *et al.*, "Accelerometer signal-based human activity recognition using augmented autoregressive model coefficients and artificial neural nets," in *Engineering in Medicine and Biology Society, 2008. EMBS 2008. 30th Annual International Conference of the IEEE.* IEEE, 2008, pp. 5172–5175.

[54] H. L. Bartlett and M. Goldfarb, "A phase variable approach for imu-based locomotion activity recognition," *IEEE Transactions on Biomedical Engineering*, 2017.

[55] D. Quintero *et al.*, "Real-time continuous gait phase and speed estimation from a single sensor," in *Control Technology and Applications (CCTA), 2017 IEEE Conference on.* IEEE, 2017, pp. 847–852.

[56] J. L. Pons, *Wearable robots: biomechatronic exoskeletons.* John Wiley & Sons, 2008.

[57] M. R. Tucker, J. Olivier, A. Pagel, H. Bleuler, M. Bouri, O. Lambercy, J. del R Millán, R. Riener, H. Vallery, and R. Gassert, "Control strategies for active lower extremity prosthetics and orthotics: a review," *Journal of neuroengineering and rehabilitation*, vol. 12, no. 1, p. 1, 2015.

[58] D. Novak and R. Riener, "A survey of sensor fusion methods in wearable robotics," *Robotics and Autonomous Systems*, vol. 73, pp. 155–170, 2015.

[59] L. Peeraer, B. Aeyels, and G. Van der Perre, "Development of emg-based mode and intent recognition algorithms for a computer-controlled above-knee prosthesis," *Journal of biomedical engineering*, vol. 12, no. 3, pp. 178–182, 1990.

[60] B. Chen, Q. Wang, and L. Wang, "Adaptive slope walking with a robotic transtibial prosthesis based on volitional emg control," *IEEE/ASME Transactions on mechatronics*, vol. 20, no. 5, pp. 2146–2157, 2015.

[61] D. Tkach and L. Hargrove, "Neuromechanical sensor fusion yields highest accuracies in predicting ambulation mode transitions for trans-tibial amputees," in *Engineering in medicine and biology society (EMBC), 2013 35th annual international conference of the IEEE.* IEEE, 2013, pp. 3074–3077.

[62] A. J. Young, A. Simon, and L. J. Hargrove, "An intent recognition strategy for transfemoral amputee ambulation across different locomotion modes," in *Engineering in medicine and biology society (EMBC), 2013 35th annual international conference of the IEEE.* IEEE, 2013, pp. 1587–1590.

[63] M. Goršič, R. Kamnik, L. Ambrožič, N. Vitiello, D. Lefeber, G. Pasquini, and M. Munih, "Online phase detection using wearable sensors for walking with a robotic prosthesis," *Sensors*, vol. 14, no. 2, pp. 2776–2794, 2014.

[64] L. Ambrozic, M. Gorsic, J. Geeroms, L. Flynn, R. M. Lova, R. Kamnik, M. Munih, and N. Vitiello, "Cyberlegs: A user-oriented robotic transfemoral prosthesis with whole-body awareness control," *IEEE Robotics & Automation Magazine*, vol. 21, no. 4, pp. 82–93, 2014.

[65] K. Yuan, Q. Wang, and L. Wang, "Fuzzy-logic-based terrain identification with multisensor fusion for transtibial amputees," *IEEE/ASME Transactions on Mechatronics*, vol. 20, no. 2, pp. 618–630, 2015.

[66] B. Chen, X. Wang, Y. Huang, K. Wei, and Q. Wang, "A foot-wearable interface for locomotion mode recognition based on discrete contact force distribution," *Mechatronics*, vol. 32, pp. 12–21, 2015.

[67] J. Staudenmayer, D. Pober, S. Crouter, D. Bassett, and P. Freedson, "An artificial neural network to estimate physical activity energy expenditure and identify physical activity type from an accelerometer," *Journal of Applied Physiology*, vol. 107, no. 4, pp. 1300–1307, 2009.

[68] S. E. Hussein and M. H. Granat, "Intention detection using a neuro-fuzzy emg classifier," *IEEE Engineering in Medicine and Biology Magazine*, vol. 21, no. 6, pp. 123–129, 2002.

[69] H. Huang *et al.*, "Continuous locomotion-mode identification for prosthetic legs based on neuromuscular–mechanical fusion," *IEEE Trans. Biomed. Eng.*, vol. 58, no. 10, pp. 2867–2875, 2011.

[70] E. Fullerton, B. Heller, and M. Munoz-Organero, "Recognizing human activity in free-living using multiple body-worn accelerometers," *IEEE Sensors Journal*, vol. 17, no. 16, pp. 5290–5297, 2017.

[71] G.-M. Jeong, P. H. Truong, and S.-I. Choi, "Classification of three types of walking activities regarding stairs using plantar pressure sensors," *IEEE Sensors Journal*, vol. 17, no. 9, pp. 2638–2639, 2017.

[72] T. Yan, M. Cempini, C. M. Oddo, and N. Vitiello, "Review of assistive strategies in powered lower-limb orthoses and exoskeletons," *Robotics and Autonomous Systems*, vol. 64, pp. 120–136, 2015.

[73] P. Beyl, M. Van Damme, R. Van Ham, B. Vanderborght, and D. Lefeber, "Pleated pneumatic artificial muscle-based actuator system as a torque source for compliant lower limb exoskeletons," *IEEE/ASME Transactions on Mechatronics*, vol. 19, no. 3, pp. 1046–1056, 2014.

[74] M. Cestari, D. Sanz-Merodio, J. C. Arevalo, and E. Garcia, "An adjustable compliant joint for lower-limb exoskeletons," *IEEE/ASME Transactions on Mechatronics*, vol. 20, no. 2, pp. 889–898, 2015.

[75] B. Ugurlu, C. Doppmann, M. Hamaya, P. Forni, T. Teramae, T. Noda, and J. Morimoto, "Variable ankle stiffness improves balance control: Experiments on a bipedal exoskeleton," *IEEE/ASME Transactions on mechatronics*, vol. 21, no. 1, pp. 79–87, 2016.

[76] S. Wang, L. Wang, C. Meijneke, E. Van Asseldonk, T. Hoellinger, G. Cheron, Y. Ivanenko, V. La Scaleia, F. Sylos-Labini, M. Molinari, *et al.*, "Design and control of the mindwalker exoskeleton," *IEEE transactions on neural systems and rehabilitation engineering*, vol. 23, no. 2, pp. 277–286, 2015.

[77] A. Kilicarslan, S. Prasad, R. G. Grossman, and J. L. Contreras-Vidal, "High accuracy decoding of user intentions using eeg to control a lower-body exoskeleton," in *Engineering in medicine and biology society (EMBC), 2013 35th annual international conference of the IEEE.* IEEE, 2013, pp. 5606–5609.

[78] J. C. Bradford, J. R. Lukos, and D. P. Ferris, "Electrocortical activity distinguishes between uphill and level walking in humans," *Journal of neurophysiology*, vol. 115, no. 2, pp. 958–966, 2015.

[79] 2018–, [Online; accessed 19-March-2018]. [Online]. Available: rewalk.com/rewalk-personal-3/

[80] 2018–, [Online; accessed 19-March-2018]. [Online]. Available: https://eksobionics.com/eksohealth/products/

[81] J. Jang, K. Kim, J. Lee, B. Lim, and Y. Shim, "Online gait task recognition algorithm for hip exoskeleton," in *Intelligent Robots and Systems (IROS), 2015 IEEE/RSJ International Conference on.* IEEE, 2015, pp. 5327–5332.

[82] K. Fite, J. Mitchell, F. Sup, and M. Goldfarb, "Design and control of an electrically powered knee prosthesis," in *Rehabilitation robotics, 2007. ICORR 2007. IEEE 10th international conference on.* IEEE, 2007, pp. 902–905.

[83] F. Sup, H. A. Varol, J. Mitchell, T. J. Withrow, and M. Goldfarb, "Self-contained powered knee and ankle prosthesis: Initial evaluation on a transfemoral amputee," in *Rehabilitation Robotics, 2009. ICORR 2009. IEEE International Conference on.* IEEE, 2009, pp. 638–644.

[84] C. D. Hoover, G. D. Fulk, and K. B. Fite, "Stair ascent with a powered transfemoral prosthesis under direct myoelectric control," *IEEE/ASME Transactions on Mechatronics*, vol. 18, no. 3, pp. 1191–1200, 2013.

[85] M. Liu, F. Zhang, P. Datseris, and H. H. Huang, "Improving finite state impedance control of active-transfemoral prosthesis using dempster-shafer based state transition rules," *Journal of Intelligent & Robotic Systems*, vol. 76, no. 3-4, pp. 461–474, 2014.

[86] S. M. Pfeifer, "Biomimetic stiffness for transfemoral prostheses," Ph.D. dissertation, ETH Zurich, 2014.

[87] M. A. Holgate, T. G. Sugar, and A. W. Bohler, "A novel control algorithm for wearable robotics using phase plane invariants," in *Robotics and Automation, 2009. ICRA'09. IEEE International Conference on.* IEEE, 2009, pp. 3845–3850.

[88] R. D. Gregg and J. W. Sensinger, "Towards biomimetic virtual constraint control of a powered prosthetic leg," *IEEE Transactions on Control Systems Technology*, vol. 22, no. 1, pp. 246–254, 2014.

[89] D. Y. Li, A. Becker, K. A. Shorter, T. Bretl, and E. T. Hsiao-Wecksler, "Estimating system state during human walking with a powered ankle-foot orthosis," *IEEE/ASME Transactions on Mechatronics*, vol. 16, no. 5, pp. 835–844, 2011.

[90] J. Kerestes, T. G. Sugar, T. Flaven, M. Holgate, and R. K. Ramachandran, "A method to add energy to running gait: Pogosuit," in *ASME 2014 International Design Engineering Technical Conferences and Computers and Information in Engineering Conference.* American Society of Mechanical Engineers, 2014, pp. V05AT08A005–V05AT08A005.

[91] S. Revzen and J. M. Guckenheimer, "Estimating the phase of synchronized oscillators," *Physical Review E*, vol. 78, no. 5, p. 051907, 2008.

[92] ——, "Finding the dimension of slow dynamics in a rhythmic system," *Journal of The Royal Society Interface*, vol. 9, no. 70, pp. 957–971, 2012.

[93] K. Seo, S. Hyung, B. K. Choi, Y. Lee, and Y. Shim, "A new adaptive frequency oscillator for gait assistance," in *Robotics and Automation (ICRA), 2015 IEEE International Conference on.* IEEE, 2015, pp. 5565–5571.

[94] L. Righetti, J. Buchli, and A. J. Ijspeert, "Dynamic hebbian learning in adaptive frequency oscillators," *Physica D: Nonlinear Phenomena*, vol. 216, no. 2, pp. 269–281, 2006.

[95] R. Ronsse, N. Vitiello, T. Lenzi, J. van den Kieboom, M. C. Carrozza, and A. J. Ijspeert, "Human–robot synchrony: flexible assistance using adaptive oscillators," *IEEE Transactions on Biomedical Engineering*, vol. 58, no. 4, pp. 1001–1012, 2011.

[96] R. Ronsse *et al.*, "Real-time estimate of period derivatives using adaptive oscillators: Application to impedance-based walking assistance," in *Intelligent Robots and Systems (IROS), 2012 IEEE/RSJ International Conference on.* IEEE, 2012, pp. 3362–3368.

[97] K. Kong and M. Tomizuka, "A gait monitoring system based on air pressure sensors embedded in a shoe," *IEEE/ASME Transactions on mechatronics*, vol. 14, no. 3, pp. 358–370, 2009.

[98] P. YOUNG and A. JAKEMAN, "Refined instrumental variable methods of recursive time-series analysis part iii. extensions," *International Journal of Control*, vol. 31, no. 4, pp. 741–764, 1980.

[99] ——, "Refined instrumental variable methods of recursive time-series analysis part i. single input, single output systems," *International Journal of Control*, vol. 29, no. 1, pp. 1–30, 1979.

[100] L. Ljung, "Experiments with identification of continuous time models," *IFAC Proceedings Volumes*, vol. 42, no. 10, pp. 1175–1180, 2009.

[101] H. O. Hartley, "The modified gauss-newton method for the fitting of non-linear regression functions by least squares," *Technometrics*, vol. 3, no. 2, pp. 269–280, 1961.

[102] J. J. Moré, "The levenberg-marquardt algorithm: implementation and theory," in *Numerical analysis.* Springer, 1978, pp. 105–116.

[103] D. W. Marquardt, "An algorithm for least-squares estimation of nonlinear parameters," *Journal of the society for Industrial and Applied Mathematics*, vol. 11, no. 2, pp. 431–441, 1963.

[104] T. F. Coleman and Y. Li, "An interior trust region approach for nonlinear minimization subject to bounds," *SIAM Journal on optimization*, vol. 6, no. 2, pp. 418–445, 1996.

[105] Z. Shi and X. Zhang, "From line search method to trust region method," in *International Symposium on OR and Its Applications*, vol. 213. Citeseer, 2005, pp. 156–170.

[106] J. Favre, R. Aissaoui, B. M. Jolles, J. A. de Guise, and K. Aminian, "Functional calibration procedure for 3d knee joint angle description using inertial sensors," *Journal of biomechanics*, vol. 42, no. 14, pp. 2330–2335, 2009.

[107] C. Jakob, P. Kugler, F. Hebenstreit, S. Reinfelder, U. Jensen, D. Schuldhaus, M. Lochmann, and B. M. Eskofier, "Estimation of the knee flexion-extension angle during dynamic sport motions using body-worn inertial sensors," in *Proceedings of the 8th International Conference on Body Area Networks.* ICST (Institute for Computer Sciences, Social-Informatics and Telecommunications Engineering), 2013, pp. 289–295.

[108] V. Lepetit and P. Fua, "Keypoint recognition using randomized trees," *IEEE transactions on pattern analysis and machine intelligence*, vol. 28, no. 9, pp. 1465–1479, 2006.

179

[109] G. Rogez, J. Rihan, S. Ramalingam, C. Orrite, and P. H. Torr, "Randomized trees for human pose detection," in *Computer Vision and Pattern Recognition, 2008. CVPR 2008. IEEE Conference on.* IEEE, 2008, pp. 1–8.

[110] L. Breiman, "Random forests," *Machine learning*, vol. 45, no. 1, pp. 5–32, 2001.

[111] L. H. Negri, "Peak detection utilities for 1d data," 2017–, [Online; accessed 21-December-2017]. [Online]. Available: https://pypi.python.org/pypi/PeakUtils

[112] C. Cortes and V. Vapnik, "Support-vector networks," *Machine learning*, vol. 20, no. 3, pp. 273–297, 1995.

[113] I. Hmeidi *et al.*, "Performance of knn and svm classifiers on full word arabic articles," *Advanced Engineering Informatics*, vol. 22, no. 1, pp. 106–111, 2008.

[114] F. Pan *et al.*, "Comprehensive vertical sample-based knn/lsvm classification for gene expression analysis," *Journal of Biomedical Informatics*, vol. 37, no. 4, pp. 240–248, 2004.

[115] G. Aguirre-Ollinger *et al.*, "Exoskeleton control for lower-extremity assistance based on adaptive frequency oscillators: Adaptation of muscle activation and movement frequency," *Proceedings of the Institution of Mechanical Engineers, Part H: Journal of Engineering in Medicine*, vol. 229, no. 1, pp. 52–68, 2015.

[116] T. G. Sugar *et al.*, "Limit cycles to enhance human performance based on phase oscillators," *Journal of Mechanisms and Robotics*, vol. 7, no. 1, p. 011001, 2015.

[117] T. G. Sugar, E. Fernandez, D. Kinney, K. W. Hollander, and S. Redkar, "Hesa, hip exoskeleton for superior assistance," in *Wearable Robotics: Challenges and Trends.* Springer, 2017, pp. 319–323.

[118] N. Hogan, "Impedance control: An approach to manipulation," in *American Control Conference, 1984.* IEEE, 1984, pp. 304–313.

[119] H. Kawamoto and Y. Sankai, "Power assist method based on phase sequence and muscle force condition for hal," *Advanced Robotics*, vol. 19, no. 7, pp. 717–734, 2005.

[120] G. Zeilig, H. Weingarden, M. Zwecker, I. Dudkiewicz, A. Bloch, and A. Esquenazi, "Safety and tolerance of the rewalk exoskeleton suit for ambulation by people with complete spinal cord injury: a pilot study," *The journal of spinal cord medicine*, vol. 35, no. 2, pp. 96–101, 2012.

[121] S. A. Kolakowsky-Hayner, J. Crew, S. Moran, and A. Shah, "Safety and feasibility of using the eksotm bionic exoskeleton to aid ambulation after spinal cord injury," *J Spine*, vol. 4, p. 003, 2013.

[122] T. C. Bulea, R. Kobetic, M. L. Audu, J. R. Schnellenberger, and R. J. Triolo, "Finite state control of a variable impedance hybrid neuroprosthesis for locomotion after paralysis," *IEEE Transactions on Neural Systems and Rehabilitation Engineering*, vol. 21, no. 1, pp. 141–151, 2013.

180

[123] A. J. del Ama, Á. Gil-Agudo, J. L. Pons, and J. C. Moreno, "Hybrid fes-robot cooperative control of ambulatory gait rehabilitation exoskeleton," *Journal of neuroengineering and rehabilitation*, vol. 11, no. 1, p. 27, 2014.

[124] B. E. Lawson, H. A. Varol, A. Huff, E. Erdemir, and M. Goldfarb, "Control of stair ascent and descent with a powered transfemoral prosthesis," *IEEE Transactions on Neural Systems and Rehabilitation Engineering*, vol. 21, no. 3, pp. 466–473, 2013.

[125] J. Li, B. Shen, C.-M. Chew, C. L. Teo, and A. N. Poo, "Novel functional task-based gait assistance control of lower extremity assistive device for level walking," *IEEE Transactions on Industrial Electronics*, vol. 63, no. 2, pp. 1096–1106, 2016.

[126] E. Perreault, L. Hargrove, D. Ludvig, H. Lee, and J. Sensinger, "Considering limb impedance in the design and control of prosthetic devices," in *Neuro-Robotics*. Springer, 2014, pp. 59–83.

[127] C. Tai and C. J. Robinson, "Knee elasticity influenced by joint angle and perturbation intensity," *IEEE Transactions on Rehabilitation Engineering*, vol. 7, no. 1, pp. 111–115, 1999.

[128] S. Pfeifer, M. Hardegger, H. Vallery, R. List, M. Foresti, R. Riener, and E. J. Perreault, "Model-based estimation of active knee stiffness," in *Rehabilitation Robotics (ICORR), 2011 IEEE International Conference on*. IEEE, 2011, pp. 1–6.

[129] R. Ranzani, "Adaptive human model-based control for active knee prosthetics," Ph.D. dissertation, 2014.

[130] P. T. Chinimilli *et al.*, "Hysteresis compensation for ground contact force measurement with shoe-embedded air pressure sensors," in *ASME Dyn. Sys. Control Conf.*, 2016, p. V001T09A006.

[131] K. Kong, J. Bae, and M. Tomizuka, "A compact rotary series elastic actuator for human assistive systems," *IEEE/ASME Trans. Mechatronics*, vol. 17, no. 2, pp. 288–297, 2012.

[132] D. A. Winter and D. Robertson, "Joint torque and energy patterns in normal gait," *Biological Cybernetics*, vol. 29, no. 3, pp. 137–142, 1978.

[133] G. Klir and B. Yuan, *Fuzzy sets and fuzzy logic*. Prentice hall New Jersey, 1995, vol. 4.

[134] P. T. Chinimilli, S. Redkar, and W. Zhang, "Human activity recognition using inertial measurement units and smart shoes," in *American Control Conference*, 2017, pp. 1462–1467.

[135] D. Reynolds, "Gaussian mixture models," *Encyclopedia of biometrics*, pp. 827–832, 2015.

[136] A. Burden, M. Trew, and V. Baltzopoulos, "Normalisation of gait emgs: a re-examination," *Journal of Electromyography and Kinesiology*, vol. 13, no. 6, pp. 519–532, 2003.

[137] R. Merletti and H. Hermens, "Introduction to the special issue on the seniam european concerted action," 2000.

[138] K. Knaepen *et al.*, "Human–robot interaction: Kinematics and muscle activity inside a powered compliant knee exoskeleton," *IEEE Trans. Neural Syst. Rehabil. Eng.*, vol. 22, no. 6, pp. 1128–1137, 2014.

[139] D. Aoyagi, W. E. Ichinose, S. J. Harkema, D. J. Reinkensmeyer, and J. E. Bobrow, "A robot and control algorithm that can synchronously assist in naturalistic motion during body-weight-supported gait training following neurologic injury," *IEEE Transactions on Neural Systems and Rehabilitation Engineering*, vol. 15, no. 3, pp. 387–400, 2007.

[140] E. H. Van Asseldonk, J. F. Veneman, R. Ekkelenkamp, J. H. Buurke, F. C. Van der Helm, and H. van der Kooij, "The effects on kinematics and muscle activity of walking in a robotic gait trainer during zero-force control," *IEEE transactions on neural systems and rehabilitation engineering*, vol. 16, no. 4, pp. 360–370, 2008.

[141] N. D. o. E. United Nations, New York and S. Affairs, *World population ageing, 1950-2050*. United Nations Publications, 2002.

[142] M. Tieland, I. Trouwborst, and B. C. Clark, "Skeletal muscle performance and ageing," *Journal of cachexia, sarcopenia and muscle*, vol. 9, no. 1, pp. 3–19, 2018.

[143] W. H. Organization, *Neurological disorders: public health challenges*. World Health Organization, 2006.

[144] W. Deng, I. Papavasileiou, Z. Qiao, W. Zhang, K.-Y. Lam, and H. Song, "Advances in automation technologies for lower-extremity neurorehabilitation: A review and future challenges," *IEEE Reviews in Biomedical Engineering*, 2018.

[145] Y. Sankai, "Hal: Hybrid assistive limb based on cybernics," in *Robotics research*. Springer, 2010, pp. 25–34.

[146] C. Hartigan, C. Kandilakis, S. Dalley, M. Clausen, E. Wilson, S. Morrison, S. Etheridge, and R. Farris, "Mobility outcomes following five training sessions with a powered exoskeleton," *Topics in spinal cord injury rehabilitation*, vol. 21, no. 2, pp. 93–99, 2015.

[147] G. F. Fuller, "Falls in the elderly." *American family physician*, vol. 61, no. 7, pp. 2159–68, 2000.

[148] J. K. Richardson and E. A. Hurvitz, "Peripheral neuropathy: a true risk factor for falls," *The Journals of Gerontology Series A: Biological Sciences and Medical Sciences*, vol. 50, no. 4, pp. M211–M215, 1995.

[149] A. J. Young and D. P. Ferris, "State of the art and future directions for lower limb robotic exoskeletons," *IEEE Transactions on Neural Systems and Rehabilitation Engineering*, vol. 25, no. 2, pp. 171–182, 2017.

[150] S. Bruijn, O. Meijer, P. Beek, and J. Van Dieën, "Assessing the stability of human locomotion: a review of current measures," *Journal of the Royal Society Interface*, vol. 10, no. 83, p. 20120999, 2013.

[151] J. Dingwell, J. Cusumano, D. Sternad, and P. Cavanagh, "Slower speeds in patients with diabetic neuropathy lead to improved local dynamic stability of continuous overground walking," *Journal of biomechanics*, vol. 33, no. 10, pp. 1269–1277, 2000.

[152] T. E. Lockhart and J. Liu, "Differentiating fall-prone and healthy adults using local dynamic stability," *Ergonomics*, vol. 51, no. 12, pp. 1860–1872, 2008.

[153] P. M. McAndrew, J. M. Wilken, and J. B. Dingwell, "Dynamic stability of human walking in visually and mechanically destabilizing environments," *Journal of biomechanics*, vol. 44, no. 4, pp. 644–649, 2011.

[154] L. Hak, H. Houdijk, F. Steenbrink, A. Mert, P. van der Wurff, P. J. Beek, and J. H. van Dieën, "Speeding up or slowing down?: Gait adaptations to preserve gait stability in response to balance perturbations," *Gait & posture*, vol. 36, no. 2, pp. 260–264, 2012.

[155] K. P. Granata and T. E. Lockhart, "Dynamic stability differences in fall-prone and healthy adults," *Journal of Electromyography and Kinesiology*, vol. 18, no. 2, pp. 172–178, 2008.

[156] K. S. van Schooten, L. H. Sloot, S. M. Bruijn, H. Kingma, O. G. Meijer, M. Pijnappels, and J. H. van Dieën, "Sensitivity of trunk variability and stability measures to balance impairments induced by galvanic vestibular stimulation during gait," *Gait & posture*, vol. 33, no. 4, pp. 656–660, 2011.

[157] T. M. Owings and M. D. Grabiner, "Measuring step kinematic variability on an instrumented treadmill: how many steps are enough?" *Journal of biomechanics*, vol. 36, no. 8, pp. 1215–1218, 2003.

[158] J. B. Dingwell, J. John, and J. P. Cusumano, "Do humans optimally exploit redundancy to control step variability in walking?" *PLoS computational biology*, vol. 6, no. 7, p. e1000856, 2010.

[159] T. Chau, S. Young, and S. Redekop, "Managing variability in the summary and comparison of gait data," *Journal of neuroengineering and rehabilitation*, vol. 2, no. 1, p. 22, 2005.

[160] K. Jordan, J. H. Challis, and K. M. Newell, "Speed influences on the scaling behavior of gait cycle fluctuations during treadmill running," *Human movement science*, vol. 26, no. 1, pp. 87–102, 2007.

[161] P. M. M. Young, J. M. Wilken, and J. B. Dingwell, "Dynamic margins of stability during human walking in destabilizing environments," *Journal of biomechanics*, vol. 45, no. 6, pp. 1053–1059, 2012.

[162] C. Duclos, P. Desjardins, S. Nadeau, A. Delisle, D. Gravel, B. Brouwer, and H. Corriveau, "Destabilizing and stabilizing forces to assess equilibrium during everyday activities," *Journal of biomechanics*, vol. 42, no. 3, pp. 379–382, 2009.

[163] J. M. Hausdorff, C. Peng, Z. Ladin, J. Y. Wei, and A. L. Goldberger, "Is walking a random walk? evidence for long-range correlations in stride interval of human gait," *Journal of Applied Physiology*, vol. 78, no. 1, pp. 349–358, 1995.

[164] U. H. Buzzi, N. Stergiou, M. J. Kurz, P. A. Hageman, and J. Heidel, "Nonlinear dynamics indicates aging affects variability during gait," *Clinical biomechanics*, vol. 18, no. 5, pp. 435–443, 2003.

[165] J. B. Dingwell and J. P. Cusumano, "Nonlinear time series analysis of normal and pathological human walking," *Chaos: An Interdisciplinary Journal of Nonlinear Science*, vol. 10, no. 4, pp. 848–863, 2000.

[166] R. T. Harbourne and N. Stergiou, "Movement variability and the use of nonlinear tools: principles to guide physical therapist practice," *Physical therapy*, vol. 89, no. 3, pp. 267–282, 2009.

[167] J. Dingwell, J. Cusumano, P. Cavanagh, and D. Sternad, "Local dynamic stability versus kinematic variability of continuous overground and treadmill walking," *Journal of biomechanical engineering*, vol. 123, no. 1, pp. 27–32, 2001.

[168] H. Kantz and T. Schreiber, *Nonlinear time series analysis*. Cambridge university press, 2004, vol. 7.

[169] M. T. Rosenstein, J. J. Collins, and C. J. De Luca, "A practical method for calculating largest lyapunov exponents from small data sets," *Physica D: Nonlinear Phenomena*, vol. 65, no. 1-2, pp. 117–134, 1993.

[170] Y. Hurmuzlu and C. Basdogan, "On the measurement of dynamic stability of human locomotion," *Journal of biomechanical engineering*, vol. 116, no. 1, pp. 30–36, 1994.

[171] J. B. Dingwell and H. G. Kang, "Differences between local and orbital dynamic stability during human walking," *Journal of biomechanical engineering*, vol. 129, no. 4, pp. 586–593, 2007.

[172] A. L. Hof, "The extrapolated center of mass concept suggests a simple control of balance in walking," *Human movement science*, vol. 27, no. 1, pp. 112–125, 2008.

[173] A. L. Hof, R. M. van Bockel, T. Schoppen, and K. Postema, "Control of lateral balance in walking: experimental findings in normal subjects and above-knee amputees," *Gait & posture*, vol. 25, no. 2, pp. 250–258, 2007.

[174] G. Lv and R. D. Gregg, "Underactuated potential energy shaping with contact constraints: Application to a powered knee-ankle orthosis," *IEEE Transactions on Control Systems Technology*, vol. 26, no. 1, pp. 181–193, 2018.

[175] J. T. Choi and A. J. Bastian, "Adaptation reveals independent control networks for human walking," *Nature neuroscience*, vol. 10, no. 8, p. 1055, 2007.

[176] D. S. Reisman, R. Wityk, K. Silver, and A. J. Bastian, "Locomotor adaptation on a split-belt treadmill can improve walking symmetry post-stroke," *Brain*, vol. 130, no. 7, pp. 1861–1872, 2007.

[177] M. Noel, K. Fortin, and L. J. Bouyer, "Using an electrohydraulic ankle foot orthosis to study modifications in feedforward control during locomotor adaptation to force fields applied in stance," *Journal of neuroengineering and rehabilitation*, vol. 6, no. 1, p. 16, 2009.

[178] J. Skidmore and P. Artemiadis, "Unilateral floor stiffness perturbations systematically evoke contralateral leg muscle responses: a new approach to robot-assisted gait therapy," *IEEE Transactions on Neural Systems and Rehabilitation Engineering*, vol. 24, no. 4, pp. 467–474, 2016.

[179] V. Dietz, G. Colombo, and R. Müller, "Single joint perturbation during gait: neuronal control of movement trajectory," *Experimental brain research*, vol. 158, no. 3, pp. 308–316, 2004.

[180] P. K. Artemiadis and H. I. Krebs, "Interlimb coordination evoked by unilateral mechanical perturbation during body-weight supported gait," in *Rehabilitation Robotics (ICORR), 2011 IEEE International Conference on*. IEEE, 2011, pp. 1–5.

[181] J. L. Emken, R. Benitez, A. Sideris, J. E. Bobrow, and D. J. Reinkensmeyer, "Motor adaptation as a greedy optimization of error and effort," *Journal of neurophysiology*, vol. 97, no. 6, pp. 3997–4006, 2007.

[182] K. E. Gordon and D. P. Ferris, "Learning to walk with a robotic ankle exoskeleton," *Journal of biomechanics*, vol. 40, no. 12, pp. 2636–2644, 2007.

[183] A. Blanchette and L. J. Bouyer, "Timing-specific transfer of adapted muscle activity after walking in an elastic force field," *Journal of neurophysiology*, vol. 102, no. 1, pp. 568–577, 2009.

[184] J. Verghese, A. LeValley, C. B. Hall, M. J. Katz, A. F. Ambrose, and R. B. Lipton, "Epidemiology of gait disorders in community-residing older adults," *Journal of the American Geriatrics Society*, vol. 54, no. 2, pp. 255–261, 2006.

[185] T. Lenzi, M. C. Carrozza, and S. K. Agrawal, "Powered hip exoskeletons can reduce the user's hip and ankle muscle activations during walking," *IEEE Transactions on Neural Systems and Rehabilitation Engineering*, vol. 21, no. 6, pp. 938–948, 2013.

[186] V. Rajasekaran, J. Aranda, and A. Casals, "User intention driven adaptive gait assistance using a wearable exoskeleton," in *Robot 2015: Second Iberian Robotics Conference.* Springer, 2016, pp. 289–301.

[187] K. Kiguchi and Y. Hayashi, "Emg-based control of a lower-limb power-assist robot," in *Intelligent Assistive Robots.* Springer, 2015, pp. 371–383.

[188] J. A. Spanias, E. J. Perreault, and L. J. Hargrove, "Detection of and compensation for emg disturbances for powered lower limb prosthesis control," *IEEE Transactions on Neural Systems and Rehabilitation Engineering*, vol. 24, no. 2, pp. 226–234, 2016.

[189] H. Kawamoto, S. Lee, S. Kanbe, and Y. Sankai, "Power assist method for hal-3 using emg-based feedback controller," in *Systems, Man and Cybernetics, 2003. IEEE International Conference on*, vol. 2.   IEEE, 2003, pp. 1648–1653.

[190] S. Lee and Y. Sankai, "Power assist control for walking aid with hal-3 based on emg and impedance adjustment around knee joint," in *Intelligent Robots and Systems, 2002. IEEE/RSJ International Conference on*, vol. 2.   IEEE, 2002, pp. 1499–1504.

[191] N. Hogan, "Impedance control: An approach to manipulation: Part iiimplementation," *Journal of dynamic systems, measurement, and control*, vol. 107, no. 1, pp. 8–16, 1985.

[192] I. L. MacDonald and W. Zucchini, *Hidden Markov and other models for discrete-valued time series.*   CRC Press, 1997, vol. 110.

[193] S.-Z. Yu and H. Kobayashi, "An efficient forward-backward algorithm for an explicit-duration hidden markov model," *IEEE signal processing letters*, vol. 10, no. 1, pp. 11–14, 2003.

[194] R. Ronsse, T. Lenzi, N. Vitiello, B. Koopman, E. van Asseldonk, S. M. M. De Rossi, J. van den Kieboom, H. van der Kooij, M. C. Carrozza, and A. J. Ijspeert, "Oscillator-based assistance of cyclical movements: model-based and model-free approaches," *Medical & biological engineering & computing*, vol. 49, no. 10, p. 1173, 2011.

[195] A. Gams, A. J. Ijspeert, S. Schaal, and J. Lenarčič, "On-line learning and modulation of periodic movements with nonlinear dynamical systems," *Autonomous robots*, vol. 27, no. 1, pp. 3–23, 2009.

[196] S. Schaal and C. G. Atkeson, "Constructive incremental learning from only local information," *Neural computation*, vol. 10, no. 8, pp. 2047–2084, 1998.